AARHUS
UNIVERSITET

Asteroseismology of Red Giant Stars: Time Series, Modelling and Mixed Modes

Chen Jiang

PHD DISSERTATION / November 2014

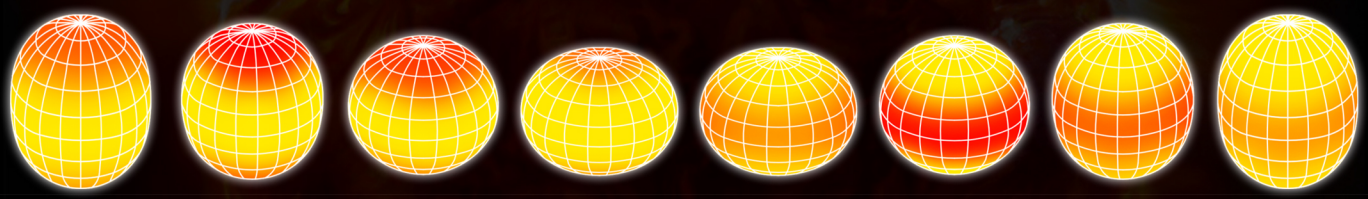

Supervisor: Jørgen Christensen-Dalsgaard
Stellar Astrophysics Centre
Faculty of Science
Department of Physics and Astronomy
Aarhus University
Denmark

Acknowledgement

Obtaining a PhD is never easy, especially having to spend such long time far away from home and family. However, during the last three years, I grew a lot and found myself on a new level of scientific research, which could not happen without the help from many people that have made my life in Aarhus much easier than I thought it would be. Let me start this thesis with some appreciations.

First, to Jørgen, the greatest man with the greatest wisdom. Thank you for giving me this fantastic opportunity to come to Aarhus and work with you and all the SACers. Thank you for your guidance, encouragement and patience for the last three years. Thank you for never forcing me, or kicking me, or screaming at me, to finish my work on time. Thank you for even when you are so busy all the time that you travel two thirds time of my PhD duration, you always reply my email immediately with the starting words of 'Many thanks'. Thank you for teaching me to recognize your handwritings with so much patience. Thank you for your endless support in every work I have done. Thank you for your guidance to prepare me for the life of an independent researcher, though I am already getting used to your comments on my work being 'not too bad'.

To Brigitte, our kindhearted and reliable secretary. Thank you for taking care of me from the first day I started my PhD in Aarhus. Thank you for your patience every time I bothering you with my financial issues and any big or small problems I encountered. Without you, my life in Denmark would be much harder.

To Prof. Jiang Biwei, for being my first mentor in Astronomy. I am grateful for being your student before I came to Denmark. Thank you for leading me the way to research and for encouraging me to continue pursuing my own way in science.

To Hans, thank you for all the answers to my questions and thank you for allowing me to travel the globe, attending conferences and workshops, meeting many interesting people.

To Frank, for years contributions to the SONG network. Your effort makes

these beautiful data of SONG become available.

To Victor for giving me advice about my PhD projects now and then.

To Rhita for reading my PhD thesis, though I sent it to you too late that you did not have time to give me much feedback.

To Vichi, for providing me the chance to administrate the software issues for the Spectroscopy Workshop in Aarhus, where I met a lot young researchers from all over the world.

To my office mates, Ditte, Vincent and Tushar for, ignoring my absence from the office in the stressful time of the last month of my PhD. Thank you for all the beers you prepared for the *Friday Bar*, which I regret not going very often.

To all the PhD class of 2011, Mia, Jens, Mikkel, for three years of friendship. All the best for your life and science in the future.

To Søren, for many inspiring discussions on my work.

To Eric, for taking care of the computing servers and providing the technical infrastructure with which we work.

To Zhuo, for being my best friend while I am alone in Denmark and for providing me shelter when I had no place to live. Wish you and Kaiyu a happy life.

To all the basketball buddies, Li Qiang, Feng Gang, Chen Yunke, Zheng Yuduo, Yu Wanwan, Gong Xianzhe, for all the happy time that we had on the basketball court, for which I could keep in good shape.

To Mario and Margarida, for offering me with an appealing job opportunity well in advance of the end of my PhD.

To my parents, Jiang Chunya and Yang Lanqiao, my sister Jiang Manling, my brother-in-law Zha Haoyu, as well as my lovely nephew Zha Ruixuan, thank you all for your love and support, without which I cannot come this far.

And finally, to the love of my life, Jing, for being present in my life. Thank you for your support during the time I am writing the thesis. I believe you will be a great architect and designer and every one knows that when he sees the beautiful cover of this thesis.

Aarhus, 30 November, 2014

Summary

As an excellent tool to study the structure of stars, asteroseismology has been developed rapidly in recent decades. By investigating stellar oscillations, it enables us to probe the interior of stars. Unlike the Sun, whose surface can be resolved by small telescopes on the Earth or even our naked eyes (using filters), other stars are observed as point sources without spatial information. However, solar-like oscillations are detected in many red giant stars that have large outer convection zones like the Sun does. Thanks to the high quality and very long term observations by NASA's space mission *Kepler*, numerous excellent data of stars in different evolutionary stages are available for the study of asteroseismology. Analyzing these data allows us to map indirectly deep inside the stars.

The high-precision observation data from photometry and spectroscopy provide various stellar parameters that can be used as constraints on stellar evolutionary codes. In return, the codes help to interpret the stars by simulating the very complicated physical processes in different parts of the stars. Making use of the pulsation codes that can compute oscillation frequencies and eigenfunctions for models generated by evolutionary codes, allows us to connect the theoretical asteroseismology with practical seismic parameters. With the help of these codes, our understanding of the inner structure and evolution of red giant stars grows as the science of asteroseismology develops. The special nature of mixed modes that have p-mode character in the outer part of stars and g-mode character in the core area, makes the investigation of stellar interior possible. The occurrence of mixed modes brings in various variations on the mode frequencies and energy inputs which are products of the stellar evolution. Mixed modes are widely detected in *Kepler* data for evolved stars and hence detailed analysis of the nature of avoided crossing and mode coupling become interesting subjects.

The work presented in this thesis focuses on data analysis, asteroseismic modelling and asymptotic analysis of mixed modes in red giant stars. It is demonstrated that the analysis of seismic data, especially the mixed modes, can open a new window on the understanding of stellar evolution and inner structure.

Danske Resumé

Inden for de seneste årtier har asteroseismologi udviklet sig hurtigt og har vist sig at være et fortrinligt redskab til at studere stjerners struktur. Ved at observere stjernernes svingninger er det muligt for os at undersøge stjernernes indre. I modsætning til Solen, hvis overflade kan studeres med mindre teleskoper på Jorden eller endda ses med det blotte øje (ved hjælp af filtre), observeres andre stjerner som punktkilder uden information om overfladestrukturer. Men man har fundet sollignende svingninger i mange røde kæmpestjerner med store ydre konvektionszoner ligesom Solens. Som et resultat af længerevarende observationer af høj kvalitet foretaget under NASAs rummission *Kepler* er talrige og fremragende data for stjerner i forskellige stadier af deres udvikling til rådighed for asteroseismologi. Ved at analysere disse data får vi mulighed for at kortlægge stjernernes dybeste indre.

De meget præcise observationsdata fra fotometri og spektroskopi bestemmer visse af stjernernes egenskaber, der kan anvendes til at efterprøve programmer til beregning af stjernernes udvikling. Disse programmer bidrager til simulering og forståelse af de meget komplicerede fysiske processer i forskellige dele af stjernerne. Ved at bruge programmer der kan beregne svingningsfrekvenser og egenfunktioner for de stjernemodeller, der produceres af stjerneudviklingsprogrammerne, får vi mulighed for at relatere den teoretiske asteroseismologi til de observerede seismiske parametre. Gennem denne analyse forbedres vores forståelse af den indre struktur og udvikling af røde kæmpestjerner gennem den videre udvikling af asteroseismologi.De særlige egenskaber ved hybride svingninger, der har akustisk karakter i den ydre del af stjernerne og tyngdebølgekarakter i det centrale område, muliggør undersøgelse af stjernernes indre. Forekomsten af hybride svingninger fører til specifikke egenskaber ved de observerede frekvenser og svingningsamplituder, som er bestemt af stjernernes udvikling. Hybride svingninger er et generelt træk i observationerne fra *Kepler* af udviklede stjerner, og det gør studiet af koblingen mellem svingninger af forskellig karakter til interessante emner for disse stjerner.

Arbejdet præsenteret i denne afhandling fokuserer på dataanalyse, asteroseismiske modellering og asymptotisk analyse af hybride svingninger i røde

kæmpestjerner. Det bliver påvist, at analysen af seismiske data, især for de hybride svingninger, åbner et nyt vindue for forståelsen af stjernernes udvikling og indre struktur.

Contents

Chapter 1

Introduction

Stars are of great importance among all the objects which modern astrophysics deals with, because they are the source of life. The effort to understand the nature of stars never stopped for thousands of years. A star undergoes a series of radical changes during its lifetime which depend on the mass of the star. The star is powered by the means of nuclear fusion for most of its life. The process fuses different chemical atoms at different evolution stage, initially starts with the fusion of hydrogen and then with heavier elements later on. Through these processes, the size as well as the structure of the star changes dramatically causing its brightness also to vary. On a much shorter timescale, some stars change their luminosity very rapidly and intrinsically, because they periodically swell and shrink, such as variable stars. Our own Sun is the most well studied variable star, based on which a science known as Helioseismology was created. Most of the observed solar oscillations have periods around 5 minutes and they are excited in the outer-layer convection zone. Studying solar-like oscillations is an expanded branch of helioseismology and an important area of asteroseismology.

The observation of solar-like stars can be performed spectroscopically and photometrically. Spectroscopy refers to the measurement of radiation intensity as a function of wavelength. It is an important tool that allows us for the derivation of the atmospheric parameters such as the surface gravity and the effective temperature, for the spectral classification and for the estimates of the chemical abundances in the stellar atmosphere. Additionally, the most valuable quantity derived from a time series of stellar spectra is the *r*adial velocity. Photometry is the technique related to the measurement of radiation intensity over large wavelength. In asteroseismology, the observed photometric time series are used to determine pulsation frequencies of stars very precisely.

In the late 19th century, the Danish astronomer Ejnar Hertzsprung noted that stars described with narrow lines tended to have smaller proper motions

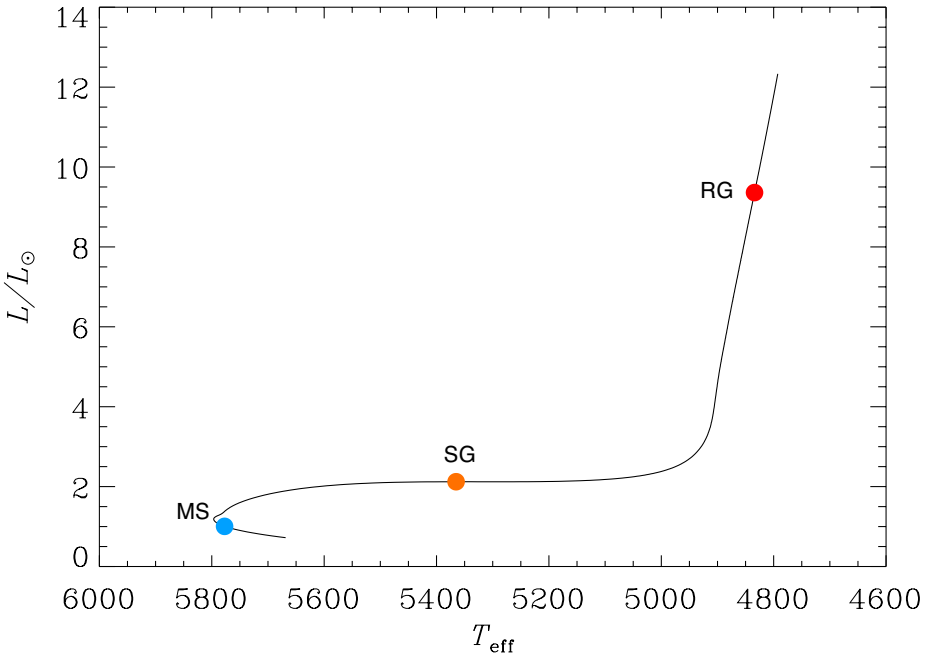

Figure 1.1: The evolutionary track of a model simulated for the Sun. The track is shown in the form of luminosity against effective temperature (a kind of H-R diagram). Three typical models at different evolution stages are coloured as blue (main sequence, MS), orange (sub-giant branch, SG) and red (ascending-branch red giant, RG). Especially the blue dot shows the location of the Sun.

than the others of the same spectral classification. He took this as an indication of greater luminosity for the narrow-line stars, and computed secular parallaxes for several groups of these, allowing him to estimate their absolute magnitude. However, the groups of stars he computed parallaxes for do not include the supergiants that are too far to obtain measure their parallaxes at that time and hence no meaningful estimate of their absolute magnitude existed prior to that work. Later in 1913, the American astronomer Henry Norris Russell's work included those supergiants and stars from the Hyades (a nearby open cluster), and several moving groups and measured their parallaxes using the method called moving cluster method to obtain absolute magnitudes for those stars. The diagram of stellar absolute magnitudes versus the spectral types represents a major step towards an understanding of stellar evolution and it is well know as *Hertzsprung-Russell diagram* (H-R diagram). There are several other forms of H-R diagram, such as ones showing the relationship between the star's luminosity and effective temperature.

1.1 Stellar Evolution

Like all the living creatures do, stars also go through the complete process of life from cradle to grave, or in astronomy it is from protostar to stellar remnants. Stellar evolution begins with the formation of the protostar, which is fulfilled by the gravitational collapse of a giant molecular cloud in the interstellar medium. The initial composition of a protostar is homogenous throughout, including about 70% of hydrogen. If the initial mass of the star is large enough, it will end up as a pre-main-sequence star, otherwise it doesn't ignite Hydrogen fusion and ends up as a brown dwarf. During the collapse, the energy of this pre-main-sequence star is generated by gravitational contraction until the core reaches the temperature required to start the core hydrogen burning and to enter the main-sequence stage. Given the fact that the evolution progress of a star depends greatly on the initial mass, it is reasonable for me to focus on stars with masses around the Solar mass as I am studying the asteroseismology of solar-like oscillations in red giant stars. Figure 1.1 shows the evolutionary track of a model simulated for the Sun, starting from the main sequence to the red giant. The track is plotted in the form of a H-R diagram, the luminosity against the effective temperature, and gives us idea of how the model evolves illustratively. Three models at different ages are picked out to represent different evolution stages, main sequence, sub-giant branch and ascending-branch red giant. The hydrogen content X of these models as well as the zero-age model are plotted in Figure 1.2, from which we can see that at the beginning of this evolution sequence, the abundance of hydrogen is uniform all through the star.

For main-sequence stars of roughly a solar mass, the central core of the star fuses hydrogen atoms into helium through proton-proton chain reactions which do not establish a steep temperature gradient in the core area. As shown by the blue dotted line in Figure 1.2, the hydrogen abundance X of the inner part of model MS increases smoothly with radius. According to the *Schwarzschild criterion*, the small temperature gradient in these low mass stars contributes to increase the convective stability and hence radiation dominates the cores. In the outer parts of these stars the gas is cool enough to be only partially ionized so that convection dominates in that region. In the sun, about 2/3 of its volume is covered by a convective envelope. Another set of fusion reaction, by which hydrogen can be also converted to helium, called *CNO cycle* (for carbon nitrogen oxygen) dominates the generation of energy in stars slightly more massive than the Sun. In the CNO cycle, the energy generation rate depends strongly on the temperature, which leads to a steep temperature gradient in the core area. Due to the strong sensitivity of temperature, convection is the dominant mode of energy transport in the core (details given in Section 1.3.4).

When these roughly one solar mass stars evolve into the post-main-sequence stage, after a short sub-giant phase. they reach the red giant branch. After the depletion of the hydrogen in the central core, the temperature in the core

is not high enough to ignite the helium fused from hydrogen during the main-sequence phase, but it is high enough to move the hydrogen burning into a shell around the core (see the orange dashed line in Figure 1.2). This causes the core to contract which increases the central temperature but the envelope starts to swell. A sub-giant star is slightly brighter than its main sequence counterpart but it cools down and changes colour rapidly as it moves to the right edge in the Hertzsprung-Russell diagrams. As the central contraction goes on, the core becomes denser and denser which generates a degenerated but not yet ignited helium core. The decreasing speed of the temperature slows down but the luminosity grows quickly, as the star ascends the red giant branch. At this time, the star is still burning hydrogen in the core shell, but the outer layer carry the energy to the surface by means of convection. This causes a uniform of X all through the convection zone leaving the bottom of the zone at the position of around 0.24 m/M (see the large gradient of X of the red line in Figure 1.2).

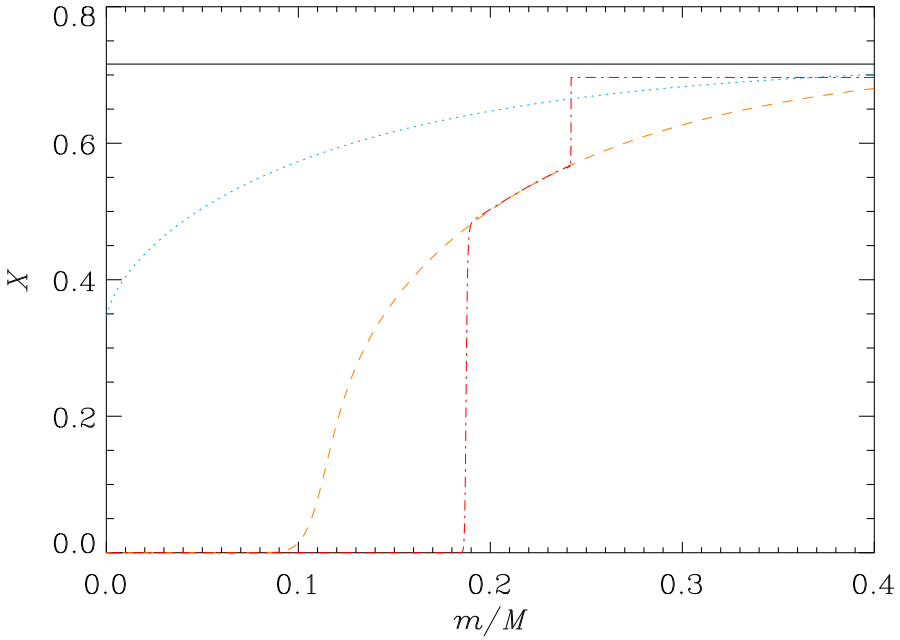

Figure 1.2: Hydrogen content X versus fractional mass m/M for four models in the solar model evolution sequence. The the blue dotted line for model MS, the orange dashed line for model SG and the red dash-dotted line for model RG in Figure 1.1, and the black solid line for the zero-age model. Only the inner 40% in mass of the models is shown.

As the hydrogen is consumed in the shell, the core absorbs the produced helium, making it even denser and contract further. Eventually this leads to the ignition of helium in the core. If the helium in the core is degenerate, the

core is supported by the electron degeneracy pressure, a thermal runaway occurs meaning that the star is undergoing a helium flash at the tip of red giant branch. The star then moves down to the horizontal branch with a helium-burning core as well as a hydrogen-burning shell. These stars are called red clump stars, hotter but less luminous than red giant stars. After the helium is exhausted in the core, the fusion is continued in a shell around the carbon-oxygen core. The star begins its life on the asymptotic giant branch, which is parallel to the red giant branch in the Hertzsprung-Russell diagram, but spends less time on this branch because of a more efficient energy generation. At this time, for a low mass star, its core may never reach temperature high enough to ignite the carbon and oxygen. The evolution of these low mass stars ends at this point and the following phases are quite complicated and controversial. Since my project is mainly focused on solar-like oscillations which can only be observed in main-sequence and red giant stars, so these late evolutionary stages are not evoked in this thesis.

1.2 Solar-like Oscillations

Solar-like oscillations are oscillations in other stars that are excited in a similar way as those in the Sun. Stars have solar-like oscillations are also called *solar-like stars*. Basically, a star is a big gaseous ball and oscillates in many different modes excited by different mechanisms. The amplitudes of the oscillations depend on the excitation and damping processes, while the frequencies are determined by some properties of the star interior, such as temperature and density. Measuring the amplitudes and frequencies of these oscillations provides us opportunities to understand the stellar inner structure and evolution that no any other way can do. The best-studied object of oscillating stars is our Sun, which oscillates in thousands of different modes simultaneously. These modes can be essentially divided into two categories by their restoring forces: gravity and acoustic modes.

For the gravity modes, or g modes, buoyancy is the restoring force and the gas motions are primarily horizontal. The gravity modes are usually low frequency modes and travel in the inner part of the star. Usually they are confined in the stellar interior below the convection zone, which makes them impossible to be observed at the surface. For the pressure modes, or p modes, pressure is their restoring force and they have gas motions that are vertical. Their dynamics depend on the variation of the sound speed in the star. The p modes normally have higher frequencies than g modes, and have very large amplitudes on the surface, so they are observable. In the Sun, the p modes have frequencies larger than 1 mHz and have the strongest signals around 3 mHz, for which they are called *5 minutes oscillations*. Thousands of p modes have been detected. In the outer layer of the Sun, the convective envelope covers 70% of its volume. The g modes are trapped only in the core area and have frequencies

less than 0.4 mHz. The gravity waves carry important information of the stellar interior, though they are very hard to be detected. The Sun has been closely observed for decades. Observations of other solar-like stars requires very high precision instruments and very long term observing time.

Solar-like oscillations are expected to be excited in all stars with outer convection envelopes. Stars having large outer convection zones are indeed the lowest mass main sequence stars up to objects near the cool edge of the classical instability strip with mass around 1.6 $M_\odot$ (Christensen-Dalsgaard, 1982; Christensen-Dalsgaard & Frandsen, 1983; Houdek et al., 1999). The driving mechanism that operates in the Sun and other solar-like stars , including some low mass cool red giant stars, is the *stochastic* driving mechanism. Stochastic excitation of oscillations in the solar atmosphere was first studied by Stein (1968), followed by Goldreich & Keeley (1977) who considered the application to the excitation of normal modes. Batchelor (1956) introduced the basics properties of damped oscillations excited by homogeneous turbulence. The power spectrum of a single mode of frequency ω_0 and damping rate η, is approximately

$$P(\omega) \simeq \frac{1}{4\omega_0^2} \frac{P_f(\omega)}{(\omega - \omega_0)^2 + \eta^2} \,, \tag{1.1}$$

where $P_f(\omega)$ is the power spectrum of the turbulent forcing. If the forcing spectrum varies slowly with frequency the result is a stochastic function modulated by a Lorentzian envelope, with a full width at half at maximum of 2η. It is obviously possible to determine the damping rate η from the fitted Lorentzian spectrum. Due to the stochastic nature of the excitation, the amplitude of a mode changes with time. However, the excitation of a certain mode is determined by the very property of the mode, and the amplitude depends on the stochastic energy input from convection and damping in the near-surface where convection is most vigorous. The mean square amplitude is approximated by (Chaplin et al., 2005)

$$\left\langle A^2 \right\rangle \simeq \frac{1}{E|\eta|} \frac{\mathcal{P}_f(\omega)}{E} \,, \tag{1.2}$$

where A can be the outcome from observation, such as the surface velocity from spectroscopy and the relative intensity variation, $\mathcal{P}_f(\omega)$ describes the energy input from convection (Christensen-Dalsgaard, 2012) and depends on the frequency but little on mode degree (Houdek, 2010). The normalized mode E inertia (Dziembowski et al., 2001) is given by

$$E = \frac{\int_0^R \left(\xi_\mathrm{r}^2 + L^2 \xi_\mathrm{h}^2\right) \rho r^2 \mathrm{d}r}{M \xi_\mathrm{r}(R)^2}, \tag{1.3}$$

where ρ is the density; r is the distance to the centre; M is the stellar mass; L is a degree related coefficient which will be given later; ξ_r and ξ_h are the radial and horizontal components of oscillation displacement. Normally where the damping rate is dominated by the near-surface layers it follows that $|\eta|E$ is

independent of E at constant frequency. Therefore, the mean square amplitude is proportional to E^{-1} at constant frequency. In the case of red giant stars, large variations in E is usually seen over a narrow frequency range, for the mixed modes which will be introduced in Section 4.1. The inertia of g modes are expected to be larger than that of p modes, because they normally travel in denser layers of the star. Basically, higher amplitudes lead to higher visibilities of the modes and hence the likelihood to detect them.

Instead of using the amplitude, Chaplin et al. (2005) noted that the ability to extract a oscillatory mode from the power spectrum depends on the *peak height* H, which is related to the mean square amplitude of the mode by

$$\left\langle A^2 \right\rangle = |\eta| H \ , \tag{1.4}$$

because the damping rate determines the peak width. Since $\left\langle A^2 \right\rangle$ and $|\eta|$ both are proportional to E^{-1} if the damping is mainly dominated by the near-surface layers, from Eq. (1.4) the peak hight H is independent of E, which means that all modes in a given frequency interval are excited to almost the same height. However, in reality, the observations are only for a finite time $\mathcal{T}$ which is typically shorter than the lifetime τ of the g-dominated modes in a red giant star. In the case of $\mathcal{T} \ll \tau$, the resulting peaks in the power density spectrum has a width proportional to $\mathcal{T}^{-1}$, i.e., that they are detected with a correspondingly smaller peak hight, which is very likely decrease the mode visibility. Fletcher et al. (2006) proposed the relation between H and $\mathcal{T}$ as

$$H \propto \frac{\left\langle A^2 \right\rangle}{|\eta| + 2/\mathcal{T}} \ , \tag{1.5}$$

which indicates that longer observation time can help discover more oscillation modes. Thanks to the long-term and high quality of the photometry data from *Kepler* and *CoRoT*, solar-like oscillations have been detected and analysed in many stars (e.g. Hekker et al., 2009; Bedding et al., 2010; Huber et al., 2010; Jiang et al., 2011; Mathur et al., 2011; Mosser et al., 2011; Baudin et al., 2012; Kallinger et al., 2012). The detail properties of observed solar-like oscillations will be introduced in the following sections.

1.3 Asymptotic Theory of Stellar Oscillations

We know there are thousands of oscillation modes existing in the Sun. They oscillate with different frequencies and having different behaviour in different regions. So how do we specify the modes?

1.3.1 Oscillations in three-dimension

Three quantum numbers are used to specify the oscillation modes: n, called the *radial order*, is related the number of radial nodes; l specifies the number of surface nodes and is called the *degree* of the mode; m is the *azimuthal order* of the mode, where $|m|$ specifies the number of longitudinal lines among the surface nodes. It is obvious that the values of m range from $-l$ to $+l$, and therefore there are $2l + 1$ modes for each degree l. Figure 1.3 presents a set of modes with different quantum numbers.

The simplest modes are the modes with $l = 0$, meaning there is no surface node, and are called *radial* modes. The radial modes make the star swell and shrink, heat and cool, as a whole ball spherically and symmetrically. In these modes the star has the core as a node and the surface as a displacement antinode. The nth overtone radial mode has n radial nodes which are concentric shells within the star (see the radial mode case in Figure 1.3).

Modes that have $l > 0$ are nonradial modes. Oscillation waves of high-degree nonradial modes can be very complicated and the simplest nonradial mode is the axisymmetric *dipole* modes, i.e., the mode with $l = 1, m = 0$. In this mode the star has its equator as a node, which makes one hemisphere swells up while the other hemisphere shrinks and vice versa. In this way, from the observers' point of view, the star looks like moving up and down in space. Modes with two surface nodes are called *quadrupole* modes. For the $l = 2, m = 0$ mode the nodes lie at latitudes $\pm 35^\circ$ (see Appendix B of Aerts et al. (2010) for the position of nodal lines of different modes). The poles of this mode swell up and heat up while the equator shrinks and cools, then vice versa. From Figure 1.3 it is obvious that the higher degree l of modes, the more sectors or zones will divide the stellar surface, with adjacent regions having opposite waving direction and opposite sign in intensity or velocity. As a result, the observed intensity or velocity, which represents the integrated quantities over the stellar surface, tends to be partially cancelled out. Therefore modes with higher degrees must be more difficult to detect than those with lower degrees. This is the so-called *partial cancellation*. Radial modes do not suffer from partial cancellation and their peak height reach about twice as high as a $l = 2$ modes. Modes with degrees higher than 2 are very rare to be observed.

The m specifies the number of longitudinal nodal lines and $|m| \leq l$, so for a spherically symmetric star the frequencies of all $2l + 1$ members of a multiplet are the same, if the star is not rotating. However, in *the co-rotating frame of reference frame* of the star, rotation leads to deviations from spherical symmetry which therefore lift this frequency degeneracy. The prograde modes travelling in the same direction as rotation have frequencies a little smaller than

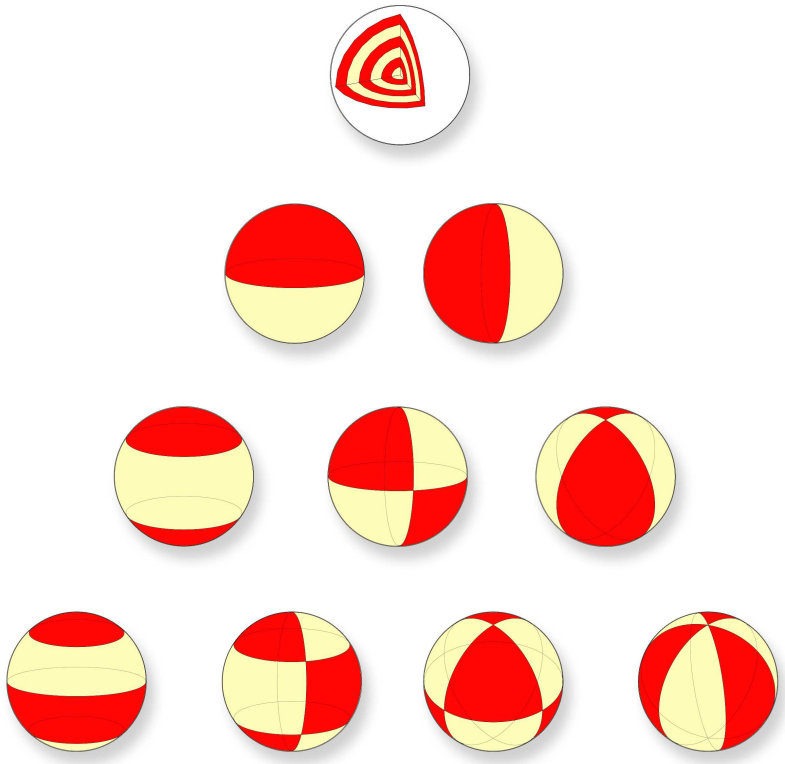

Figure 1.3: Exhibition of modes with different l and m. The stellar parts that have different movement directions are coloured differently. The top one shows the case of radial mode with couple of nodes inside the star. The other rows show the modes with different l. The second row is for dipolar modes, the left one is the case of $l = 1$ and $m = 0$, while the right one is $l = 1$ and $m = \pm 1$. The third row is for quadruple modes, and from left to the right shows $m = 0, \pm 1, \pm 2$. Similarly the last row shows the set of octupole modes, with $m = 0, \pm 1, \pm 2$ and ± 3. The sign of m is distinguished by rotation direction. Credit to Jing Xu.

the $m = 0$ mode, while the retrograde modes with opposite direction of rotation have slightly larger frequencies. This is due on the one hand by a Doppler effect that shifts the pulsation frequency in the inertial frame, and on the other hand by the Coriolis force that modifies the dynamics of pulsation modes, and thereby their frequency. The effect of rotation in oscillation frequencies was first investigated by Ledoux (1951). He developed the expression for the frequency of modes accounting for the rotational splitting, for a uniformly rotating star,

at first order, in the observer frame:

$$\nu_{nlm} = \nu_{nl0} + m\,(1 - C_{nl})\,\Omega/2\pi\,, \tag{1.6}$$

where ν_{nlm} is the observed frequency for a mode specified by n, l, m, ν_{nl0} is the mode with $m = 0$, which is unaffected by rotation and is the unperturbed central frequency of the multiplet, C_{nl} is a mode- and model-dependent coefficient (with value smaller than 1), and Ω is the angular velocity making the corresponding rotation frequency to be $\Omega/2\pi$. Eq. (1.6) can be rewritten as

$$\nu_{nlm} = \nu_{nl0} - mC_{nl}\Omega/2\pi + m\Omega/2\pi\,, \tag{1.7}$$

from which it is clear to see the reduction in frequency of prograde modes with positive m by the Coriolis force, but also the increase in that from the rotation frequency for the mode is propagating in the same direction of rotation. On contrary, modes with negative m are propagating against the rotation, therefore their frequency in the observer's frame are reduced by the rotation but increased by Coriolis force. Eq. (1.6) describes a multiplet with $2l + 1$ components separated by the *rotational splitting* $(1 - C_{nl})\,\Omega/2\pi$. However, uniform rotation is not real in stars. The rotational splitting and the components of the multiplet can be excited to different amplitudes, as a consequent, the observed spectrum can be very complicated.

1.3.2 The asymptotic relation for p modes

The asymptotic relations are very important in asteroseismology. The frequencies of low-degree (l) and high-order (n) p modes are regularly spaced, approximately following the asymptotic relation (Tassoul, 1980; Gough, 1986):

$$\nu_{nl} = \frac{\omega_{nl}}{2\pi} \simeq \Delta\nu(n + \tfrac{1}{2}l + \epsilon_{\rm p}) - d_{nl}\,, \tag{1.8}$$

where n is the radial order, l is the angular degree of the mode and ω_{nl} is the angular frequency. $\Delta\nu$ is known as the *large frequency separation*, which is the inverse sound travel time across the star, given by

$$\Delta\nu = \left(2\int_0^R \frac{{\rm d}r}{c}\right)^{-1}\,, \tag{1.9}$$

where c is the sound speed and R is the surface radius, and the integration is made over the distance r to the centre. In equation (1.8), $\epsilon_{\rm p}$ is a frequency-dependent phase shift due to the large gradient of the cut-off frequency near the stellar surface and d_{nl} is a correction called a small correction.

Figure 1.4 shows a power density spectrum of the flux variations observed over a time span of 13 months for the red giant star KIC 11618103 by *Kepler*. It

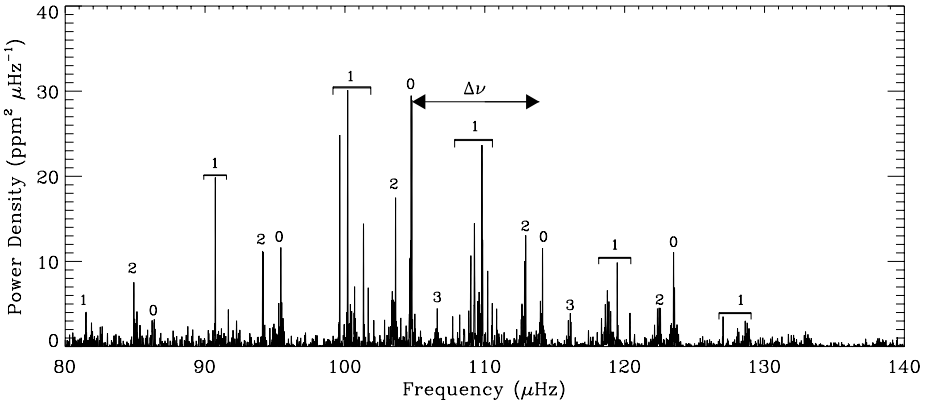

Figure 1.4: A power density spectrum of flux variations in the red giant star KIC 11618103 for 13 months of data taken with the *Kepler* space mission. The superimposed mode identification is provided by the modelling comparison. The large frequency separations are clearly shown.

presents the "comb" of mode frequencies of p modes described by Eq. (1.8). The very long-term observation of *Kepler* provides us the power spectrum with very high resolution but low noise. The power density spectrum in Figure 1.4 shows a bell-shaped envelope of power caused by the combination of damping and excitation, with a maximum power at a frequency $\nu_{\rm max}$ locating in the centre. Assuming the oscillations are adiabatic in an isothermal atmosphere, $\nu_{\rm max}$ is approximately related to the acoustic cut-off frequency $\nu_{\rm ac}$ in the atmosphere (Brown et al., 1991; Kjeldsen & Bedding, 1995),

$$\nu_{\rm max} \propto \nu_{\rm ac} \propto MR^{-2}T_{\rm eff}^{-1/2} \,, \tag{1.10}$$

where $T_{\rm eff}$ is the effective temperature of the star. In the solar photosphere $\nu_{\rm ac}$ is ~ 5.5 mHz (about 1.8 times the solar $\nu_{\rm max}$). The scaling of Eq. (1.10) has been supported by substantial observational results (e.g. Bedding & Kjeldsen, 2003; Stello et al., 2008), though it is not well understood theoretically (Belkacem et al., 2011).

The superimposed mode identification in Figure 1.4 was obtained after a series of modelling work which is introduced in Section 2.2. The value of $\Delta\nu$ is illustrated as the frequency separation between two consecutive radial modes. Unlike the radial and quadrupole modes that one of these modes corresponding to one peak, a set of multiplet of dipole modes cluster closely in a very small frequency range because of the effect of *avoided crossing* (discussed in Section 4.1). These dipole modes are mixed modes and they dominate the oscillation modes in evolved stars, such as in red giant stars. In the case of KIC 11618103, $\nu_{\rm max}$ is around 106 μHz and $\Delta\nu$ around 9.37 μHz. To a good approximation, $\Delta\nu$ is

proportional to the square root of the mean stellar density (Ulrich, 1986), as

$$\Delta\nu \propto M^{1/2}R^{-3/2}\,, \tag{1.11}$$

although White et al. (2011) pointed out that this scaling relation can be improved by including a function of $T_{\rm eff}$. Eqs. (1.10) and (1.11) can be rewritten as scaling relations from the accurate observed solar parameters (Kjeldsen & Bedding, 1995),

$$\frac{\nu_{\rm max}}{\nu_{\rm max,\odot}} \simeq \left(\frac{M}{M_\odot}\right)\left(\frac{R}{R_\odot}\right)^{-2}\left(\frac{T_{\rm eff}}{T_{\rm eff,\odot}}\right)^{-1/2} \tag{1.12}$$

$$\frac{\Delta\nu}{\Delta\nu_\odot} \simeq \left(\frac{M}{M_\odot}\right)^{1/2}\left(\frac{R}{R_\odot}\right)^{-3/2}\,. \tag{1.13}$$

In asteroseismology Eqs. (1.12) and (1.13) are widely used to approximate the radius and mass of a star with a little rearrangements to the equations

$$\frac{R}{R_\odot} \simeq \left(\frac{\Delta\nu}{\Delta\nu_\odot}\right)^{-2}\left(\frac{\nu_{\rm max}}{\nu_{\rm max,\odot}}\right)\left(\frac{T_{\rm eff}}{T_{\rm eff,\odot}}\right)^{1/2} \tag{1.14}$$

$$\frac{M}{M_\odot} \simeq \left(\frac{\Delta\nu}{\Delta\nu_\odot}\right)^{-4}\left(\frac{\nu_{\rm max}}{\nu_{\rm max,\odot}}\right)^{3}\left(\frac{T_{\rm eff}}{T_{\rm eff,\odot}}\right)^{3/2}\,. \tag{1.15}$$

Since $\Delta\nu$, $\nu_{\rm max}$ and $T_{\rm eff}$ can be obtained from observation, the radius and mass of a solar-like star may be easily estimated with the help of the well-known Solar parameters. The scaling relations give very good estimates for less evolved stars (Bedding & Kjeldsen, 2003), while Stello et al. (2008) have shown that they also hold for stars on the giant branch, although with larger uncertainties.

1.3.3 The asymptotic relation for g modes

Likewise, the *periods* of g modes satisfy an asymptotic relation (Tassoul, 1980):

$$\Pi_{nl} = \frac{2\pi}{\omega_{nl}} \simeq \Delta\Pi\,(n+\epsilon_{\rm g})\ , \tag{1.16}$$

where $\epsilon_{\rm g}$ is again a phase shift, n being the radial order and

$$\Delta\Pi = \frac{2\pi^2}{L}\left(\int_{r_1}^{r_2} N\frac{{\rm d}r}{r}\right)^{-1}\,, \tag{1.17}$$

where $L=\sqrt{l(l+1)}$, N is the Brunt-Väisälä frequency (or buoyancy frequency) and the integral is over the cavity where the g mode is trapped. However, the

asymptotic relations for both p and g modes are only valid for high-order modes ($n \gg l$). It is obvious that the periods of g modes are equally separated by $\Delta\Pi$, known as the *period spacing*. The definition of N is given by

$$N^2 = g\left(\frac{1}{\Gamma_1 p}\frac{\mathrm{d}p}{\mathrm{d}r} - \frac{1}{\rho}\frac{\mathrm{d}\rho}{\mathrm{d}r}\right) , \tag{1.18}$$

where p is the pressure, and

$$\Gamma_1 = \left(\frac{\partial \ln p}{\partial \ln \rho}\right)_{\mathrm{ad}} \tag{1.19}$$

is the adiabatic exponent (Cox, 1968; Weiss et al., 2004). The physical significance of N is well discussed in Aerts et al. (2010), Chapter 3. The convective *stability*, which is also the oscillatory case, requires that $N^2 > 0$. In this case, buoyancy forces the fluid element into an oscillation around the equilibrium. These oscillatory waves are indeed the internal gravity waves. In evolved stars the very compact core leads to a high value of g and hence N in the centre area of the star, such that oscillatory modes may have g-mode character in the interior while p-mode character in the outer part of the star. We will come back to discuss this in Section 1.4.

On contrary, N^2 is important to form a convective core in evolved star (see detailed discussion of convection in Section 1.3.4). In a helium-burning red clump star, a convective core is developed very close to the onset of central helium burning. The value of N^2 becomes negative in the convective core area and hence the period spacing $\Delta\Pi$ is much higher than that in the ascending-branch stage. In this way, we can distinguish red giants and clump stars based on the period spacings of modes (Bedding et al., 2011).

1.3.4 Convection

Presumably the ideal gas law is approximately valid for a fully ionized gas in the interior of cool stars, as

$$p = \frac{k_{\mathrm{B}}\rho T}{\mu m_{\mathrm{u}}} , \tag{1.20}$$

where k_{B} is Boltzmann's constant, T is the temperature, m_{u} is the atomic mass unit and μ is the mean molecular weight determined solely by the composition. By using Eq. (1.20), N^2 can be rewritten as

$$N^2 \simeq \frac{g^2\rho}{p}\left(\nabla_{\mathrm{ad}} - \nabla + \nabla_\mu\right) , \tag{1.21}$$

where

$$\nabla = \frac{\mathrm{d}\ln T}{\mathrm{d}\ln p}\ , \qquad \nabla_{\rm ad} = \left(\frac{\partial \ln T}{\partial \ln p}\right)_{\rm ad}\ , \qquad \nabla_\mu = \frac{\mathrm{d}\ln \mu}{\mathrm{d}\ln p}. \tag{1.22}$$

The condition for convective instability, $N^2 < 0$, becomes that

$$\nabla > \nabla_{\rm ad} + \nabla_\mu\ , \tag{1.23}$$

which is know as the *Ledoux criterion* of convective instability. Note that ∇_μ provides positive contribution to the stability, because typically μ increases with decreasing r and hence increasing p. However, since the chemical material is mixed in the convection region causing zero ∇_μ which would make the region become stable according to the Ledoux criterion. Such complications of ∇_μ motive the use of *Schwarzschild criterion* in a layer the that all energy is transferred by radiation, $\nabla = \nabla_{\rm rad}$, which is

$$\nabla_{\rm rad} > \nabla_{ad} \tag{1.24}$$

for an unstable region. The radiative temperature gradient is given by

$$\nabla_{\rm rad} = \frac{3}{16\pi a\tilde{c}G}\frac{\kappa p}{T^4}\frac{L(r)}{m(r)}\ . \tag{1.25}$$

where a is the radiation density constant, $\tilde{c}$ is the speed of light, κ is the opacity, G is gravitational constant, L and m are the luminosity and mass, both as a function of r. However, in convectively unstable regions part of the energy is transported by convection, therefore the actual temperature gradient ∇ is smaller than $\nabla_{\rm rad}$. It also may be argued that a intermediate case exists,

$$\nabla_{\rm ad} + \nabla_\mu > \nabla_{\rm rad} > \nabla_{\rm ad}, \tag{1.26}$$

such case is corresponding to the *semiconvection* motions.

From the Schwarzschild criterion and Eq. (1.25), we can summarize several favourable conditions for convection:

1. Large opacities, which leads to large $\nabla_{\rm rad}$;
2. Low γ, which leads to small $\nabla_{\rm ad}$ (in the case of idea gas $\gamma = \Gamma_1$, then $\nabla_{\rm ad} = \gamma/C_p, C_p$ being the specific heat at constant pressure);
3. Partial ionisation zones, which brings γ close to 1 and hence small $\nabla_{\rm ad}$ ($\nabla_{\rm ad} = 1 - 1/\gamma$);
4. Strongly temperature-dependent energy generation, such as the CNO cycle, which leads to large $\nabla_{\rm rad}$.

The detailed effects of the convective instability remain uncertain due to various complications. Models are often computed applying many approximations,

a typical example is the *mixing-length* formulation, which makes use of the mixing-length parameter to describe the convective flux, velocity, and temperature gradients of the convective elements and stellar medium. The mixing-length parameter is defined to be proportional to the local pressure scale height, and the mixing-length parameter must be determined by comparing the stellar models to some calibrator, usually the Sun. No strong arguments exist to suggest that the mixing-length parameter is the same in all stars and at all evolutionary phases. An analytical, non-local, time-dependent sub-sonic solution for the convective energy transport that does not depend on any free parameter was discussed by Pasetto et al. (2014).

1.4 Trapping of p and g modes

The oscillation displacement $\boldsymbol{\delta r}$ can be separated into radial and horizontal components, $\xi_{\rm r}$ and $\xi_{\rm h}$,

$$\boldsymbol{\delta r} = \xi_{\rm r}\boldsymbol{a}_{\rm r} + \boldsymbol{\xi}_{\rm h} \tag{1.27}$$

where $\boldsymbol{a}_r$ is a unit vector directed outward. Unno et al. (1989) introduced two variables v and w related to the displacement components as

$$v = \rho^{1/2} cr \left(\left| 1 - \frac{S_l^2}{\omega^2} \right| \right)^{-1/2} \xi_{\rm r} \tag{1.28}$$

and

$$w = \rho^{1/2} r^2 \omega^2 \left(|N^2 - \omega^2| \right)^{-1/2} \xi_{\rm h}, \tag{1.29}$$

where ω is the angular frequency of a mode. Neglecting the perturbation to the gravitational potential (the so-called Cowling approximation; Cowling, 1941), the two variables v and w each approximately satisfy a second-order differential equation that describes the behaviour of oscillations,

$$\frac{{\rm d}^2 v}{{\rm d}r^2} + K^2 v = 0 \tag{1.30}$$

and

$$\frac{{\rm d}^2 w}{{\rm d}r^2} + K^2 w = 0 \tag{1.31}$$

with K defined by

$$K^2 \approx \frac{\omega^2}{c^2} \left(1 - \frac{S_l^2}{\omega^2} \right) \left(1 - \frac{N^2}{\omega^2} \right). \tag{1.32}$$

Here K^2 is approximated by ignoring the acoustic cut-off frequency term that is generally small in the stellar interior and large near the surface. In equations (1.28) and (1.32), apart from N there is another characteristic frequency S_l,

also known as the Lamb frequency,

$$S_l^2 = \frac{l(l+1)c^2}{r^2}. \tag{1.33}$$

Unno et al. (1989) solved the set of differential equations (1.30) and (1.31) asymptotically to obtain v and w using the JWKB method (or Jeffreys, Wentzel, Kramers and Brillouin; Gough 2007). The local behaviour v and w in Eqs. (1.28) and (1.29) depends on the sign of K^2. Where $K^2 > 0$, they are locally oscillating functions of r, and where $K^2 < 0$ the solutions are locally exponentially increasing or decreasing functions of r. The solutions will be discussed in more detail in Section 4.1.3. Thus according to this description and Eq. (1.32) the solutions oscillate as a function of r when

$$\text{(o1)} \quad \omega^2 > N^2 \quad \text{and} \quad \omega^2 > S_l^2 \,, \tag{1.34}$$

$$\text{(o2)} \quad \omega^2 < N^2 \quad \text{and} \quad \omega^2 < S_l^2 \,, \tag{1.35}$$

and they are exponential when

$$\text{(e1)} \qquad N^2 > \omega^2 > S_l^2 \,, \tag{1.36}$$

$$\text{(e2)} \qquad S_l^2 > \omega^2 > N^2 \,, \tag{1.37}$$

The two oscillatory-behaviour solutions, (o1) and (o2) corresponding to the specific cases of acoustic and gravity waves in the star. Furthermore, the intersections between ω and the two characteristic frequencies, N and S_l, constrain the travelling regions for those two modes. The so-called propagation diagram of the model MS is plotted in Figure 1.5, where the cyclic N and S_l are plotted against radius fraction. According to the conditions of (o1) and (o2), the red bar indicates the p mode frequency region where ω is greater than both N and S_l, while the blue bar shows the g mode frequency region where ω is smaller than the two characteristic frequencies. The two coloured bars also confine the depth of trapping areas in the radial direction for the two types of waves.

For the regions that satisfy the exponential-behaviour solutions, (e1) and (e2), they are often the *evanescent* region, meaning that the mode is evanescent in the given region. The evanescent region is of great important for the analysis of mixed modes, detailed discussion will be given in Section 4.1.1.

1.5 Outline of this thesis

All the work presented in this thesis has done with the purpose of trying to understand the seismology of red giant stars, theoretically as well as practically.

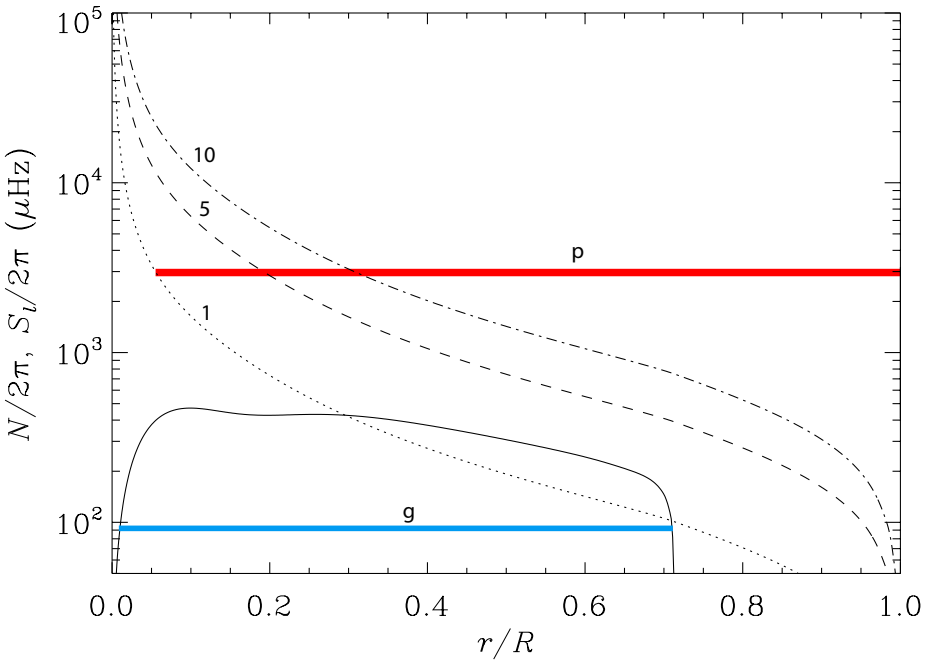

Figure 1.5: The so-called propagation diagram of the model MS in Figure 1.1 plotted as Buoyancy frequency N (continuous line) and Lamb frequency S_l (discontinuous lines for degree 1, 5 and 10, as labelled so in the diagram) as a function of the fractional radius r/R. The red bar shows the theoretical frequency region for p modes, which is also the typical observed frequency region for the Sun, while the blue bar shows the region for g modes. All the frequencies are in cyclic form.

In Chapter 2, we start the discussion of the asteroseismology in red giant stars practically by introducing the well-know space mission *Kepler*, which intends to discover Earth-like planets orbiting other stars. We present our analysis method for *Kepler* data that are used in our studies, including methods to treat the photometric data and the power spectrum. In addition, we discuss further how we extract the seismic parameters, such as $\Delta\nu$, ν_{max}, individual mode frequencies and so on, from the power spectrum. With those seismic results, we can easily estimates the global parameters of the stars, like their masses and radii. For more advanced analysis, if we know the effective temperature and the chemical composition of the stars, the seismic results can be compared with models, which gives good constraints of the stellar parameters. Such kind of work for the red giant stars in *Kepler* clusters are present. The detailed modelling is given in Chapter 3, followed with several studies of specific cases.

Finally, in Chapter 4 we also investigate the interior structure of red giant stars through the analysis of mixed modes. Since g modes normally have very

small amplitude compared with p modes for solar-like oscillations, they are very unlikely to be detected at the surface. However, the information of inner structure these g-mode waves carrying is of great important. As discussed in Section 1.3.3, mixed modes have g-mode character in the interior as well as p-mode character in the outer part, which make them significant enough to be observed. By analyzing these mixed modes, we can also gain some idea about the myth in the deep interior. Although this part of work is done mainly theoretically, some proofs of the utility for real stars are also given. We end this thesis with concluding remarks and future prospects in Chapter 5.

Chapter 2

Red Giant Stars in Kepler Field

The NASA *Kepler* Mission (Borucki et al., 2008, 2010) was successfully launched on March 7, 2009. Its primary scientific goal is to search for Earth-size planets in or near the habitable zone and to determine how many stars have this kind of planets in our Milky Way. *Kepler* is equipped with a 0.95-meter diameter telescope with an array of CCDs which continuously points to a large area of the sky in the constellations Cygnus and Lyra to detect the transits of the planets. Over the whole course of the mission, the spacecraft has been measuring the variations in the brightness of more than 100,000 stars, which are outstanding data for the study of asteroseismology. For many of these stars we can detect solar-like oscillations, which allow us to investigate them in detail and obtain their fundamental properties, by using the techniques of asteroseismology (Christensen-Dalsgaard et al., 2007; Aerts et al., 2010).

2.1 Data analysis

The *Kepler* mission observes the brightness change of a star and can provide us very high-precision photometric light curves. The targets are observed in two cadences, *short cadence* (sampling interval $\sim$ 58.89 s) and *long cadence* (sampling interval $\sim$ 29.4 min). The short cadence data with the *Nyquist* frequency $\sim$ 8500 μHz have maximum observable frequency that is high enough to detect solar-like oscillations in main-sequence stars. On the other hand the long cadence data (the Nyquist frequency $\sim$ 283 μHz) are helpful for the detection for solar-like oscillations in red giant stars. Therefor, we only introduce our work with long cadence data.

2.1.1 Time series reduction

Even though the *Kepler* photometric data are very ideal for asteroseismology study (Gilliland et al., 2010), they present a series of unwanted effects mainly from the instruments like most space based observation do. These effects may contaminate the time series and complicate our analysis. The first effect in the time series is the *outliers* probably coming from the cosmic and magnetic events. Additionally, long term trends in flux in terms of terms of temperature drifts are also presented in the data originating from the variation in the heating of the space craft. Gaps and jumps are seen between quarters because of the correction of direction of the telescope every quarter, which changes the position of the individual stars on the CCD focal plane, with different CCD having different sensitivity response function. Jumps are primarily CCD pixel sensitivity related issues. Therefore, these unwanted effects should be removed before we proceed with the analysis.

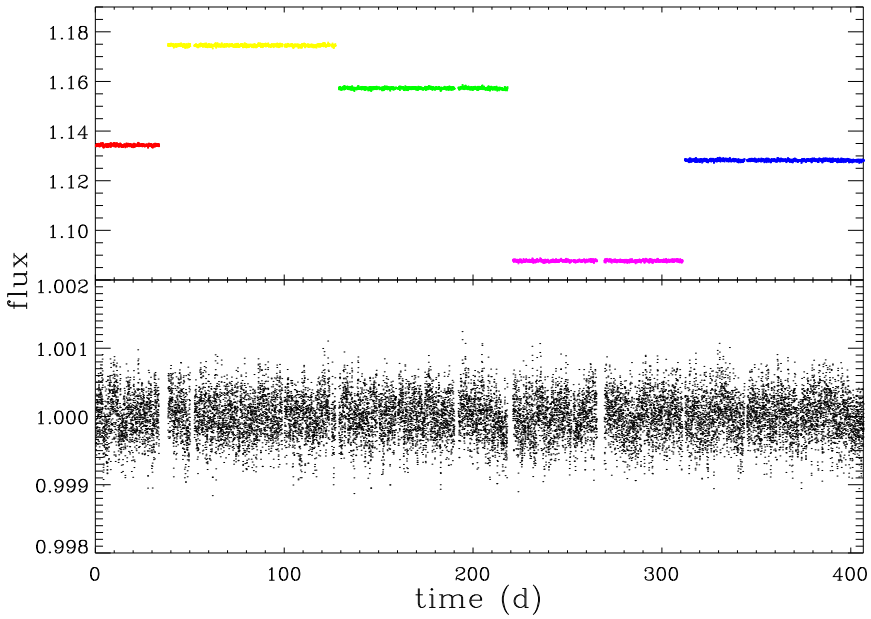

Figure 2.1: Upper panel, untreated light curve of the KIC 11618103 consists for the first five quarters data (13 months). Different quarter data are colored with different color. Lower panel, the same light curve as above treated by our data analysis pipeline, removing outliers, jumps and other unwanted trends.

Figure 2.1 presents the raw long-cadence light curve (upper panel) of a *Kepler* red giant star KIC 11618103 covering 13 months almost continuous data. However, very small gaps exist due to the safe mode of the spacecraft. We first

remove the outliers by performing a point-to-point sigma clipping and correct the thermal drift fitting a second-order polynomial to the affected parts of the time-series for each quarter. Then we normalize the flux to remove the big jumps between each quarter. The resulted light curve is shown in the lower panel of Figure 2.1 after these treatments. Although our automated data reduction pipeline is a bit crude, the signals in the solar-like oscillations frequency range are all preserved. A more delicate and systematic method is published by Handberg & Lund (2014).

2.1.2 Background of the power spectrum

The power spectrum describes how much a signal is at a frequency ω. A power spectrum can be generated from the reduced time series by using a discrete Fourier transform. However, the power spectrum does not exclude the effect of observation gaps which insert peaks that are not from oscillations into the frequency spectrum. Therefore we use the power density spectrum instead, which is calculated as the reciprocal of the area integrated under the spectral window and can be obtained easily by multiplying the power spectrum by the effective observation length in time.

The power spectrum shows a frequency-dependent background signal due to stellar activity, granulation and faculae which can be modelled by a sum of several Lorentzian-like functions (Harvey, 1985). In our spectrum treatment, the stellar activity, granulation and faculae were represented by modified Lorentzian-like functions, first introduced by Karoff (2008), which give a better fit to the background than a Harvey model with a constant slope of -2. This background model has a shallower slope at low frequencies and a steeper slope at higher frequencies, corresponding to stellar activity and granulation, respectively. The power excess hump from stellar oscillations is approximately Gaussian, so the complete spectrum was modeled by:

$$P(\nu) = P_n + \sum_{i=1}^{3} \frac{4\sigma_i^2 \tau_i}{1 + (2\pi\nu\tau_i)^2 + (2\pi\nu\tau_i)^4} + P_{\rm g} \exp\left(\frac{-(\nu_{\rm max} - \nu)^2}{2\sigma_{\rm g}^2}\right), \quad (2.1)$$

where P_n corresponds to the white noise component, σ_i is the rms intensity of the granules and τ_i is the characteristic time scale of granulation. For the Gaussian term, the parameters $P_{\rm g}$, $\nu_{\rm max}$, and $\sigma_{\rm g}$ are the height, the central frequency, and the width of the power excess hump.

Fig. 2.2 shows the fitted model for the KIC 11618103 power spectrum using Eq. (2.1). The three components of the background and the white noise were simultaneously fitted to a lightly smoothed power spectrum (Gaussian with FWHM of 0.5 μHz) outside the region where the power excess hump is seen. The value of $\nu_{\rm max}$ was obtained by fitting to a heavily smoothed power spectrum

(Gaussian with FWHM of 3 $\Delta\nu$, where $\Delta\nu$ is estimated in Sect. 2.1.3), giving 106.5 $\pm$ 0.3 μHz. Finally, the background and the white noise were subtracted from the power density spectrum, leaving only the oscillation signal. The power density spectrum of the KIC 11618103 with background removed was calculated and is shown in Figure 1.4, which is ready for next step to extract individual oscillation frequency and other seismic parameters from the spectrum.

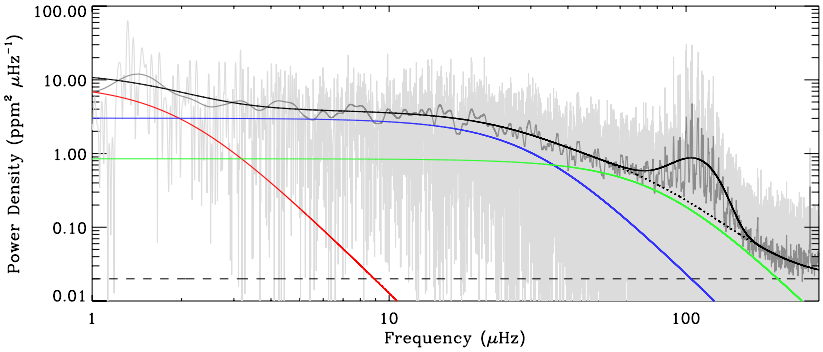

Figure 2.2: Power density spectrum of the combined first five quarters of data (light-grey) and corresponding global model fit(black line). The dark-grey line is the smoothed (Gaussian with a FWHM of 0.5 μHz) power density spectrum. The dotted line is the fitted background and the dashed line is the white noise. The red line shows the contribution from stellar activity, the blue from granulation and the green from faculae (Karoff, 2008).

2.1.3 Estimations for $\nu_{\max}$ and $\Delta\nu$

$\nu_{\max}$ normally locates closely to the frequency of the highest peak in the power spectrum, though it is defined as that frequency. The value of $\nu_{\max}$ and the shape of the power excess envelope are determined by the excitation and damping. The envelope is modelled by the last term of Eq. (2.1), which directly gives the valued of $\nu_{\max}$, as the central frequency of the Gaussian function.

As mentioned in Section 1.3.2, the frequencies of p modes are nearly equally spaced by the quantity $\Delta\nu$ which is, as labelled in the Figure 1.4, the frequency difference between modes with consecutive radial orders but the same degree. In reality, there are several ways to obtain $\Delta\nu$ from a power spectrum without knowing the frequencies of individual modes. We use a fraction of the background corrected power density spectrum where power excess presented to be applied with the two common methods to estimate $\Delta\nu$.

The first method is to calculate a power spectrum of the power spectrum,

(PS2 Kjeldsen & Bedding (1995)). Since the power spectrum can illustrate the periodicities of signals, the PS2 shows how the peaks repeat in frequency domain. However, there is always a $l = 1$ mode located nearly in the middle of two radial modes (see Figure 1.4), so the period of frequency peaks for solar-like oscillations in a power spectrum is actually half of the large frequency spacing. Figure 2.3 shows PS2 of KIC 11618103 with frequency range from 80 to 140 μHz. After performing a Fourier transform to the power spectrum, the series was transformed back to the time domain. The first highest peak is around 2.2×10^{-6} s which can be obtained by a Lorentzian fit to the peak. A series of peaks locating at multiple time points of the highest peak indicate the overtone of $\frac{1}{2}\Delta\nu$ in the power spectrum. For stars with relatively low quality data, the series of peaks may not be significant other than the first highest peak. Measuring this peak can lead to a little deviation for $\Delta\nu$.

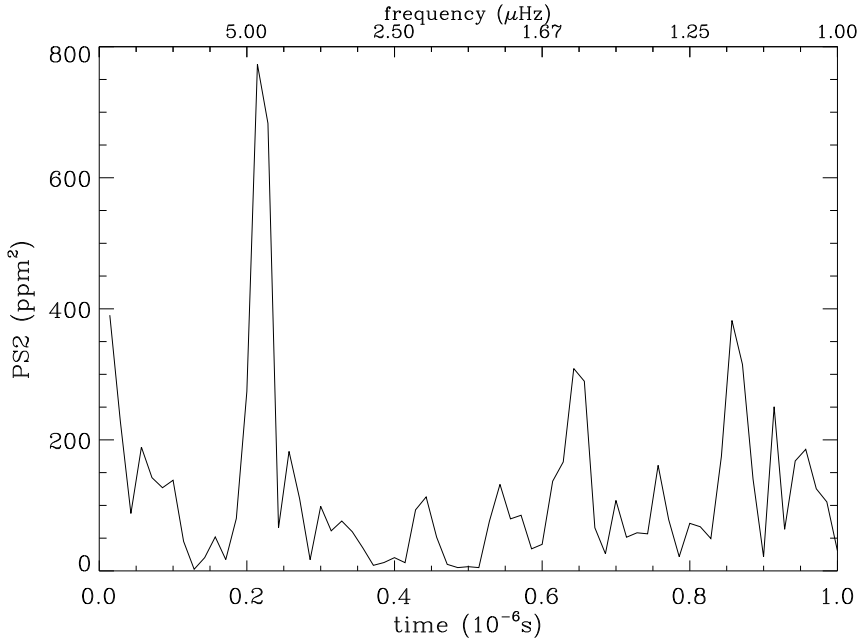

Figure 2.3: The power spectrum of the power spectrum of the KIC 11618103 time series. Only the fraction of the power spectrum with significant power excess is used in the generation of this plot. The highest peak corresponds to half of the large frequency separation.

The alternative method to estimate $\Delta\nu$ is the autocorrelation function, which is the cross-correlation of a power spectrum with itself. Informally, it is the similarity between observations as a function of the time lag between them. It is a mathematical tool to find the repeating patterns in a power spectrum, which is half to the $\Delta\nu$, for the same reason with PS2. The autocorrelation

Table 2.1: Results of $\Delta\nu$ from methods of autocorrelation(AC), PS2 and radial modes fitting (RM).

	AC	PS2	RM
$\Delta\nu$	9.07	9.36	9.37

as a function of the frequency lag is plotted in Figure 2.4. The results from autocorrelation and PS2 are given in Table 2.1.

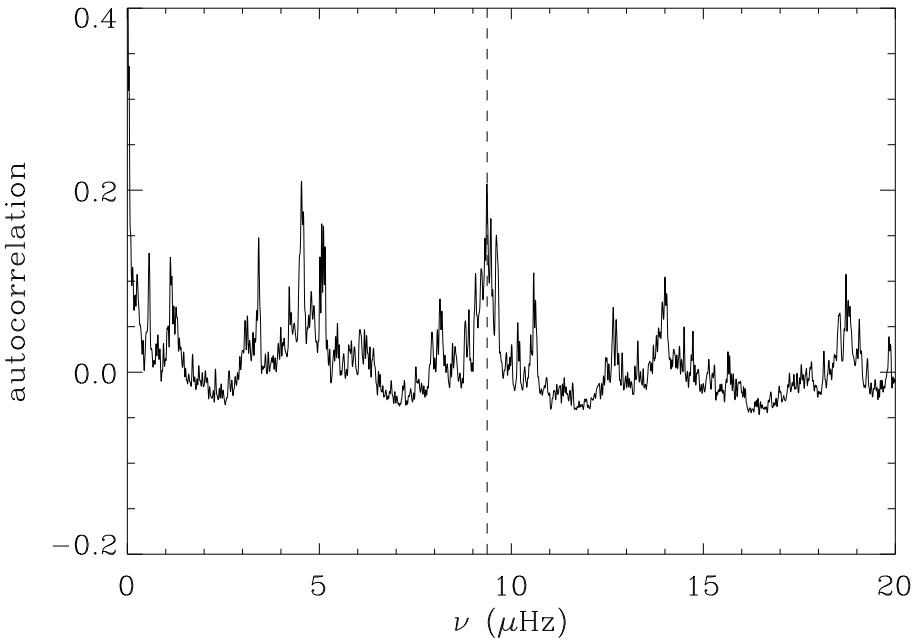

Figure 2.4: Autocorrelation function of the power spectrum for the KIC 11618103 against the frequency. A series of peaks corresponding to multiples of $\frac{1}{2}\Delta\nu$. The $\Delta\nu$ peak is guided by the dashed line.

The above two methods can be used to estimate $\Delta\nu$ without extracting individual mode frequency and hence they are widely included in automated pipelines for data analysis. They are very useful when the oscillation peaks are not significant and therefore their repeating patterns are not clear. Such cases are normal in short-term and low-precision observations where the noise level can be very high but the signals of oscillations are low. For a power spectrum with significant amplitudes, a number of modes with different radial orders become accessible. From the asymptotic relation for p mode frequency Eq. (1.8), we know that $\Delta\nu$ is the slope of that linear function. Therefore, if we plot the mode frequencies as a function of the radial order, the slope of that line, the $\Delta\nu$, can be estimated by performing a linear fit to the five

$l = 0$ modes. Frequencies for $l = 0$ modes are the most suitable ones for this calculation because they are not affected by the mixing with g-modes. In reality, $\Delta\nu$ is not a constant value, but varies with frequency. For higher-radial-order p modes, the difference of $\Delta\nu$ is quite small. The resulting $\Delta\nu$ from the linear fit to radial mode frequencies and orders is a mean value, which is usable for the asymptotic analysis. The last method actually dose not need to know the radial orders for the fitting. Several continuous integers can also do the work. But the frequencies of radial modes should be extracted from the power spectrum first.

2.2 Mode Identification from Kepler Data

The very high resolution and low noise level power spectra from *Kepler* provide us exquisite data for asteroseismology. These data are basically the oscillation frequencies, aside from the $\Delta\nu$ and $\nu_{\rm max}$ for the p modes as well as the period spacings $\Delta\Pi$ for the mixed modes that will be introduced in Section 4.1. Although my work does not involve much effort to derive frequencies from the power spectrum, we utilize the powerful software package called Period04 (Lenz & Breger, 2004) to extract the frequencies of individual oscillation modes. Period04 uses iterative sine-wave fitting, which does a good job of extracting frequencies in cases such as this where the individual modes are unresolved or barely resolved. The program analyzes the power spectrum within the power excess range and finds the highest peak in the range. Then the contribution of this peak to the power spectrum is in from a prewhitening process, after which a new highest peak can be found in the new power spectrum. The method can find all the significant peaks efficiently and precisely, but cannot provide any information about the mode identification. It fails to distinguish the signals of oscillations from those of other process, such as the frequency splittings caused by rotation. Therefore, we introduce a comprehensive way to identify these frequencies derived from the power spectrum.

It is basically not possible to gain any information about the mode identification directly from the peaks. However, from the asymptotic analysis we know the frequencies of oscillation modes have certain regular patterns in the power spectrum, with which the identification becomes feasible. For instance, the roughly equal spacings between p-mode frequencies can be used to predict locations of these p modes. In order to have an idea about the repeating pattern of these p modes, it is convenient to rewrite Eq. (1.8) for the radial modes and

modes of $l = 1$ and 2 separately,

$$\nu_{n,0} \simeq \Delta\nu(n + \epsilon_{\rm p}) - d_{n,0} \ , \tag{2.2}$$

$$\nu_{n,1} \simeq \Delta\nu(n + \tfrac{1}{2} + \epsilon_{\rm p}) - d_{n,1} \ , \tag{2.3}$$

$$\nu_{n,2} \simeq \Delta\nu(n + 1 + \epsilon_{\rm p}) - d_{n,2} \ . \tag{2.4}$$

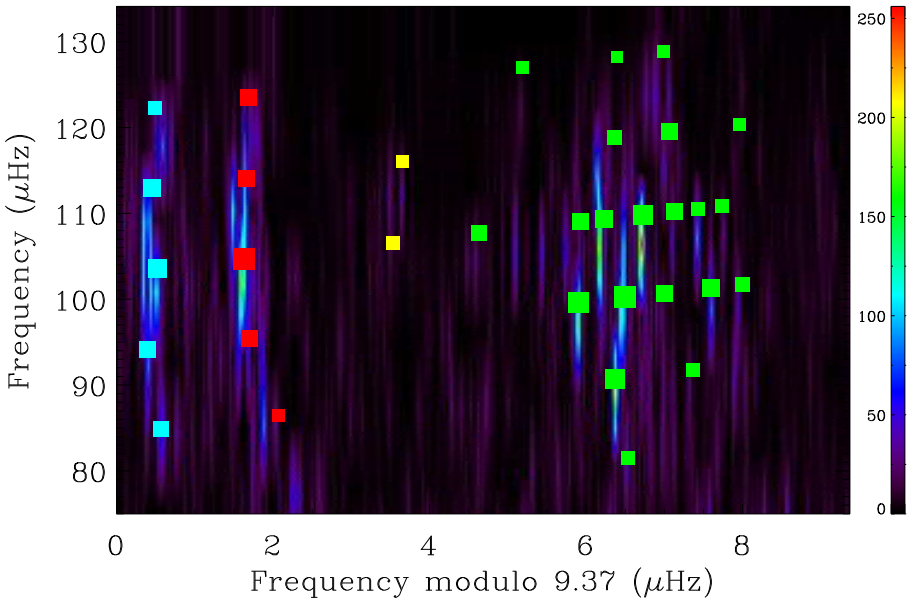

Figure 2.5: Échelle diagram for the KIC 11618103, based on Eq. (2.9); the frequencies are plotted against $\tilde{\nu}_{nl}$. The background is the power spectrum (*cf.* Figure 1.4) in the échelle form. The color of the background represents the amplitude, namely warmer color means higher amplitude. Squares are modes extracted from the power spectrum using Period04, their sizes are scaled from the amplitudes. Therefore the mode with highest amplitude is located around 105 µHz which is very close to the $\nu_{\rm max}$. Red, green, blue, yellow are used for modes of degree $l = 0, 1, 2, 3$.

The mean value of $\Delta\nu$ are not the exactly same for different degree modes, but the difference is quite small. Therefore, it is reasonable to apply the radial-mode $\Delta\nu$ to other degree modes. Here in the above equations, $\Delta\nu$ is from the linear fitting to the radial modes. It is also helpful to list the differences between

$l = 1,\ 2$ modes and the radial modes as

$$\nu_{n-1,2} - \nu_{n,0} \simeq -\left(d_{n,2} - d_{n,0}\right) \ , \tag{2.5}$$

$$\nu_{n,1} - \nu_{n,0} \simeq \tfrac{1}{2}\Delta\nu - (d_{n,1} - d_{n,0}), \tag{2.6}$$

here the difference between $\nu_{n,0}$, $\nu_{n-1,2}$ is the so-called *small frequency separation* $\delta\nu$, which is sensitive to the core condensation and hence to the age of the main-sequence star (Scherrer et al., 1983),

$$\delta\nu \simeq \nu_{n,0} - \nu_{n-1,2} \ , \tag{2.7}$$

while the large frequency separation is

$$\Delta\nu \simeq \nu_{n+1,0} - \nu_{n,0} \ . \tag{2.8}$$

From the above relations between different modes, it is clear to image their pattern in a power spectrum asymptotically. For a radial mode with order n, a $l = 2$ mode with $n - 1$ order sits to its left with a frequency spacing of $\delta\nu$ and a $l = 1$ mode with the same radial order n appears to its right at a distance of $\frac{1}{2}\Delta\nu$. To illustrate the properties of this pattern in more comprehensive way, it is useful to utilize an *échelle diagram* (Grec et al., 1983), in which the frequencies are reduced modulo $\Delta\nu$ by expressing them as

$$\nu_{nl} = +k\Delta\nu + \tilde{\nu}_{nl} \ , \tag{2.9}$$

where k is an integer so that $\tilde{\nu}_{nl}$ is between 0 and $\Delta\nu$. Therefore the échelle diagram is plotted as ν_{nl} against $\tilde{\nu}_{nl}$. Figure 2.5 shows the power spectrum in the échelle format, given in Eq. (2.9), together with the extracted modes with different degrees from the power spectrum. Modes with the same degree are illustrated in the same color. It is not surprising to find modes with the same degree stacking up vertically in this diagram, except for the dipolar modes due to their mixed character. The $l = 0$ and 2 ridges locate close to each other by the small distance of $\delta\nu$, with $l = 2$ modes being to the left of radial modes. The dipolar modes are supposed to be to the right of radial modes with a distance of about half of the $\Delta\nu$. Here due to the effect of mixed modes, the dipolar modes spread about on that location. It is more illustrative to plot the mixed modes in the period échelle diagram instead of this frequency échelle, because they are equally spaced in period. However, for a sub-giant star, the avoided crossing can be clearly seen in the frequency échelle diagram (Bedding, 2012). The sizes of the modes plotted in Figure 2.5 are scaled from their amplitudes. The mode with the highest amplitude is a radial mode and is very close to the $\nu_{\max}$. The observed amplitudes are much smaller for higher degree l modes than for lower degree modes because of the effect of partial cancellation. Therefore, only two octupole modes are extracted from the power spectrum. Figure 2.6

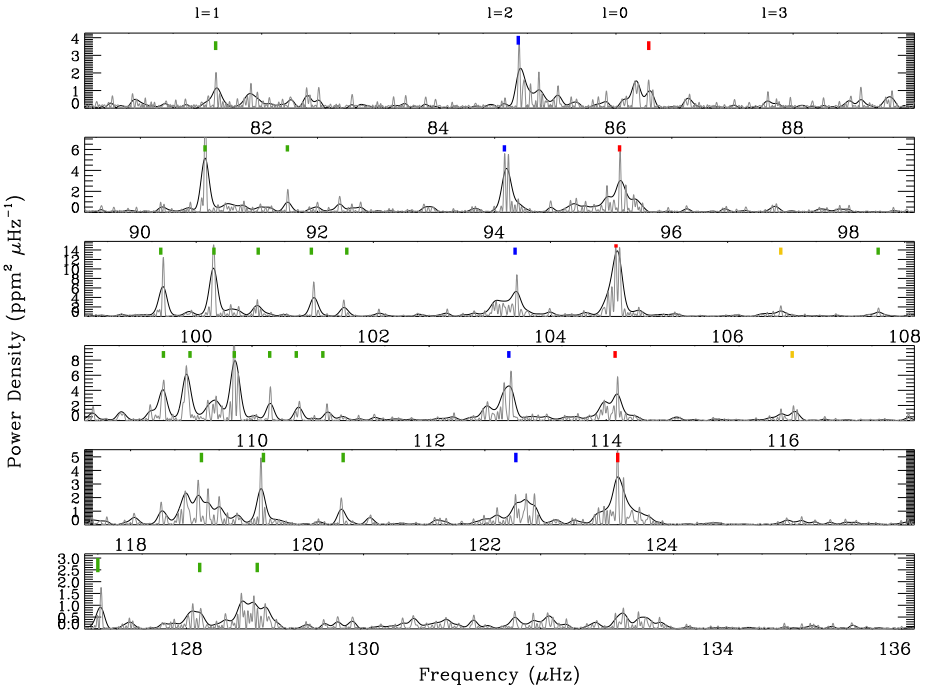

Figure 2.6: The échelle diagram of the smoothed power density spectrum (dark, FWHM of 0.1 μHz) and the unsmoothed background corrected power density spectrum (grey, power divided by a factor of 2) divided into bins each $\Delta\nu$ wide. The colored bars indicate 33 modes in Figure 2.5, with $l = 0$ modes in red, $l = 1$ ones in green, $l = 2$ ones in blue and two $l = 3$ modes in yellow. The peaks for the same degree almost line up. The offset from perfect alignment is caused by the variation of the large frequency spacing with frequency. Multiple peaks for $l = 1$ mixed modes can be seen clearly.

shows another version of échelle diagram by dividing the power spectrum into segments each $\Delta\nu$ wide and stacking them up so that modes with the same degree lie atop of each other.

Once we have a good estimation of $\Delta\nu$ we can get a preliminary idea of the mode identifications by plotting the extracted frequencies. However, rotation and mixed modes can shift the location of peaks making the power spectrum complicated. Therefore, an ideal method for mode identification is using the help of modelling which is crucial in asteroseismology study, which will be introduced in Section 3.1. Alternatively, for the purpose of peak bagging, which is a technique to extract frequencies directly from the power spectrum but much more sophisticated than what we are using in this thesis, applying the asymptotic relations for solar-like oscillations also helps to identify mode more correctly (*cf.* Handberg & Campante 2011).

2.3 Asteroseismology of Kepler Open Clusters

With the techniques introduced in the last section, we are able to analyse the observed time series with the intension of obtaining some seismical parameters, such as the $\Delta\nu$, $\nu_{\rm max}$, and mode frequencies. In this section, we demonstrate the result of the red giant stars of the Open Clusters, NGC 6791, NGC 6811 and NGC 6819, using the *Kepler* data. Many recent studies of solar-like oscillations of red giant stars have been focused on those three open clusters in the *Kepler* field (Basu et al. 2011; Hekker et al. 2011; Stello et al. 2011; Corsaro et al. 2012; Miglio et al. 2012). Stars in a certain cluster are formed from the same interstellar cloud of gas and dust at the same time and hence it is reasonable to assume that all stars in this cluster share the same age, distance and metallicity. This knowledge is an excellent advantage that allows for stringent verification of stellar evolution theory. The large number of stars in the cluster also provide good samples for investigation of stellar interior structure.

2.3.1 Observations

Solar-like oscillations have been detected in K giants in the open cluster M67 (Stello et al., 2007) and the globular clusters 47 Tuc (Edmonds & Gilliland, 1996) and NGC 6397 (Stello & Gilliland, 2009a). The first study about cluster

in the *Kepler* field of view was performed by Stello et al. (2010) for the open cluster NGC 6819. By now the *Kepler* time-series photometry cover 17 quarters of the observation time, which is about 49 months long. Although not all the stars in the three *Kepler* open clusters, NGC 6791, NGC 6811 and NGC 6819, are observed the whole time, *Kepler* data are precise enough for extracting reliable seismic parameters, while the data prior to *Kepler* failed to do so but could only reveal the presence of the oscillations.

We analysis the time series to obtain the global oscillation parameters using the method introduced in last section. First, we merge the time series for all the quarters for a certain star in the cluster while eliminating the outliers, removing the long-term systematic trend and normalizing them. The resulting time series are then transformed into the frequency domain through a Fourier transform. After removing the background, the power spectra are ready for further analysis. We studied 89 stars belonging to the three clusters (52 in NGC 6791, 32 in NGC 6819 and 5 in NGC 6811) and obtained reliable $\Delta\nu$ and $\nu_{\rm max}$ for 67 of them. Figure 2.7 shows 10 examples of the power spectra from NGC 6791. The power spectra are background removed with the above mentioned procedure, though high noise can still be seen at low frequency range, which is a known issue for *Kepler* data. Therefor, *Kepler* data are not good enough for the study of low-frequency oscillations, such as g modes and oscillations in evolved red giants. Solar-like oscillations are clear for the spectra in the figure and also for other

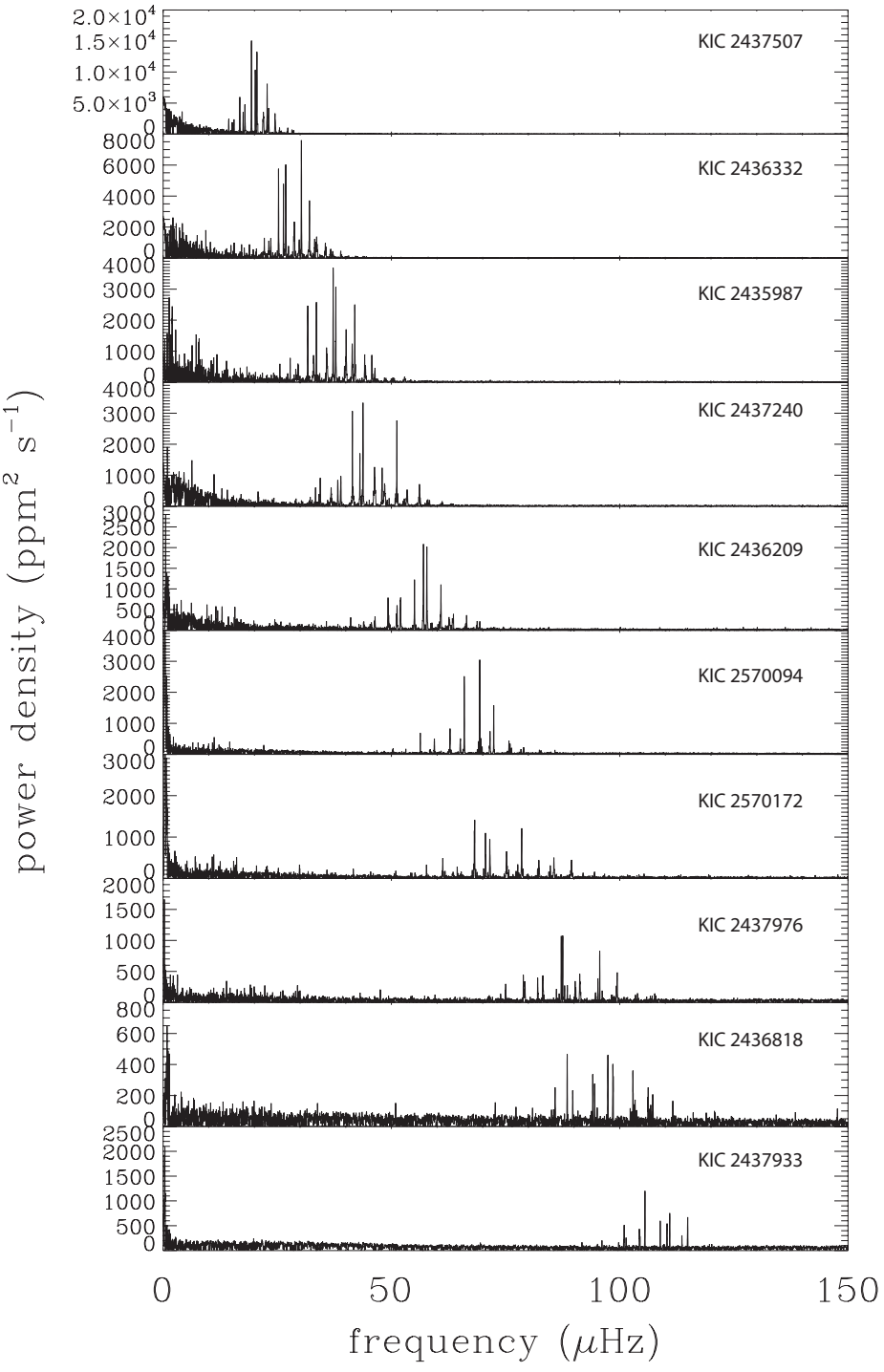

Figure 2.7: Power spectra of 10 stars in NGC 6791, with $\nu_{\rm max}$ increasing from the top to the bottom. Solar-like oscillations are clear on the spectra. The $\nu_{\rm max}$ and $\Delta\nu$ are listed in Table 2.2.

59 stars, which enables us to obtain the seismic parameters easily and they are listed in Table 2.2 for NGC 6791, Table 2.3 for NGC 6819 and Table 2.4 for NGC 6811. The $\nu_{\rm max}$ we obtained for all the data cover a large range, the lowest end is 7.8 μHz and the highest one is 159.6 μHz. Accordingly, the $\Delta\nu$ are in the range of 1.15 μHz to 11.98 μHz. The differences in these two parameters for the targets mean that the stars occupy different positions along the red giant branch, some of them are also clump stars. In this thesis, we only study the stars ascending the red giant branch and the targets in Table 2.2 and Table 2.3 are all RGB, but the 5 stars of NGC 6811 in Table 2.4 are clump stars. We made the selection of RGB by using the classification for RGB and clump stars given by Stello et al. (2011). As the star evolve along the ascending branch, the luminosity increase rapidly, the star keep expanding and therefore the mean density decrease. $\Delta\nu$ and $\nu_{\rm max}$ also become smaller for more evolved RGB. .

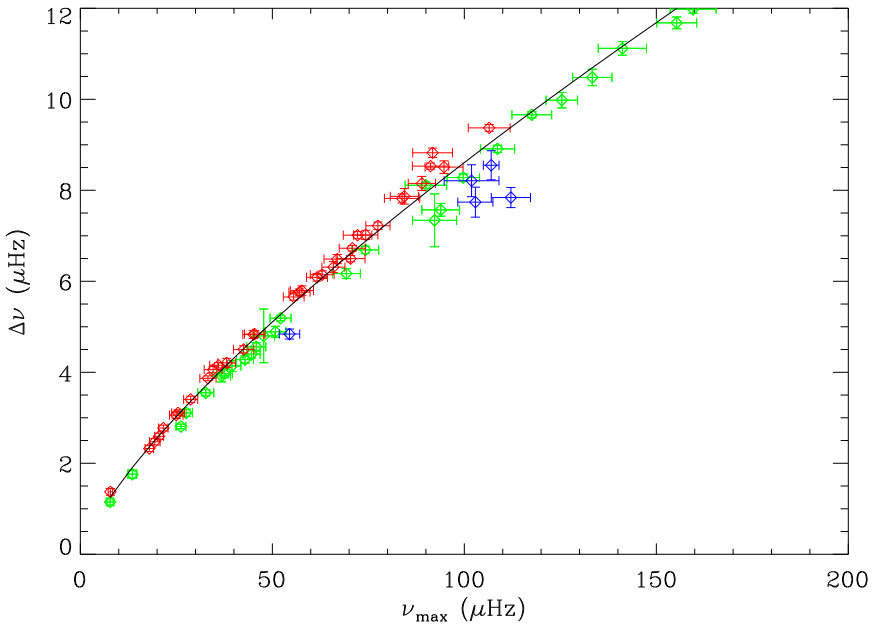

Figure 2.8: $\Delta\nu$ vs. $\nu_{\rm max}$ for the targets in the cluster NGC 6791 (red), NGC 6819 (green) and NGC 6811 (blue), with the fit through all the data.

The large sample of giant seismic data provide us opportunity to explore the relation between $\Delta\nu$ and $\nu_{\rm max}$. As already pointed by (Stello et al., 2009b) and (Huber et al., 2010), the two parameters follow a tight power-law relation:

$$\Delta\nu \simeq a\nu_{\rm max}^{b} \,, \tag{2.10}$$

where $\nu_{\rm max}$ is in the unit of μHz, a and b are open coefficient. After a fit to the giants we got from the three open clusters (*cf.* Figure 2.8, we derived a

result of $a = 0.267 \pm 0.004$ and $b = 0.754 \pm 0.004$, which is in good agreement, for a but not for b, with what (Stello et al., 2009b) got from a fit to red giants and main-sequence stars ($a = 0.263 \pm 0.009$, $b = 0.772 \pm 0.005$). Hekker et al. (2009) also measured this relation for *CoRoT* red giants ($\nu_{\rm max} < 100\mu$Hz) and the work is followed by Mosser et al. (2010) who found a set of [a, b] as $[0.28 \pm 0.02, 0.75 \pm 0.01]$. The latter considered a significant larger sample of data with lower error bars than the former and they did not scale the relation to the solar values of $\Delta\nu$ and $\nu_{\rm max}$. There exponent b is consistent with ours because we both measure the relation for RGB. However, the power-law relation between $\Delta\nu$ and $\nu_{\rm max}$ depends on mass and effective temperature. In order to investigate this dependance Hekker et al. (2011) divide the field sample of the same clusters as ours into low- and high-mass group with a threshold of 1.5 $M_{\odot}$ and derived different set of [a,b] for the two groups, $[0.282 \pm 0.003, 0.754 \pm 0.002]$ for the low-mass sample and $[0.262 \pm 0.005, 0.753 \pm 0.005]$ for the high-mass one. Our value of a is more in line with that obtained for higher-mass sample. Basu et al. (2011) estimated model-independant the average mass of NGC 6791 and NGC 6819 red giants to be $1.20 \pm 0.01 M_{\odot}$ and $1.68 \pm 0.03 M_{\odot}$, respectively. The difference in our value a may be due to the higher masses stars in NGC 6819 and the different mass distributions. We also have 5 clump stars of NGC 6811 in the sample, of which the stars have even larger masses than those of NGC 6819. In addition to study the mass dependence of the $\Delta\nu - \nu_{\rm max}$ relation, Hekker et al. (2011) also verified the influence of metallicity on the relation.

Table 2.2: Properties of NGC 6791.

KIC ID	$\nu_{\rm max}$ (μHz)	$\Delta\nu$ (μHz)	$\Delta\nu_{\rm sc}$ (μHz)	$\nu_{\rm max,sc}$ (μHz)	$T_{\rm eff}$ (B-V) (K)	$T_{\rm eff}$ (V-K) (K)	$\log L/L_{\odot}$	BC
2435987	38.1 ± 2.3	4.21 ± 0.10	35.3	4.0	4357	4363	1.60	-0.71
2436097	42.5 ± 2.6	4.50 ± 0.08	40.1	4.4	4369	4369	1.55	-0.70
2436209	57.1 ± 2.8	5.76 ± 0.07	53.3	5.5	4537	4491	1.46	-0.61
2436332	28.7 ± 1.8	3.40 ± 0.07	27.0	3.3	4374	4305	1.70	-0.76
2436458	36.0 ± 2.3	4.16 ± 0.06	35.1	4.0	4393	4336	1.60	-0.73
2436540	57.7 ± 3.0	5.80 ± 0.10	53.8	5.6	4507	4445	1.44	-0.64
2436688	77.5 ± 3.2	7.22 ± 0.08	73.7	7.1	4577	4530	1.34	-0.58
2436814	25.4 ± 1.7	3.11 ± 0.07	24.6	3.0	4359	4291	1.73	-0.77
2436818	91.7 ± 5.2	8.82 ± 0.10	93.6	8.5	4654	4543	1.24	-0.57
2436824	33.2 ± 2.1	3.87 ± 0.05	33.3	3.8	4366	4322	1.61	-0.75
2436900	34.6 ± 2.3	4.06 ± 0.07	35.5	4.1	4445	4404	1.61	-0.68
2437040	25.0 ± 1.8	3.06 ± 0.08	28.8	3.4	4354	4258	1.65	-0.57
2437240	45.4 ± 2.7	4.84 ± 0.08	44.2	4.8	4484	4436	1.53	-0.65
2437270	70.4 ± 3.8	6.50 ± 0.07	59.1	6.0	4458	4533	1.43	-0.58
2437325	94.7 ± 4.9	8.51 ± 0.14	89.4	8.1	4856	4445	1.22	-0.64
2437340	7.8 ± 0.6	1.37 ± 0.07	8.3	1.3	3984	3982	2.09	-1.15
2437402	45.0 ± 2.7	4.83 ± 0.09	43.4	4.7	4458	4413	1.53	-0.67
2437444	19.4 ± 1.4	2.47 ± 0.07	17.5	2.3	4261	4184	1.84	-0.89
2437488	65.9 ± 3.0	6.31 ± 0.12	58.9	6.0	4516	4454	1.41	-0.64
2437507	20.5 ± 1.1	2.59 ± 0.07	19.6	2.6	4312	4243	1.81	-0.82
2437653	72.2 ± 3.7	7.01 ± 0.08	69.8	6.8	4536	4483	1.34	-0.61
2437781	83.8 ± 4.6	7.82 ± 0.10	75.0	7.1	4539	4453	1.30	-0.64
2437816	18.0 ± 1.1	2.33 ± 0.07	17.0	2.3	4286	4214	1.86	-0.85

Table 2.2 – continued

KIC ID	$\nu_{\rm max}$ (μHz)	$\Delta\nu$ (μHz)	$\Delta\nu_{\rm sc}$ (μHz)	$\nu_{\rm max,sc}$ (μHz)	$T_{\rm eff}$ (B-V) (K)	$T_{\rm eff}$ (V-K) (K)	$\log L/L_\odot$	BC
2437933	106.5 ± 5.4	9.37 ± 0.08	106.8	9.4	4620	4606	1.20	-0.53
2437957	91.2 ± 4.7	8.53 ± 0.07	92.9	8.5	4620	4598	1.26	-0.53
2437972	84.4 ± 3.7	7.87 ± 0.17	77.9	7.4	4612	4541	1.32	-0.57
2437976	88.9 ± 3.6	8.15 ± 0.15	83.5	7.8	4590	4523	1.28	-0.58
2438038	63.0 ± 3.1	6.15 ± 0.08	58.8	6.0	4503	4451	1.41	-0.64
2438140	70.8 ± 3.4	6.73 ± 0.06	69.8	6.8	4541	4542	1.36	-0.57
2438333	61.6 ± 2.7	6.09 ± 0.08	59.6	6.0	4489	4499	1.42	-0.60
2569360	21.6 ± 1.2	2.77 ± 0.07	21.1	2.7	4317	4256	1.78	-0.81
2569618	55.6 ± 2.7	5.66 ± 0.07	54.2	5.6	4541	4496	1.46	-0.60
2570094	66.9 ± 3.5	6.49 ± 0.10	64.5	6.4	4518	4482	1.38	-0.61
2570172	74.3 ± 3.2	7.02 ± 0.10	70.0	6.8	4543	4499	1.35	-0.60

Table 2.3: Properties of NGC 6819.

KIC ID	$\nu_{\rm max}$ (μHz)	$\Delta\nu$ (μHz)	$\Delta\nu_{\rm sc}$ (μHz)	$\nu_{\rm max,sc}$ (μHz)	$T_{\rm eff}$ (B-V) (K)	$T_{\rm eff}$ (V-K) (K)	$\log L/L_{\odot}$	BC
4937576	32.7 ± 2.1	3.55 ± 0.07	30.1	3.32	4559	4490	1.86	-0.75
4937770	93.8 ± 4.9	7.57 ± 0.14	86.0	7.48	4991	4797	1.50	-0.31
4937775	92.3 ± 5.7	7.34 ± 0.58	83.6	7.41	5144	4942	1.56	-0.39
5023732	27.5 ± 1.6	3.11 ± 0.08	25.5	2.94	4591	4527	1.94	-0.72
5023845	108.6 ± 4.5	8.91 ± 0.08	100.7	8.40	4844	4771	1.42	-0.55
5023931	50.8 ± 2.7	4.89 ± 0.12	46.2	4.63	4707	4632	1.72	-0.64
5024143	117.6 ± 5.2	9.66 ± 0.07	111.8	9.07	4872	4747	1.37	-0.53
5024240	159.6 ± 6.0	11.98 ± 0.09	157.0	11.81	4952	4862	1.26	-0.49
5024297	45.8 ± 2.5	4.56 ± 0.09	43.3	4.40	4693	4579	1.73	-0.64
5024312	90.0 ± 5.4	8.11 ± 0.07	91.4	7.78	4835	4707	1.45	-0.55
5024404	47.8 ± 2.8	4.80 ± 0.59	43.3	4.41	4716	4617	1.74	-0.63
5024405	99.7 ± 4.2	8.28 ± 0.08	92.8	7.84	4784	4670	1.43	-0.58
5024512	74.2 ± 3.5	6.69 ± 0.08	73.8	6.63	4852	4720	1.54	-0.54
5024583	36.8 ± 2.3	3.92 ± 0.13	34.6	3.70	4620	4528	1.81	-0.70
5024750	13.5 ± 1.2	1.76 ± 0.09	11.6	1.61	4431	4378	2.23	-0.87
5111718	133.3 ± 5.1	10.48 ± 0.18	127.6	10.10	4933	4849	1.35	-0.50
5111940	52.1 ± 2.7	5.19 ± 0.06	50.3	4.96	4735	4666	1.69	-0.62
5112072	125.4 ± 4.1	9.98 ± 0.17	121.6	9.73	4926	4836	1.36	-0.50
5112361	69.3 ± 3.6	6.17 ± 0.11	59.8	5.70	4946	4812	1.67	-0.49
5112403	141.2 ± 6.3	11.12 ± 0.15	140.6	10.84	4939	4822	1.30	-0.50
5112734	39.5 ± 2.3	4.14 ± 0.12	37.0	3.88	4640	4523	1.78	-0.68
5112744	44.6 ± 2.2	4.40 ± 0.09	40.8	4.20	4662	4567	1.75	-0.67
5112786	7.8 ± 0.8	1.15 ± 0.07	6.7	1.04	4265	4187	2.41	-1.08
5112880	26.2 ± 1.3	2.81 ± 0.05	19.4	2.38	4527	4453	2.04	-0.78

Table 2.3 – continued

KIC ID	$\nu_{\rm max}$ (μHz)	$\Delta\nu$ (μHz)	$\Delta\nu_{\rm sc}$ (μHz)	$\nu_{\rm max,sc}$ (μHz)	$T_{\rm eff}$ (B-V) (K)	$T_{\rm eff}$ (V-K) (K)	$\log L/L_{\odot}$	BC
5112948	42.9 ± 2.2	4.28 ± 0.08	38.5	4.02	4640	4564	1.78	-0.68
5113041	37.5 ± 2.1	3.97 ± 0.09	36.3	3.84	4645	4527	1.79	-0.68
5113441	155.3 ± 5.2	11.68 ± 0.13	161.9	12.04	4895	4812	1.23	-0.40

Table 2.4: Properties of NGC 6811.

KIC ID	$\nu_{\rm max}$ (μHz)	$\Delta\nu$ (μHz)	$\Delta\nu_{\rm sc}$ (μHz)	$\nu_{\rm max,sc}$ (μHz)	$T_{\rm eff}$ (B-V) (K)	$T_{\rm eff}$ (V-K) (K)	$\log L/L_\odot$	BC
9534041	112.1 ± 5.1	7.84 ± 0.22	115.7	8.79	6012	5453	1.76	-0.15
9655101	102.9 ± 4.6	7.74 ± 0.33	107.0	8.27	5291	5418	1.78	-0.16
9655167	101.9 ± 7.1	8.21 ± 0.35	105.4	8.07	5322	5245	1.74	-0.21
9716090	107.0 ± 2.0	8.55 ± 0.32	107.7	8.11	5777	5075	1.68	-0.27
9716522	54.5 ± 2.7	4.84 ± 0.11	51.2	4.67	5343	5139	2.02	-0.25

2.3.2 Estimates of Effective Temperature

We used the metallicity-dependent temperature vs. color calibrations by Ramírez & Meléndez (2005) to estimate the effective temperature for all the targets in Table 2.2, 2.3 and 2.4. First we determine the temperatures based on the $(B-V)$ color. We obtained the B and V band photometry from Stetson et al. (2003) for NGC 6791, V band and $(B-V)$ color from Hole et al. (2009), B and V band from the Tycho-2 catalogue (Høg et al., 2000). Therefore, we have V band and observed $(B-V)_{\rm obs}$ color for all the three clusters. Then the intrinsic $(B-V)$ of the targets can be derived by

$$(B-V) = (B-V)_{\rm obs} - E(B-V)\ , \tag{2.11}$$

where $E(B-V)$ is the reddening index, which helps to correct the color index from interstellar extinction, due to the light scattering off dust and other matter in the interstellar medium. The adopted average cluster reddening of $E(B-V)$ is given in Table 2.5. In the table, the source of $E(B-V)$ is Brogaard et al. (2011), Bragaglia et al. (2001), and Lindoff (1972) for NGC 6791, NGC 6819, NGC 6811, respectively.

Table 2.5: Adopted parameters for the three clusters in this thesis.

Cluster	$E(B-V)$	$E(V-K)$	$(m-M)_0$
NGC 6791	0.16	0.432	13.11
NGC 6819	0.15	0.405	11.85
NGC 6811	0.16	0.435	10.3

After the reddening correction, we plot the color-magnitude diagrams of the targets in Figure 2.9. All our targets are bright enough to have JHK photometry from the 2MASS catalog (Skrutskie et al., 2006), allowing us to gain the $(V-K)$ color index which is also plotted in the color-magnitude diagram of Figure 2.9 after removing the reddening $E(V-K)$ (Hekker et al., 2011, see Table 2.5). Using the Ramírez & Meléndez (2005) color-temperature calibrations we then transformed the $(B-V)$ and $(V-K)$ color indices to $T_{\rm eff}$, respectively. We adopted the way that Hekker et al. (2011) estimated the uncertainty in $T_{\rm eff}$ to be 110 K including the contributions from photometry, reddening estimations and color-temperature relations. We compare the $T_{\rm eff}$ derived from $(V-K)$ color with those from $(V-K)$ and plot the results in Figure 2.10. One outlier exists for NGC 6791, KIC 2437325, appears to be much cooler in $(V-K)$ than it does in $(B-V)$. For NGC 6891, the difference is not significant for all the targets, though $(B-V)$ temperatures seem higher than the $(V-K)$ ones for most of the stars. The outliers in Stello et al. (2011) are not included in our sample, so we are not able to verify them, but otherwise the temperatures are in good agreement with their results. Stello et al. (2011) pointed out that the $(V-K)$ color index is generally the better temperature proxy for cool red giants, so we use temperatures from $(V-K)$ for further analysis.

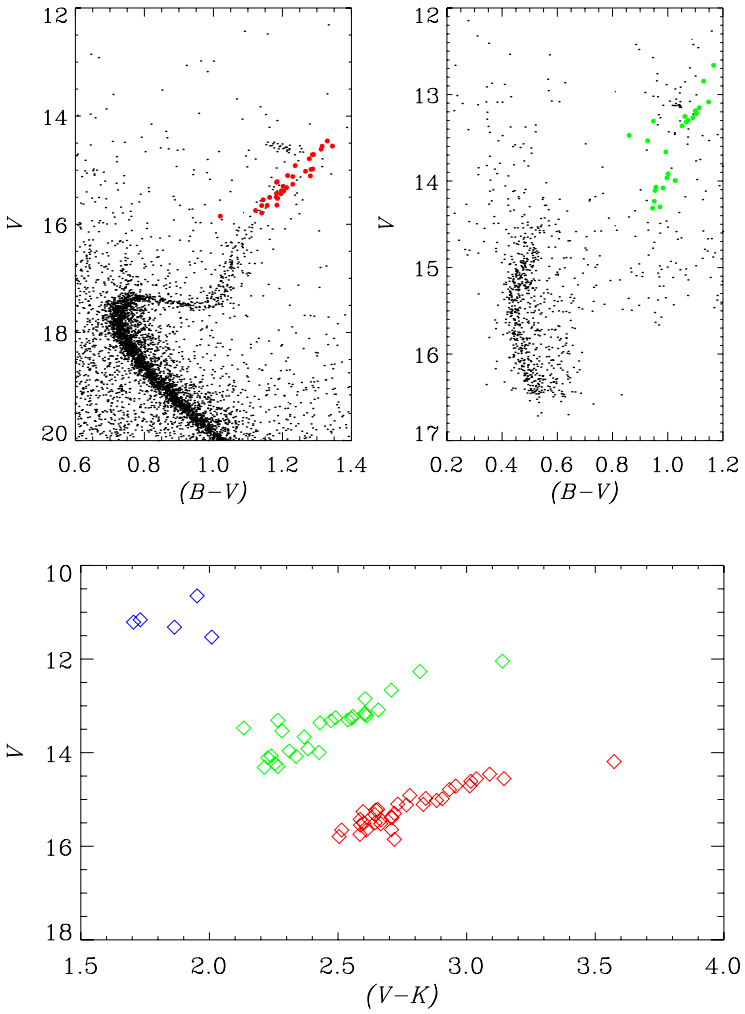

Figure 2.9: Color-magnitude diagrams in the three clusters (same color coding as in Figure 2.8). The $(B-V)$ and $(V-K)$ color is corrected from reddening. The upper two diagrams show all the cluster members (black dots) in NGC 6791 (Stetson et al., 2003) and NGC 6819 (Hole et al., 2009) and targets in our study (coloured dots). The lower shows the V magnitude against $(V-K)$ color for all the three clusters. The clusters are located differently in the diagram into three groups, indicating deviations in global parameters, such as mass.

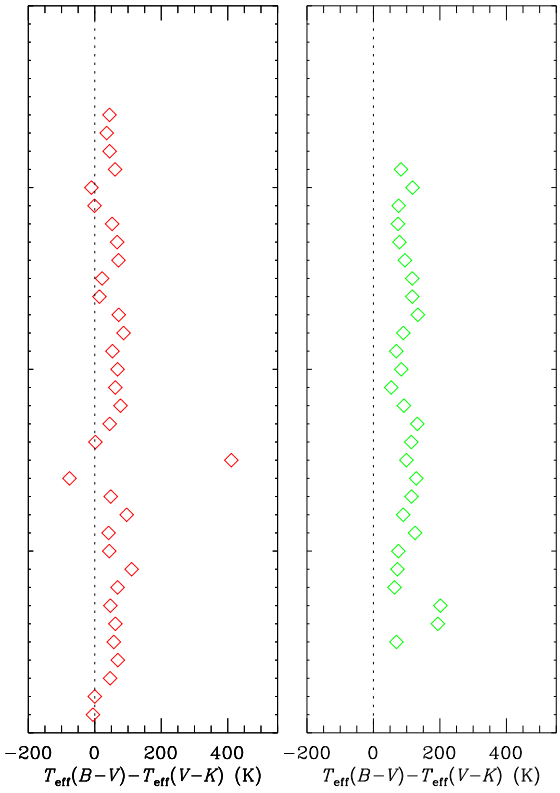

Figure 2.10: Difference between temperatures derived from the $(V-K)$ and $(B-V)$ color indices for NGC 6791 (left) and NGC 6819 (right). The vertical dashed lines locate the position of 0. The y-axis is the KIC number ascending with the same order as given in Table 2.2 and 2.3.

2.3.3 Estimates of Luminosity

Luminosity measures the total amount of energy that a star emits per unit time. Normally it is related to the brightness that is the luminosity observed in a certain spectral region. If we plot the luminosity as a function of the surface effective temperature of our cluster targets in the Hertzsprung–Russell diagram, we can have basic idea of their evolutionary stages. As a matter a fact, the color-magnitude diagrams shown in Figure 2.9 is also a version of Hertzsprung–Russell diagram, because the V band photometry is the apparent magnitude, also called visual magnitude, which is a measure of the stellar brightness as observed by the telescope and is related to the luminosity and the color indices can directly lead to effective temperature. Additionally, luminosity is an important parameter in

modelling.

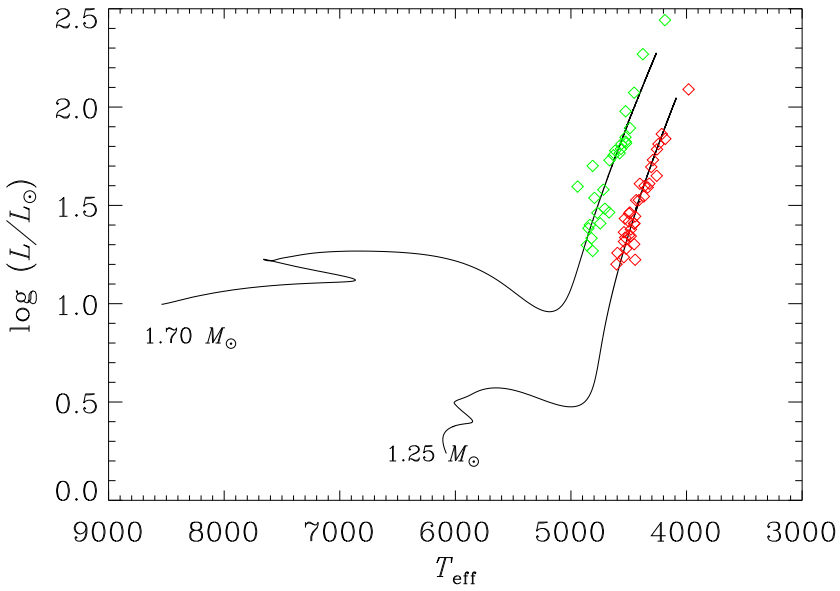

Figure 2.11: Evolutionary tracks of two models for the targets in NGC 6791 (red diamonds) and NGC 6819 (green diamonds). The initial masses of the models are 1.25 and 1.70 $M_\odot$. It is clear that all our targets are on the ascending giant branch. Detailed modelling is still needed to determine the masses.

Assuming a star is a black body, the luminosity of a star L is given by:

$$L = 4\pi R^2 \sigma T_{\rm eff}^4 \tag{2.12}$$

where σ is the Stefan–Boltzmann constant $5.67 \times 10^{-8}\mathrm{Wm}^{-2}\mathrm{K}^{-4}$ and R is the stellar radius which is not a measurable parameter from photometry, but through a somewhat lengthy calculation it is attainable, which involves the stellar distance and absolute magnitude. Instead of calculating the radius for our targets, we obtain their luminosities. The luminosity ratio to the Sun is related to the difference in bolometric magnitude as:

$$\log\left(\frac{L}{L_\odot}\right) = \frac{M_{\rm bol,\star} - M_{\rm bol,\odot}}{-2.5}\ , \tag{2.13}$$

where $L_\odot$ is the luminosity of the Sun, $M_{\rm bol,\odot}$ and $M_{\rm bol,\star}$ are the bolometric magnitudes of the star and the Sun, respectively. The bolometric magnitude of

the star can be corrected from its absolute visual magnitude:

$$M_{\mathrm{bol},\star} = M_V + \mathrm{BC} \,, \tag{2.14}$$

here BC is a bolometric correction, M_V is the V band absolute magnitude. The BC depends on the stellar temperature. We derived the BCs using the calibrations of Flower (1996), who introduced BC–temperature relations. The BCs of our targets are listed in Table 2.2, 2.3 and 2.4 for the three clusters. The other term on the right side of equation 2.14 M_V can be obtained from the observable apparent visual magnitude V with

$$M_V = V - \mu \,, \tag{2.15}$$

with μ being the visual distance modulus, always denoted as $\mu = (m - M)_V$. Similar to the color indices, the interstellar medium absorption is also an important factor to the distance modulus and it can even play a dominant role in some special cases, *e.g.* in the direction of the galactic centre. Hence a reddening correction can be performed to the visual distance modulus which then become the true distance modulus denoted as $\mu_0 = (m - M)_0$. We adopted the distance moduli for NGC 6791 and NGC 6819 from Basu et al. (2011), and that for NGC 6811 from Barkhatova et al. (1978). The difference between the visual and true distance modulus is the interstellar extinction $A(V)$,

$$\begin{aligned}(m - M)_0 &= V_0 - M_V = V - A(V) - M_V \\ &= (m - M)_V - A(V) \,.\end{aligned} \tag{2.16}$$

The extinction $A(V)$ is actually the difference between the apparent and true magnitudes of V band and is related to the reddening correction, given by

$$A(V) = V - V_0 = 2.5E(B - V) \,, \tag{2.17}$$

where the coefficient 2.5 is the reddening constant $R(V) = A(V)/E(B - V)$. It is straightforward to derive the luminosity from equations (2.13), (2.14), (2.16) and (2.17):

$$\begin{aligned}\log\left(\frac{L}{L_\odot}\right) =& 0.4(M_{\mathrm{bol},\odot} - V + 2.5E(B - V) \\ &+ (m - M)_0 - BC) \,,\end{aligned} \tag{2.18}$$

with $M_{\mathrm{bol},\odot}$ adopted as 4.7554 mag. The luminosities of all our cluster targets are also given in Table 2.2, 2.3 and 2.4. For the uncertainties of luminosity, we considered the same contributions from V (0.02), $E(B - V)$ (0.02) as for the temperature, and also those from $(m - M)_0$ (0.06) and BC (0.01). As a result, we adopted a conservative uncertainty of 0.01 for all the luminosities. So far we have obtained the two parameters T_{eff} and L, we can plot the targets in the Hertzsprung–Russell diagram of Figure 2.11, in which we also plot two evolutionary tracks of the models simulated by the ASTEC evolution code

(Christensen-Dalsgaard, 2008a) to guide the eye. The models are initiated from the parameters in Basu et al. (2011). They are not for detailed modelling, but only to give the basic idea of how the two clusters evolve.

2.3.4 Verification of Memberships

Although targets in the same cluster share some global parameters, such as distance, metallicity and age, they don't necessarily have an identical mass. In fact, members of a cluster have large differences in mass, which decide the speed of their evolution. Under the condition that they have same initial composition, members with larger masses evolve faster than those with smaller masses, and consequently members at the same evolution stage are supposed to have relatively similar masses. Combining the asymptotic scaling relations given by equations (1.12) and (1.13) with luminosity equation (2.12) yields

$$\frac{\nu_{\rm max}}{\nu_{\rm max,\odot}} \simeq \left(\frac{M}{M_\odot}\right)\left(\frac{T_{\rm eff}}{T_{\rm eff,\odot}}\right)^{3.5}\left(\frac{L}{L_\odot}\right)^{-1} , \tag{2.19}$$

$$\frac{\Delta\nu}{\Delta\nu_\odot} \simeq \left(\frac{M}{M_\odot}\right)^{0.5}\left(\frac{T_{\rm eff}}{T_{\rm eff,\odot}}\right)^{3}\left(\frac{L}{L_\odot}\right)^{-\frac{3}{4}} , \tag{2.20}$$

which scale the $\nu_{\rm max}$ and $\Delta\nu$ from luminosity instead of radius. The two variables in equations (2.19) and (2.20) $T_{\rm eff}$ and L are already obtained, and for the mass we again adopted the ones from Basu et al. (2011) for NGC 6791 and NGC 6819. For NGC 6811 we used the value of 2.6 $M_\odot$ as the average mass (Hekker et al., 2011). Therefore $\nu_{\rm max}$ and $\Delta\nu$ can be estimated using the scaling relations, and they are expected in the same cluster and are expected to have similar masses. The results from the scaling relations $\nu_{\rm max,sc}$ and $\Delta\nu_{\rm sc}$ are listed in Table 2.2, 2.3 and 2.4 for the three clusters, respectively. The observed–to–scaled ratios for $\nu_{\rm max}$ and $\Delta\nu$ are shown in Figure 2.12. Almost all the targets locate within the $1-\sigma$, which means the masses we used in the scaling relations are correct and all the targets are members of their cluster. This method was used by Stello et al. (2011) to distinguish the membership for NGC 6791, NGC 6819 and NGC 6811. They studied almost one year data of *Kepler* data and confirmed four previously found non-members in NGC 6819 and three additional non-members are found, two in NGC 6819, one in NGC 6791. The scaling relations are proved to be a very robust method to study the membership of clusters directly using seismic properties. Here in this thesis, we have data that span 4 times longer than that in the work of Stello et al. (2011), which are therefore enable us to obtain accurate seismic parameters for these red giant targets in the three open clusters.

It should be noted that the temperature used for the scaled $\nu_{\rm max}$ and $\Delta\nu$ are

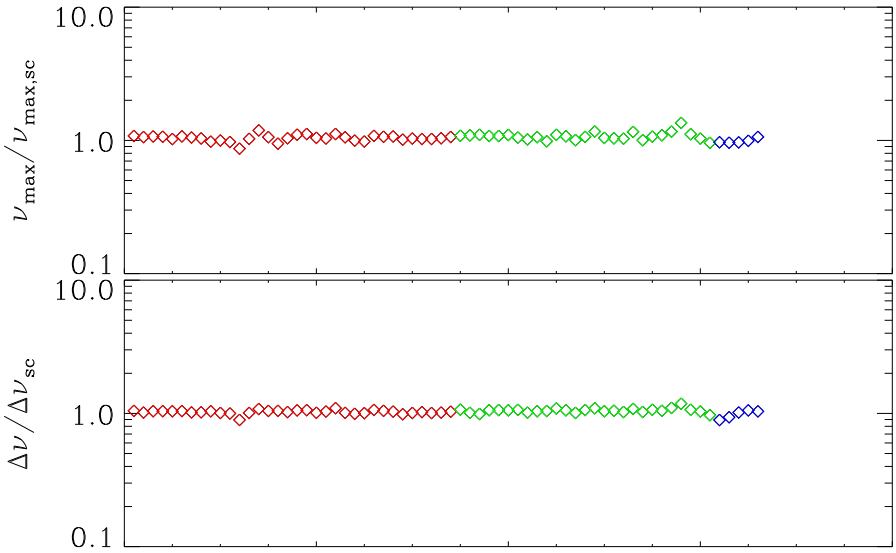

Figure 2.12: Ratio between observed and solar-scaled $\nu_{\rm max}$ (top) and $\Delta\nu$ (bottom) for targets in NGC 6791 (red), NGC 6819 (green) and NGC 6811 (blue). The x-axis is again the KIC number.

calibrated from $(V-K)$ color index. We also tested the results using $(B-V)$ colors. The scatter of is 1% larger for the ratio of $\nu_{\rm max}$ and 3% larger for the ratio of $\Delta\nu$ scaled from $(V-K)$ colors. These results verify that the utility of $(V-K)$ color to derive temperature for cool red giants is more reasonable than $(B-V)$.

Chapter 3

Modelling

In Chapter 2, we spend most of the pages introducing asteroseismology for RGBs from the observation point of view. In this chapter, we will discuss asteroseismology theoretically, specifically we will focus on the numeric modelling part. However, we will not dig into the codes to investigate how they numerically interpret various complicated physics, but to discuss the utilization of the codes from the consumer's point of view. The codes here we are using refer to evolutionary codes that can simulate the evolution track of the star, and oscillation codes that can compute oscillation frequencies and eigenfunctions for models generated by evolutionary codes. For the former one, we generally use the Aarhus STellar Evolution Code (ASTEC, Christensen-Dalsgaard, 2008a) and for the latter one we use the Aarhus Adiabatic Oscillation Package (ADIPLS, Christensen-Dalsgaard, 2008b).

In the first part of this chapter, we will introduce the general problems of modelling in asteroseismology and in the remaining parts we will show several examples of our modelling work.

3.1 Modelling stars in Asteroseismology

At the beginning of this thesis, we show a simple H–R diagram, Figure 1.1, simulating the solar evolutionary track computed by ASTEC. With correct initial input parameters, the track is able to provide information on models at certain stage for a given star, in this case our Sun. Different evolution codes require different parameters. In ASTEC, the simplest set of initial inputs is mass and composition to start an evolutionary computation. It is also possible to control the mixing length, diffusion, overshoot and the kind of some complicated

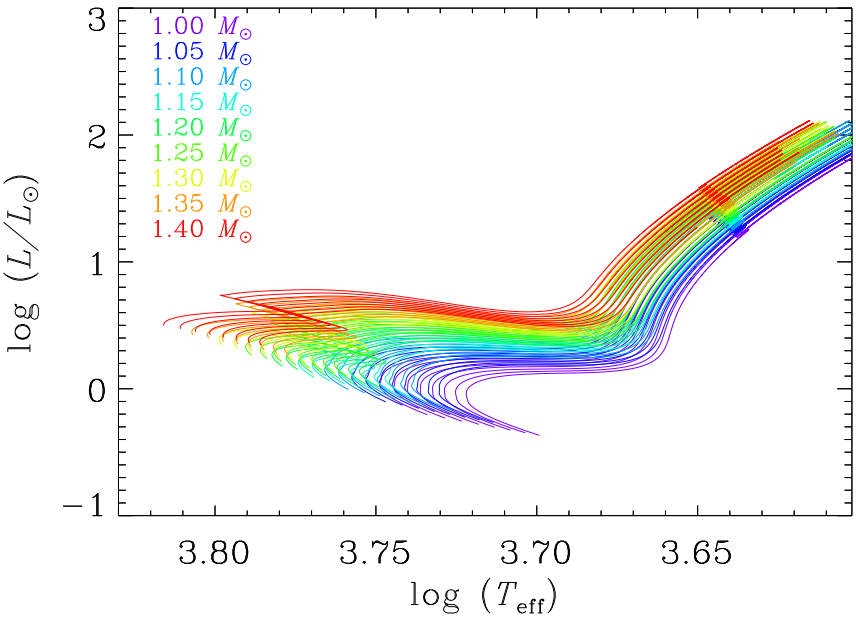

Figure 3.1: Evolutionary tracks for models with different masses (M = 1.00 to $1.40 M_\odot$ and Z = 0.025 to 0.040. Models with the same masses are in the same color. There is no distinguishment in color nor line style among models with different Z, but in principle models with larger value of Z have smaller temperatures and luminosities and hence lies to the right of ones with smaller Z.

physics. However, there are many aspects of physics that so far we do not understand. Therefore we have to make some simplifications in the modelling. Aerts et al. (2010) summarize the approximations made in most stelar evolution calculations. Here we simply cite their summarizations adopted in ASTEC:

1. The convection is generally approximated and parametrized through the mixing-length theory.
2. Effects of rotation are ignored.
3. Effects of magnetic fields are ignored.
4. Effects of stellar winds are ignored.

For the calculations of oscillation frequencies, the assumption of adiabatic oscillation is always used, which assumes the oscillating elements do not transfer

heat or matter between itself and its surroundings and the motion occurs adiabatically. Since the star can be seen as a giant gas ball and we are talking about heat transfer or energy transfer at this point, we shall pay some special attention on the energy equation of hydrodynamic:

$$\frac{\mathrm{d}q}{\mathrm{d}t} = \frac{\mathrm{d}E}{\mathrm{d}t} + p\frac{\mathrm{d}V}{\mathrm{d}t} \,, \tag{3.1}$$

where $\mathrm{d}q/\mathrm{d}t$ is the rate of heat gain or loss, E the internal energy, per unit mass and $V = 1/\rho$ is specific volume. Equation (3.1) can be expressed in terms of thermodynamical coefficients:

$$\begin{aligned}\frac{\mathrm{d}q}{\mathrm{d}t} &= \frac{1}{\rho(\Gamma_3 - 1)}\left(\frac{\mathrm{d}p}{\mathrm{d}t} - \frac{\Gamma_1 p}{\rho}\frac{\mathrm{d}\rho}{\mathrm{d}t}\right) \\ &= c_p\left(\frac{\mathrm{d}T}{\mathrm{d}t} - \frac{\Gamma_2 - 1}{\Gamma_2}\frac{T}{p}\frac{\mathrm{d}p}{\mathrm{d}t}\right) \\ &= c_V\left[\frac{\mathrm{d}T}{\mathrm{d}t} - (\Gamma_3 - 1)\frac{T}{\rho}\frac{\mathrm{d}\rho}{\mathrm{d}t}\right] \,. \end{aligned} \tag{3.2}$$

When the assumption of adiabatic is considered, the heating can be neglected, therefore from the energy equation given above

$$\frac{\mathrm{d}p}{\mathrm{d}t} = \frac{\Gamma_1 p}{\rho}\frac{\mathrm{d}\rho}{\mathrm{d}t} \,. \tag{3.3}$$

This equation, together with the continuity equation

$$\frac{\partial \rho}{\partial t} + \mathrm{div}(\rho \boldsymbol{v}) = 0, \tag{3.4}$$

where $\boldsymbol{v}(\boldsymbol{r}, t)$ is the velocity of the moving element, and equation of motion

$$\rho\frac{\partial \boldsymbol{v}}{\partial t} + \rho\boldsymbol{v}\cdot\nabla\boldsymbol{v} = -\nabla p + \rho\boldsymbol{f} \,, \tag{3.5}$$

where $\boldsymbol{f}$ is the body force per unit mass which needs to be specified in a given situation, and the Poissen equation

$$\nabla^2 \Phi = 4\pi G\rho \,, \tag{3.6}$$

form the complete set of equations for adiabatic oscillations. We consider only gravity that is among all the possible body forces. The force per unit mass from gravity is the gravitational acceleration $\boldsymbol{g}$, which is the gradient of the gravitational potential Φ as

$$\boldsymbol{g} = -\nabla\Phi. \tag{3.7}$$

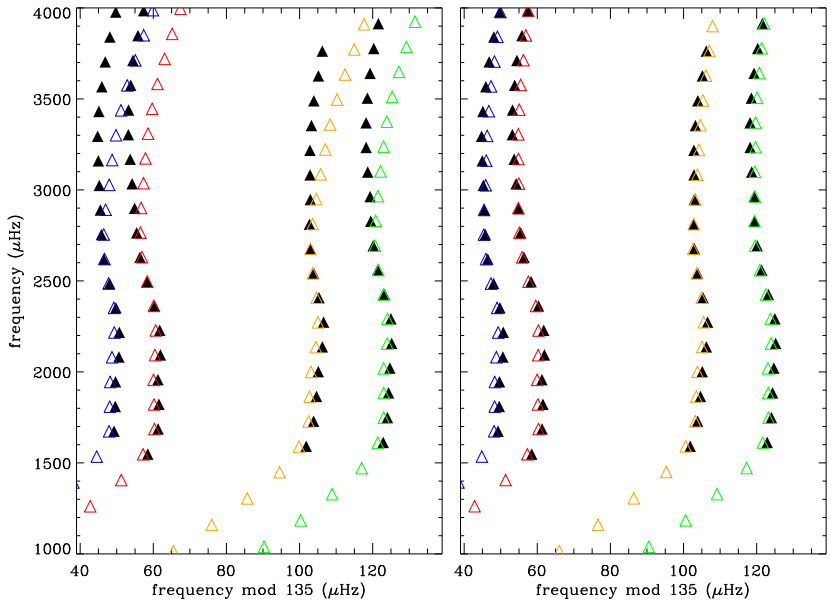

Figure 3.2: Échelle diagrams of observed (filled triangles) and computed (open triangles) frequencies for the Sun. The left plot shows the offsets between observed and computed frequencies, while the right one shows the theoretical frequencies after surface corrections. Four degrees of modes are presented in the plots with radial models in red, $l = 1, 2$ and 3 mode in blue, green and orange, respectively. The observed solar frequencies are from BiSON.

Some oscillation codes also take non-adiabatic effects into account, but their treatment is not clear yet. Furthermore, most of the uncertain or neglected microphysics are concentrated very near the surface (Aerts et al., 2010). Such near-surface can be very problematic to the evolutionary codes as well as to the oscillation frequencies.

As mentioned above, mass and metallicity are two important inputs to the evolutionary codes. In most astronomical objects, hydrogen and helium are the dominant elements. The metallicity can be expressed by the hydrogen mass fraction $X = m_H/M$, helium mass fraction $Y = m_{He}/M$ and the mass fraction of all the elements heavier than helium $Z = \sum m_i/M = 1 - X - Y(i > He)$ where M is the total mass of the system and m_i is the mass of the element it contains. ASTEC accepts X and Z as the input of metallicity because Y is very easy to obtain from them. Figure 3.1 shows a bunch of models with different masses (from 1.00 to 1.40 $M_\odot$) and different Z values (from 0.025 to 0.040). Their X and mixing length parameter α are fixed as 0.70 and 1.80, respectively. For models with higher masses, their tracks have higher temperatures and luminosities than those models with

Table 3.1: Near-surface corrections for the solar model

l	n_i	$\langle\nu_{\rm obs}(n)\rangle$ (μHz)	$\langle\nu_{\rm ref}(n)\rangle$ (μHz)	$\langle\Delta\nu_{\rm obs}(n)\rangle$ (μHz)	$\langle\Delta\nu_{\rm ref}(n)\rangle$ (μHz)	a (μHz)	r
0	10–28	2765.89	2768.53	134.98	135.67	-3.08	1.00011
1	10–27	2762.29	2764.72	135.07	135.78	-3.40	1.00024
2	10–27	2823.94	2826.49	135.22	135.96	-3.32	1.00027
3	10–25	2677.36	2678.86	135.43	136.11	-3.96	1.00057

lower masses. For models with same mass but different Z values, larger Z value models lie to the right of less metal-rich models, hence their temperatures and luminosities are smaller than the latter models at the same evolutionary point. The code is able to provide a large number of parameters of the model at every time step along the track. However, models with totally different inputs can occupy the same point in the H–R diagram. This is very clear in Figure 3.1 that many models overlap with other models of different color. In fact, the evolution track of a model can be very close, for some time at certain stage, to that of a model with higher masses and higher Z. Furthermore, X and α can also change the evolution tracks of the models. We do not discuss in detail how they will change the tracks, but to get the best model that fits a real star we need the correct set of inputs.

3.1.1 Selecting the Best-fitting model

So how to find the best fit models among all these models initiated from various sets of inputs? We can make use of the observations to fulfill this goal. There are two approaches could be used for the modelling in asteroseismology. The first one is the so-called *grid-based* method, which uses models generated by a wide range of masses and metallicities and perhaps mixing-length parameter and search for the best model that fits the observational constraints, such as $\nu_{\rm max}$, $\Delta\nu$ $T_{\rm eff}$ and [Fe/H] (Stello et al. 2009b; Basu et al. 2010; Gai et al. 2011; Chaplin et al. 2014). The other approach is *detailed frequency modelling*, which uses individual oscillation frequencies extracted from the observed power spectrum instead of the global seismic parameters to determine the best-fitting model more precisely (Metcalfe et al., 2010; Jiang et al., 2011). In this thesis, we use the detailed frequency modelling approach to look for best-fitting model for our targets, but we also use the global parameters as preliminary constraints.

In this section we continue using our Sun, the best observed star of all time, as an example to explain how to perform the asteroseismic modelling. First, we should calculate some models that cover a wide range of masses and metallicities. Since we observed the Sun so well that we know its radius ($R_\odot = 6.95508 \times 10^8$ cm), luminosity ($L_\odot = 3.846 \times 10^3 3$ erg/s) , effective temperature ($T_{\rm eff} = 5777$ K), age (4.57 Gyr), $Z/X = 0.0245$ (Grevesse & Noels, 1993), it is possible for us to calibrate the solar model based on these solar parameters after several iterations. The model plotted in Figure 1.1 is actually a calibrated solar model track with initial $X = 0.718$, $Z = 0.0176$ and $\alpha = 1.93$, which hit the solar parameters at the age of 4.57 Gyr. For stars other than the Sun, we do not have so many observational constraints that we may only two or three parameters, normally $T_{\rm eff}$, [Fe/H], photometry and seismic ones $\nu_{\rm max}$ and $\Delta\nu$,

which can be used for the model selection. Then we could perform a χ^2 minimization to find the best models. The definition of the χ^2 function was based on observed stellar parameters, $P_i^{\rm obs}$, as follows:

$$\chi^2 = \frac{1}{N}\sum_{i=1}^{N}\left(\frac{P_i^{\rm obs} - P_i}{\sigma_i}\right)^2 , \tag{3.8}$$

where N is the number of observed variables, P_i is model parameters, and σ_i is the estimated uncertainty for each $P_i^{\rm obs}$. Models with χ^2 less than a certain threshold are selected for frequency comparison.

3.1.2 Near-surface correction

Then we can go on to compute oscillation frequencies for this particular model at this particular age and compare them with observed frequencies. The theoretical frequencies are computed using the ADIPLS code, and the observed frequencies are from Birmingham Solar Oscillation Network (BiSON, Chaplin et al., 1996). However, it has been established by several studies Christensen-Dalsgaard et al. 1988; Dziembowski et al. 1988; Christensen-Dalsgaard et al. 1996; Christensen-Dalsgaard & Thompson 1997 that there is a long-lasting systematic deviation between the theoretical and observed frequencies due to the deficient treatment of near-surface layers in the modelling codes. Kjeldsen et al. (2008) derived an empirical correction for the near-surface effect, which we will use in the following pages. For the Sun, the offset between the computed frequencies of the best model $\nu_{\rm best}$ and the observed ones $\nu_{\rm obs}$ can be well fitted by a power law given by

$$\nu_{\rm obs}(n) - \nu_{\rm best}(n) = a\left[\frac{\nu_{\rm obs}}{\nu_0}\right]^b , \tag{3.9}$$

where n is the radial order, and ν_0 is a suitably chosen reference which is usually chosen to be the $\nu_{\rm max}$. Although the best model here is thought to be the one describing the stellar interior, it still fails to model the near-surface layers. That is also why the offsets exist in equation (3.9) for the "best model". Practically, we may have some candidates for the best models, which are very close to the best models and are called the reference model. The frequencies of the reference model, $\nu_{\rm ref}$, are also very close to those of the best model and from homology they can be scaled from $\nu_{\rm best}$ like this

$$\nu_{\rm best} = r\nu_{\rm ref}(n) , \tag{3.10}$$

where r is the scaling factor. A reference model close to the best model gives a value of r close to 1. Substituting equation (3.10) into equation (3.9) results

$$\nu_{\rm obs}(n) - r\nu_{\rm ref}(n) = a\left[\frac{\nu_{\rm obs}}{\nu_0}\right]^b . \tag{3.11}$$

In order to obtain the factor r, we can differentiate equation (3.11) with respect to n, which gives

$$\Delta\nu_{\rm obs}(n) - r\Delta\nu_{\rm ref}(n) = ab\left[\frac{\nu_{\rm obs}(n)}{\nu_0}\right]^{b-1}\frac{\Delta\nu_{\rm obs}(n)}{\nu_0} . \tag{3.12}$$

Rearranging last two equations then r is directly given by

$$r = (b-1)\left[b\frac{\langle\nu_{\rm ref}(n)\rangle}{\langle\nu_{\rm obs}(n)\rangle} - \frac{\langle\Delta\nu_{\rm ref}(n)\rangle}{\langle\Delta\nu_{\rm obs}(n)\rangle}\right]^{-1} , \tag{3.13}$$

and

$$b = \left[r\frac{\langle\Delta\nu_{\rm ref}(n)\rangle}{\langle\Delta\nu_{\rm obs}(n)\rangle} - 1\right]\left[r\frac{\langle\nu_{\rm ref}(n)\rangle}{\langle\nu_{\rm obs}(n)\rangle} - 1\right]^{-1} . \tag{3.14}$$

where $\langle\nu_{\rm ref}(n)\rangle$ and $\langle\nu_{\rm obs}(n)\rangle$ are the means of the given sets of frequencies with radial orders $n_1, n_2, ..., n_N$, and

$$\langle\Delta\nu_{\rm obs}(n)\rangle = \frac{\sum_{i=1}^{N}\left[\nu_{\rm obs}(n_i) - \langle\nu_{\rm obs}(n)\rangle\right](n_i - \langle n\rangle)}{\sum_{i=1}^{N}(n_i - \langle n\rangle)^2} , \tag{3.15}$$

$$\langle\Delta\nu_{\rm ref}(n)\rangle = \frac{\sum_{i=1}^{N}\left[\nu_{\rm ref}(n_i) - \langle\nu_{\rm ref}(n)\rangle\right](n_i - \langle n\rangle)}{\sum_{i=1}^{N}(n_i - \langle n\rangle)^2} , \tag{3.16}$$

Lastly, by assuming a value for either b or r and estimate the other using equation (3.13) or (3.14), the value of a is given as

$$a = \frac{\langle\Delta\nu_{\rm obs}(n)\rangle - r\langle\Delta\nu_{\rm ref}(n)\rangle}{N^{-1}\sum_{i=1}^{N}\left[\nu_{\rm obs}(n_i)/\nu_0\right]^b} . \tag{3.17}$$

Kjeldsen et al. (2008) found $b = 4.90$ using the solar data measured by Lazrek et al. (1997) and solar model S of Christensen-Dalsgaard et al. (1996). It is possible to estimate r and a from equations (3.13) and (3.17) with the given b. Following these steps, we corrected the computed frequencies of our solar model (model 'MS' in Figure 1.1) and show the results in Figure 3.2. The offsets between observed and computed frequencies are obvious in the left panel in which $l = 0, 1, 2,$ and 3 modes are plotted. We corrected the near-surface effect for all the theoretical p modes and using $b = 4.9$ to determine r and a for each degree. From the resulted parameters listed in Table 3.1 we can see that the offsets are nearly independent of degree l, for the values of r for each degree modes are very close. From the échelle diagram with the uncorrected theoretical frequencies we can also see that the offsets affect the highest frequencies the most.

The offsets between observed and computed mixed modes frequencies become

$$\nu_{\rm obs}(n) - rQ_{nl}\nu_{\rm ref}(n) = a\left[\frac{\nu_{\rm ref}(n)}{\nu_0}\right]^b , \tag{3.18}$$

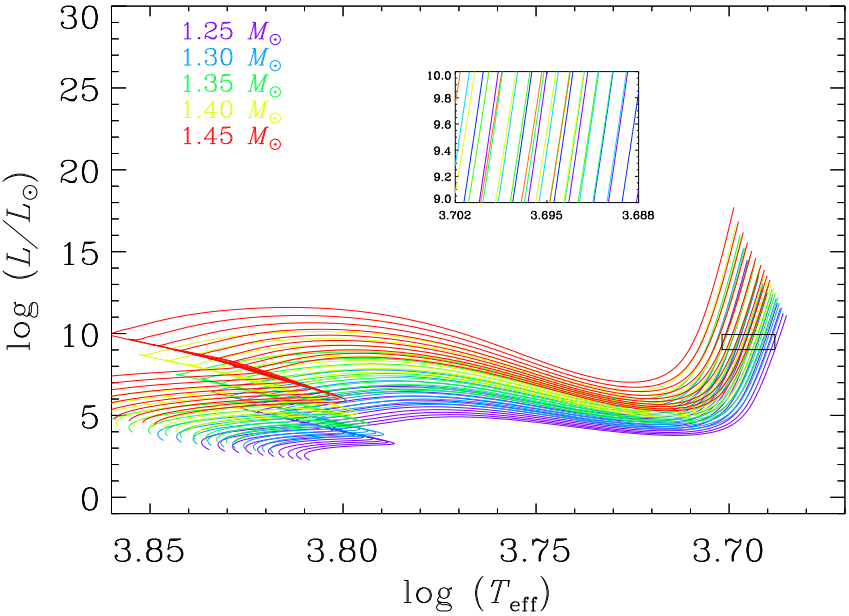

Figure 3.3: Evolution tracks for the grid of models built for KOI-1299. Models with same mass are in the same color. The error box is based on observed $T_{\rm eff}$ and derived L listed in Table 3.2. The inset plot is a blown up version of the error box. Not all the models are plotted in the figure.

and

$$Q_{nl} = \frac{E_{nl}}{\overline{E}_0(\omega_{nl})} \,, \tag{3.19}$$

where E_{nl} is the mode inertia (*cf.* equation (1.3) and $\overline{E}_0(\omega_{nl})$ is obtained by interpolating to ω in the values of inertia for radial modes. In principle, Q_{nl} is much larger than 1, which means that the surface correction applied to mixed modes should be less than that for the pure p modes.

We use the method described by Brandão et al. (2011) to find the best-fitting model with the near-surface corrected frequencies. A χ^2 minimization is also performed to find the reference model that have individual oscillation frequencies closest to the observed ones for all l and it is given by

$$\chi^2 = \frac{1}{N} \sum_{n,l} \left[\frac{\nu_{\rm ref,corr}(n,l) - \nu_{\rm obs}(n,l}{\sigma(\nu_{\rm obs}(n,l))} \right]^2 \,, \tag{3.20}$$

where N is the number of modes, $\nu_{\rm ref,corr}(n,l)$ are the surface-corrected frequencies of modes of a given reference model, and $\sigma(\nu_{\rm obs}(n,l))$ are the estimated errors for the observed frequencies. It should be noted that the correction term in the right-hand side of equation (3.9) only works for the frequencies of the best model. Since we do not

Table 3.2: KOI-1299 observation properties

Parameter	Value
Spectroscopic Properties	
$T_{\rm eff}$ (K)	4995 ± 78
$\log g$ (cgs)	3.340 ± 0.006
[m/H]	-0.07 ± 0.10
$v \sin i$ (km s^{-1})	2.7 ± 0.5
Photometric Properties	
V (mag)	12.463 ± 0.050
K_p (mag)	12.183 ± 0.020
J (mag)	10.684 ± 0.021
H (mag)	10.221 ± 0.019
K_s (mag)	10.121 ± 0.017
Asteroseismic Properties	
$\nu_{\rm max}$	266 ± 3
$\Delta\nu$	18.59 ± 0.04
Derived Properties	
$M(M_\odot)$	$1.35^{+0.10}_{-0.07}$
$R(R_\odot)$	$4.12^{+0.12}_{-0.08}$
$L(L_\odot)$	9.48 ± 0.46
ρ (g cm^{-3})	0.02725
Age (Gyr)	$3.5^{+0.7}_{-0.8}$
$E(B-V)$ (mag)	0.039 ± 0.004
d (pc)	879 ± 20

have the best model yet but only have some reference models that are close to the best model, we can again scale the corrected frequencies of the reference model $\nu_{\rm ref,corr}(n,l)$ from the corrected ones of the best model $\nu_{\rm best,corr}(n,l)$, to a good approximation, as

$$\nu_{\rm best,corr}(n,l) = r\nu_{\rm ref,corr}(n,l) \ , \tag{3.21}$$

substituting which into equation (3.9), and with the approximation $\nu_{\rm best,corr} \approx \nu_{\rm obs}$, hence we have

$$\nu_{\rm ref,corr}(n,l) = \nu_{\rm ref}(n,l) + \left(\frac{a}{r}\right)\left[\frac{\nu_{\rm obs}(n,l)}{\nu_0}\right]^b \ . \tag{3.22}$$

Thus, equation (3.20) becomes

$$\chi^2 = \frac{1}{N}\sum_{n,l}\left(\frac{\nu_{\rm ref}(n,l) + \left(\frac{a}{r}\right)\left[\frac{\nu_{\rm obs}(n,l)}{\nu_0}\right]^b - \nu_{\rm obs}(n,l)}{\sigma(\nu_{\rm obs}(n,l))}\right)^2 \ , \tag{3.23}$$

which is appropriate for pure p modes correction. For mixed modes, we can make use

of the inertia ratio Q_{nl} in the χ^2 of equation (3.20) as

$$\chi^2 = \frac{1}{N}\sum_{n,l}\left(\frac{\nu_{\rm ref}(n,l) + \frac{1}{Q_{nl}}\left(\frac{a}{r}\right)\left[\frac{\nu_{\rm obs}(n,l)}{\nu_0}\right]^b - \nu_{\rm obs}(n,l)}{\sigma(\nu_{\rm obs}(n,l))}\right)^2 , \tag{3.24}$$

After the χ^2 minimization for all the reference models with corrected modes, the best model is the one that have least value of equation (3.20).

Table 3.3: KOI-1299 identified mode frequencies

n	$l=0$ (μHz)	$l=1$ (μHz)	$l=2$ (μHz)	$l=3$ (μHz)
9	$194.11^{0.018}_{-0.014}$	$202.500^{+0.007}_{-0.008}$	$209.990^{+0.010}_{-0.023}$	
		$204.392^{+0.015}_{-0.010}$		
		$207.713^{+0.006}_{-0.007}$		
10	$212.214^{+0.025}_{-0.020}$	$215.394^{+0.008}_{-0.007}$	$228.236^{+0.019}_{-0.019}$	
		$219.215^{+0.006}_{-0.008}$		
		$221.586^{+0.011}_{-0.019}$		
		$224.590^{+0.016}_{-0.008}$		
		$228.905^{+0.020}_{-0.013}$		
11	$230.704^{+0.009}_{-0.008}$	$233.410^{+0.013}_{-0.017}$	$247.031^{+0.013}_{-0.016}$	$253.534^{+0.018}_{-0.034}$
		$233.410^{+0.013}_{-0.017}$		
		$237.904^{+0.014}_{-0.011}$		
		$240.439^{+0.011}_{-0.009}$		
		$244.157^{+0.015}_{-0.009}$		
12	$249.259^{+0.016}_{-0.009}$	$254.553^{+0.005}_{-0.006}$	$265.636^{+0.011}_{-0.043}$	$272.212^{+0.015}_{-0.006}$
		$254.553^{+0.005}_{-0.006}$		
		$258.288^{+0.006}_{-0.008}$		
		$261.490^{+0.003}_{-0.004}$		
13	$267.757^{+0.017}_{-0.016}$	$273.216^{+0.007}_{-0.007}$	$284.389^{+0.013}_{-0.011}$	$291.410^{+0.009}_{-0.008}$
		$277.110^{+0.006}_{-0.008}$		
		$281.091^{+0.006}_{-0.006}$		
14	$286.457^{+0.006}_{-0.009}$	$294.131^{+0.015}_{-0.014}$	$303.352^{+0.021}_{-0.015}$	
		$297.229^{+0.013}_{-0.017}$		
15	$305.284^{+0.015}_{-0.014}$	$315.134^{+0.032}_{-0.011}$		

3.2 Global Parameter Constraints of KOI-1299

Using the approach mentioned in last section for asteroseismic modelling, we introduce our work on seeking the best model for a red giant star KOI-1299 in this section. The photometric observations of KOI-1299 were performed by *Kepler* which provided data that span *Kepler* observation quarter 0–7 (about 19 months). After being identified as a promising asteroseismic target, KOI-1299 was observed in short cadence mode ($\delta t \sim 58.89$ s) for 8 quarters. Its candidature of planetary system was raised by Kepler

Objects of Interest (KOI) and confirmed by Batalha et al. (2013). Quinn et al. (2014) highlight the discovery of KOI-1299b and c and studied the star and its planetary system in detail. We provide asteroseismic modelling result for that paper.

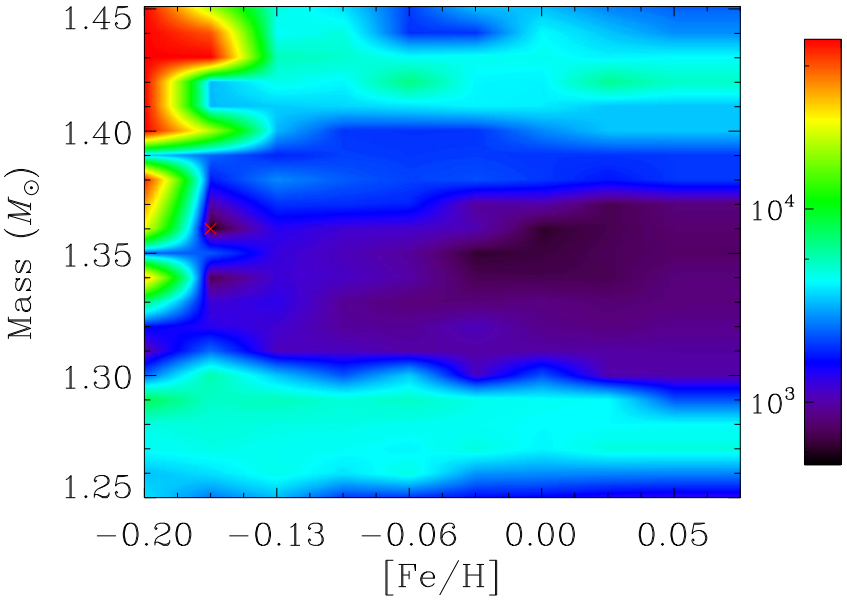

Figure 3.4: χ^2 calculated based on the surface corrected frequencies for all the models. The values of χ^2 are indicated by the color. The lower the χ^2 is, the black is more black. The x-axis is the metallicity of the models and y-axis is the mass. The red cross indicates the location of the 'best fitting model'.

Table 3.4: KOI-1299 best-fitting model properties

Parameter	Value
$M(M_\odot)$	1.36
$R(R_\odot)$	4.10
$L(L_\odot)$	9.62
ρ (g cm^{-3})	0.02789
$T_{\rm eff}$ (K)	5028
$\log g$ (cgs)	3.347
[m/H]	-0.16
Age (Gyr)	2.97

The basic observation features are listed in Table 3.2 (Quinn et al., 2014). The spectroscopic properties in the table were obtained by (Quinn et al., 2014), who analyzed the spectrographs from the Tillinghast Reflector Echelle Spectrograph (TRES,

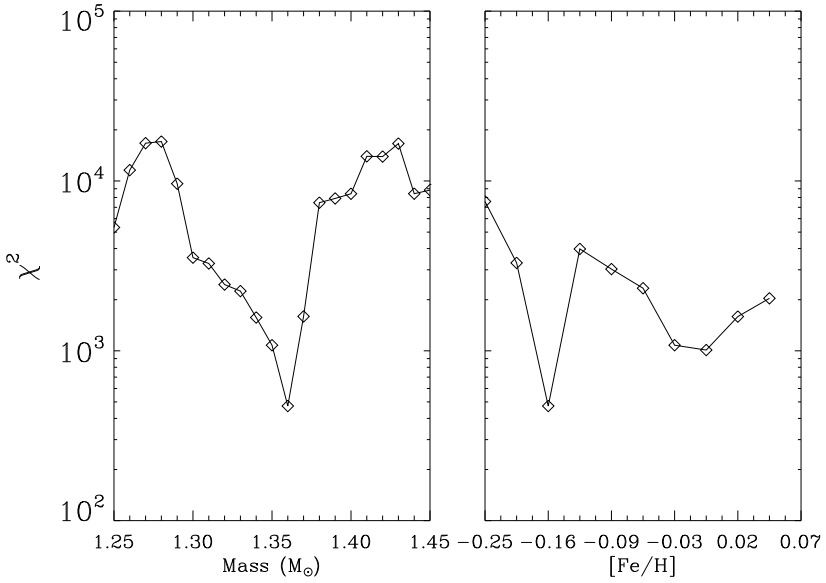

Figure 3.5: χ^2 plotted as functions of mass (left) and metallicity (right), respectively. The data points are obtained as the minima values from all the models with the same masses or metallicity.

Fűrész, 2008) mounted on the 1.5-m Tillinghast Reflector at the Fred L. Whipple Observatory (FLWO) on Mt. Hopkins, AZ and the FIber-fed Echelle Spectrograph (FIES, Frandsen & Lindberg, 1999) on the 2.5-m Nordic Optical Telescope (NOT, Djupvik & Andersen, 2010) at La Palma, Spain. For the photometric properties, K_p is the *Kepler* magnitude, J, H and K_s from the 2MASS catalog (Cutri et al., 2003). Quinn et al. (2014) used the eight quarters of short cadence *Kepler* data for the frequency analysis. The time series was prepared by the *Kepler Asteroseismic Science Operations Centre* (KASOC) filter (Handberg & Lund, 2014) using the *Kepler raw target pixel data* (Jenkins et al., 2010). The KASOC filter is able to remove long-term trends, instrument effects and transit signals, which can add unreal signals to the power spectra. They identified 37 modes and their frequencies are given in Table 3.3. We do not consider rotation in this thesis, so all the $l = 1$ mixed modes are $m = 0$ modes that are not affected by rotation.

We build a grid of models covering the parameters around the observed ones. We vary the masses and Z of the models to search for the best model, namely the masses are varied within the range of 1.25 to $1.45 M_\odot$ with a step of 0.01 $M_\odot$ and Z in the range of 0.01 to 0.02 with a step of 0.001. The Y is increased when Z increases according to the elation $\Delta Y/\Delta Z = 1.4$ (Casagrande et al., 2007), and hence the [Fe/H] of our models embrace the range of -0.25 to +0.07 (adopting $(X/Z)_\odot = 0.0245$). The mixing length parameter α is fixed to be 1.94, calibrated from the solar model The

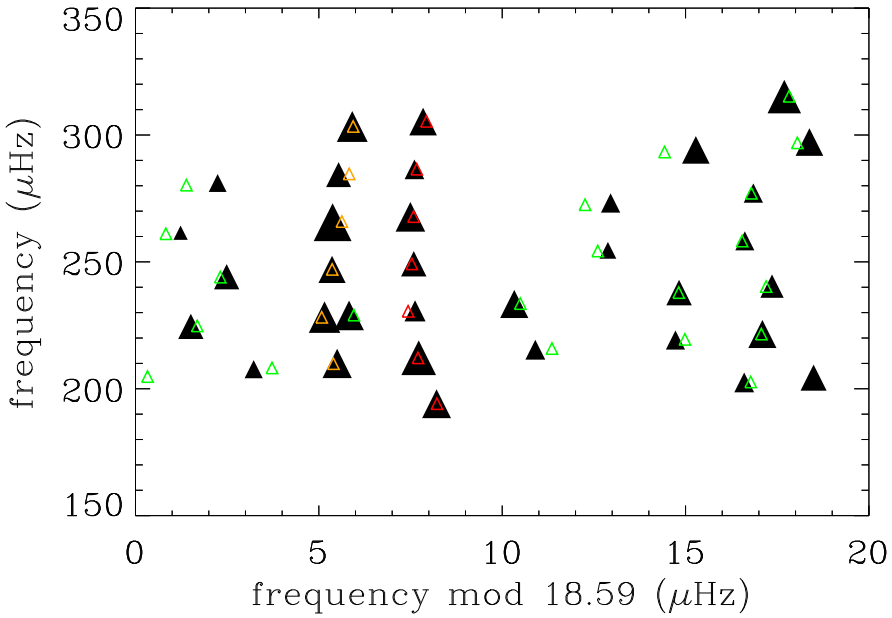

Figure 3.6: The échelle diagram of KOI-1299. The observed frequencies are filled triangles, whose sizes are scaled from their uncertainties. The computed frequencies are represented by open triangles, with radial modes in red, dipolar modes in green and quadrupole modes in orange.

evolution tracks of the grid are plotted in Figure 3.3. The black rectangle represents the error box for observed $T_{\rm eff}$ and $\log g$ from spectroscopy listed in Table 3.2. Tracks travel through the error box have chances to be the reference models. A zoomed in version of the error box is given as the inset plot. For the first step of model selection, we computed the χ^2 of equation (3.8), using observed parameters, $T_{\rm eff}$, L, R, $\log g$ and $\Delta\nu$, for all models locate in the error box. Then models with χ^2 smaller than 3 are selected for the next step.

By comparing the observed frequencies and computed frequencies for all the models selected through the first step, it is possible to find the best-fitting model more precisely. Thus, we continue to calculate χ^2 for the mode frequencies that are corrected from near-surface effect, using equation (3.23) for the radial modes and equation (3.24) for non-radial mixed modes. The results are given in Figure 3.4. Due to the fact that there are quite a few mixed dipolar modes observed for KOI-1299 and the uncertainties given by peakbagging processes are small, the resulted χ^2 values are mostly very large. In Figure 3.4 the blackish area, which covers the mass from 1.30 to 1.37 $M_{\odot}$, represents models with smaller χ^2.The smallest values of χ^2 are found in the order of several hundreds, but most models have χ^2 ranging from several thousands to tens of thousands. The best-fitting model locates at the leftmost edge of the blackish area, though the χ^2 of models with [Fe/H] of about -0.01 are only a little larger. This is clear

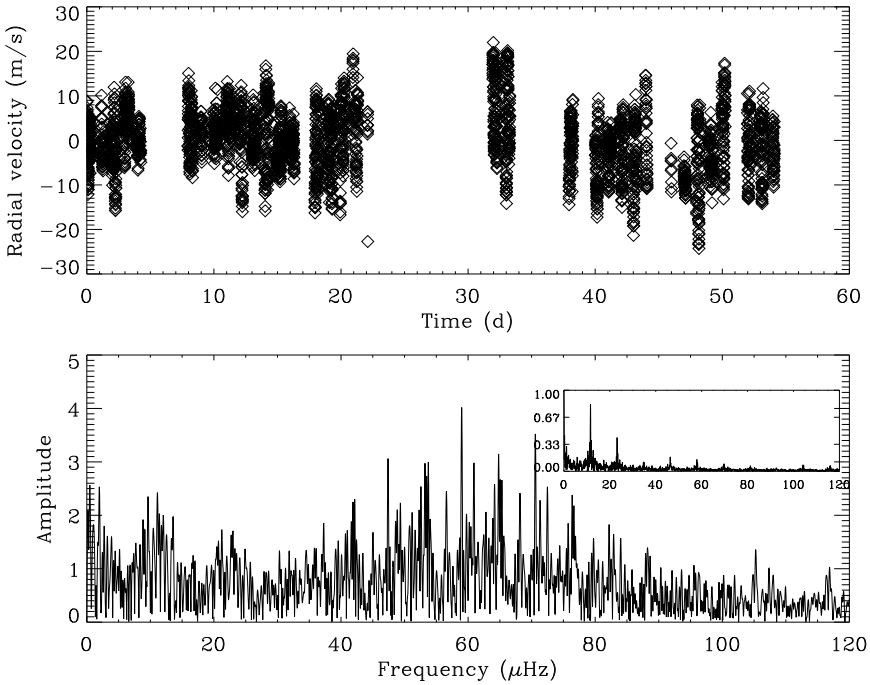

Figure 3.7: Upper panel, the time series of 46 LMi observed by SONG. Lower panel, power spectrum of 46 LMi transformed from the time series shown above. The inset plot shows the window function.

if we plot the χ^2 of models against the masses and [Fe/H] separately, as in Figure 3.5 and the best-fitting model was found to have mass of 1.36 $M_{\odot}$ and [Fe/H] of -0.16. The detailed parameters of the best-fitting model are listed in Table 3.4, which are in agreement with the observations (Table 3.2). The frequency échelle diagram of the best model frequencies are given in Figure 3.6. Despite the small deviations between observed and computed mixed dipolar modes, the surface-effect corrected model frequencies fit the observed frequencies very well, which enhance the reliability of the best model. We failed to give reliable errors for the model parameters because of the extremely large χ^2 values.

Table 3.5: 46 LMi observation and best-fitting model properties

Parameter	Value
Spectroscopic Properties	
$T_{\rm eff}$ (K)	4677 ± 110
$\log g$ (cgs)	2.96 ± 0.1
[Fe/H]	-0.2 ± 0.10
Astrometry Properties π (mas)	33.48 ± 0.21
Asteroseismic Properties	
$\nu_{\rm max}$	58 ± 1.0
$\Delta\nu$	5.80 ± 0.12
Derived Properties	
$L(L_\odot)$	34 ± 2
$R(R_\odot)$	8.22 ± 0.22
$M(M_\odot)$	1.24 ± 0.22
Best-fitting Model Properties $M(M_\odot)$	1.25 ± 0.13
$R(R_\odot)$	8.31 ± 0.25
$L(L_\odot)$	32.47 ± 4.5
Age (Gyr)	3.94 ± 2.23
$T_{\rm eff}$ (K)	4787 ± 100
[Fe/H]	-0.25 ± 0.3
$\log g$ (cgs)	2.70 ± 0.10

3.3 The First SONG Target, Red Giant Star 46 LMi

The Stellar Observation Network Group (SONG) is a ground based network of 1m-class telescopes with the aim of developing asteroseismology and searching for exoplanets (Grundahl et al., 2014). Thanks to the effort of global group observations, the expected nearly uninterrupted time series is possible to provide high-quality oscillations measurement for solar-like oscillations. The first node of SONG, the prototype of the SONG telescope (the Hertzsprung SONG telescope), is placed at the Teide Observatory, Tenerife. One of the first targets of the first campaigns with the Tenerife site is the red giant star 46 LMi, of which the time series and power spectrum are given in Figure 3.7. The observation length covers around two months, although regular gaps exist on the time series, which are indicated by the window spectrum, and the effective observation length is about 18 days. The limited observation time is not long enough for us to resolve individual oscillation mode peaks. However, by utilizing the technique of auto-correlation, we managed to find the $\Delta\nu$ to be around 5.8 μHz, which is in agreement with the one obtained from the empirical relation between $\nu_{\rm max}$ and $\Delta\nu$ from Huber et al. (2011). The basic parameters that are derived from spectroscopy or the Hipparcos mission (van Leeuwen, 2007) are listed in Table 3.5. Among the derived properties, luminosity and radius are from literature (Piau et al., 2011) and the mass is the mean value of the ones estimated from the scaling relation using equation (1.15) and the interferometric radius in Table 3.5.

Using these observed and derived properties as constraints, we can select the model that has parameters matching them best. Due to the fact that limited observation time could not permit us to resolve many individual frequencies and we could only identify three modes in total, the best models are not well resolved from the χ^2 grid of Figure 3.8, which is reflected by large area of low χ^2 values resulting large errors of model parameters. The errors of model parameters are estimated by increasing the χ^2 values by one from the lowest. This can be overcome by longer observations and global network of SONG which will efficiently reduce the gaps of the time series that can allow more seismic parameters to be measured.

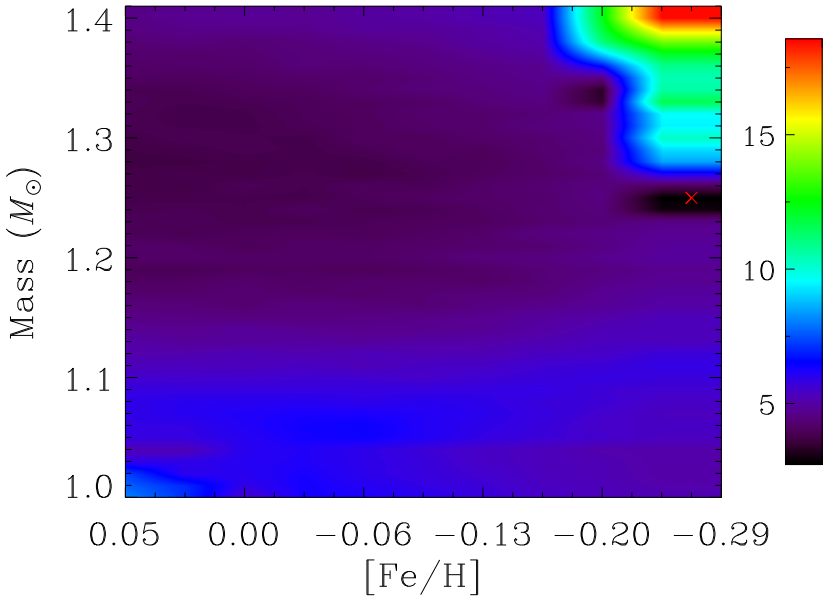

Figure 3.8: χ^2 calculated based on the observation constraints for the first SONG red giant 46 LMi. Similar to Figure 3.4, the values of χ^2 are indicated by the color. The lower the χ^2 is, the black is more black. The x-axis is the metallicity of the models and y-axis is the mass. The red cross indicates the location of the 'best fitting model'.

Chapter 4

Mixed Modes

In main-sequence stars, p modes and g modes are trapped in their own cavities. When stars evolve to the giant stage, the very large gravitational acceleration in the core opens up the possibility that the two cavities could couple with each other, making these coupled modes have p-mode character in the outer part of stars and g-mode character in the core area, for which they are called *mixed modes*. Thanks to the high quality of the photometry data from *Kepler* and *CoRoT*, many recent analyses of oscillations in red giant (RG) stars have been done (e.g. Hekker et al., 2009; Bedding et al., 2010; Huber et al., 2010; Jiang et al., 2011; Mathur et al., 2011; Mosser et al., 2011; Baudin et al., 2012; Kallinger et al., 2012), which prove that using mixed modes is a robust tool to probe the inner structure and evolution of these evolved stars (Beck et al., 2011, 2012; Bedding et al., 2011; Mosser et al., 2012). In this chapter, we discuss the properties of mixed modes in red giant stars theoretically. Section 4.1.1, 4.1.2 and 4.2 are from our published paper (Jiang & Christensen-Dalsgaard, 2014).

4.1 Properties of Mixed Modes

When stars evolve to post-main-sequence stages, the large gravitational acceleration in the core increases the upper limit of the frequency range that g modes can reach, which results in the coupling of p modes and g modes. As a result, these coupled modes undergo so-called *avoided crossing* and *mode bumping*, their frequencies being shifted from the regular spacings indicated by the asymptotic descriptions.

The amplitudes of solar-like p modes are large enough to be detected. On the other hand, for a red giant star the very large mode inertia of solar-like g modes make them almost impossible to be detected directly on the stellar surface (*cf.* equation (1.2). However, when a mode have mixed character of p and g mode, its inertia increase to a certain level, which is determined by its phase, making them observable. As shown in the power spectrum of the red giant star KIC 3744043 (cf. upper panel of Figure 4.1), the $l = 1$ modes are observed as mixed modes which form several clusters of peaks

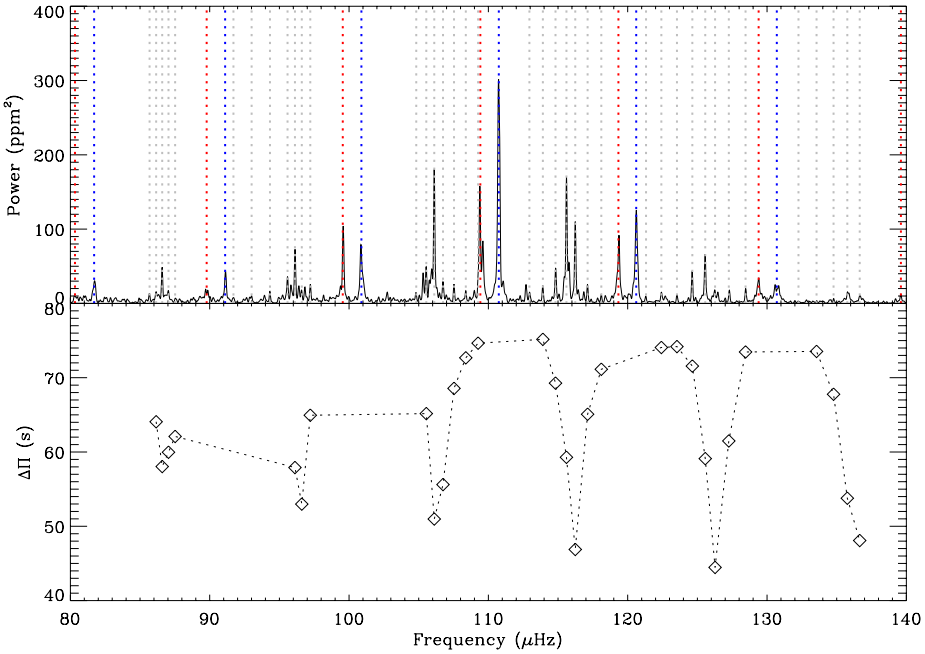

Figure 4.1: Upper panel, the background corrected power spectrum of the *Kepler* red giant star KIC 3744043. The mode identification was done by Mosser et al. (2012). The peaks of $l = 0, 1$ and 2 modes are guide by dashed lines colored in blue, red and grey, respectively. Lower panel, period spacing $\Delta\Pi$ of the $l = 1$ mixed modes above as a function the mode frequencies. Only mixed modes have consecutive g-mode radial order, $n_{\rm g}$ are plotted.

in the plot. Those modes having the same p-mode radial order, $n_{\rm p}$, locate in the same cluster (will be discussed later). Modes possessing more p mode character have higher amplitudes than other mixed modes in a cluster. Mosser et al. (2012) extracted 66 modes, including 50 $l = 1$ mixed modes which enable us to estimate the period spacing $\Delta\Pi$ simply by calculating the period differences of modes with consecutive g-mode radial orders, $n_{\rm g}$. The resulted $\Delta\Pi$ are given in the lower panel of Figure 4.1.

As indicated by the asymptotic relation for g modes (*cf.* equation (1.16)), the periods of pure g modes are equally spaced by $\Delta\Pi$. When the mode is mixed with p character, its period changes leading to a reduction of $\Delta\Pi$. Similar to the frequency échelle diagram of p modes, it is convenient to plot these mixed modes in a period échelle diagram, of which the x-axis is defined as the period modulo the period spacing $\Delta\Pi$. Figure 4.2 shows the period échelle diagram for all the mixed modes extracted from KIC 3744043 power spectrum. Periods of pure g modes would stack up vertically in this diagram, while those of mixed modes drift sidewards and form a 'S' shape pattern per $\Delta\nu$-wide interval. Using this kind of period échelle diagram we may measure $\Delta\Pi$ by making the mixed modes align regularly in the plot. However, this approach is not accurate enough.

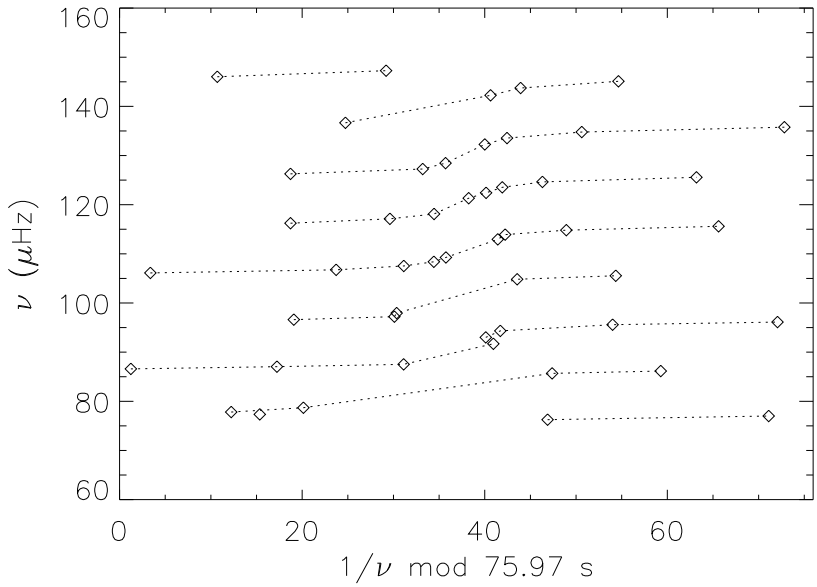

Figure 4.2: Period échelle diagram for all the mixed modes extracted from KIC 3744043 power spectrum. Modes with same $n_{\rm p}$ are connected by a dashed line.

With the intention of asymptotic analysis, we follow a 1.3 $M_\odot$ RG model with initial solar parameters that was calculated by the ASTEC evolution code and the ADIPLS oscillation package. Its evolutionary track is illustrated in Figure 4.3. Several different cases of mixed modes will be discussed in the following sections. We selected four models at different locations on the evolution track (see Fig. 4.3), including one sub-giant model M_1 and three ascending branch models M_2 to M_4. Details of these models will be given in Section 4.2.1. Figure 4.4 shows the evolution of the oscillation modes for the 1.30 $M_\odot$ model, as functions of stellar age and radius. The frequencies in the figure have been scaled according to the inverse of dynamical time-scale $t^{-1} = (R^3/GM)^{-1/2}$, which makes the frequencies of acoustic modes vary little with time. There are clear uniform spacings between p modes. On the other hand, the scaled frequencies of gravity modes (see solid lines at the lower-left corner) have an increasing trend with age, which is a consequence of the increase in N. However, the striking feature of the frequencies in Figure 4.4 is the interaction between the dipolar acoustic and gravity modes. At an early age when the star just leaves the main sequence, the high-order modes are only pure p modes, while g modes are located at low frequency but gradually increasing with time. When the frequencies of the g modes are high enough to interact with p modes, the horizontal lines of p modes are bumped up to relatively higher values, which breaks the equally spaced pattern of p modes. These interactions take place through a series of avoided crossings when the two modes exchange nature. On the other hand, as the star ages, g modes dominate the whole frequency range, while p modes can only be revealed in terms of mixed modes. In this

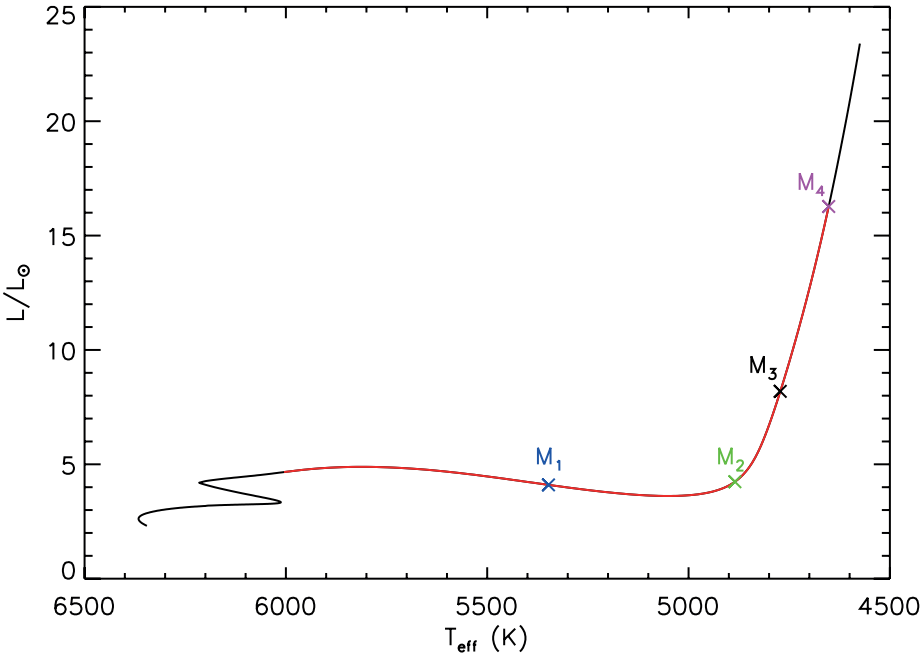

Figure 4.3: Evolution track of the 1.30 $M_\odot$ model. The red part covers all the modes shown in Figure 4.4. The three crosses indicate the selected models coloured the same way as in Figure 4.4 plus an additional more evolved RG model M_4 (purple cross).

case, frequencies will be diminished when avoided crossings happen, which form the very dense p-dominated mixed modes (see Section 4.1.2) in the time sequence that still can be observed as very dense horizontal lines in Figure 4.4.

The detection of mixed modes reveals the mystery of g–mode behaviour in solar-like RG stars. The variations of their mode inertia, frequencies, energy inputs lead us directly to the study of the stellar interior. We will introduce the character of mixed modes theoretically and asymptotically, but to very good approximations.

4.1.1 Asymptotic analysis

The behaviour of oscillations can be described by the set of differential equations (1.30) and (1.31), where v and w are related to the oscillation displacement $\boldsymbol{\delta r}$ in radial and horizontal direction, respectively. Solving these equations can give us the idea of the eigenfunctions which are helpful for the analysis of different modes. However, it is numerically difficult to solve them. Unno et al. (1989) solved the set of differential equations (1.30) and (1.31) asymptotically to obtain v and w using the JWKB method (or Jeffreys, Wentzel, Kramers and Brillouin; Gough 2007) and found that there is a

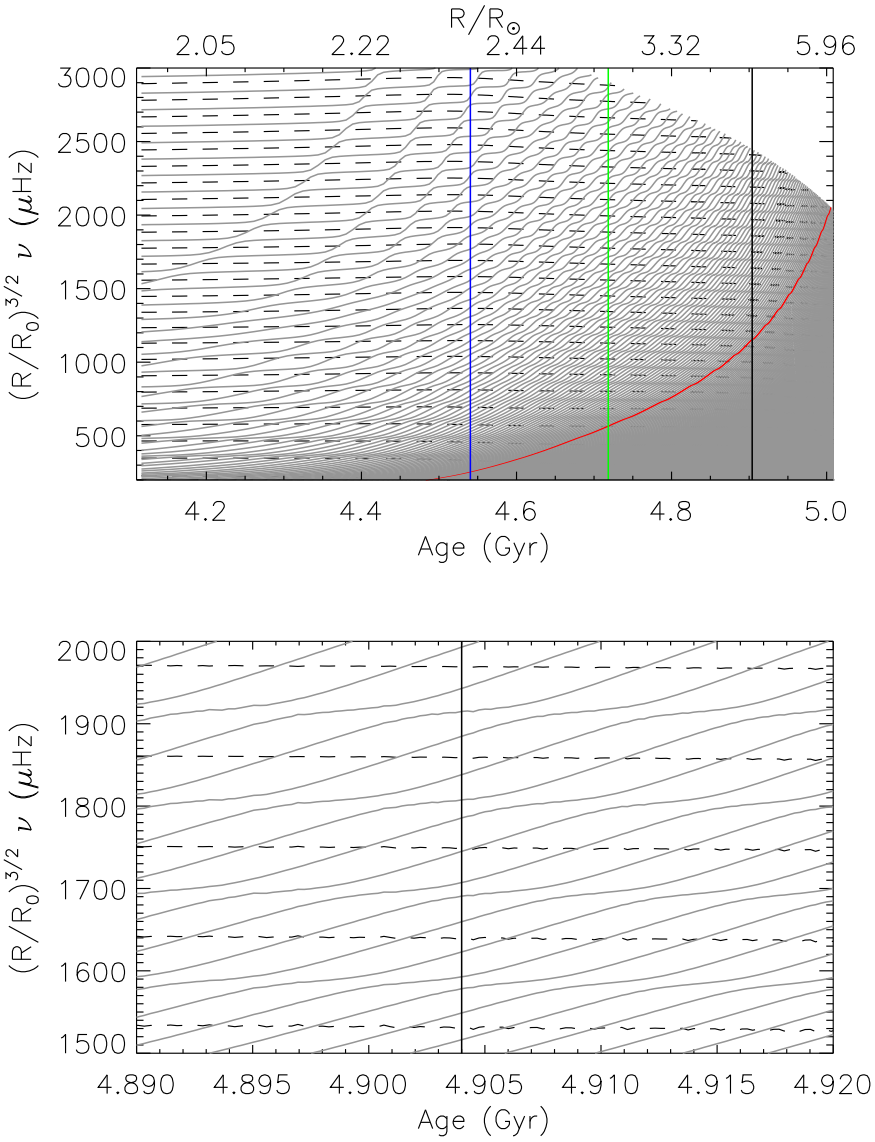

Figure 4.4: Scaled oscillation frequencies as a function of age and radius in the 1.30 $M_\odot$ model. The models in the upper panel start from the subgiant to the RG stage, while the lower panel shows a small segment of the solutions around the age of 4.904 Gyr. On the y-axis, R is the surface radius of the model and R_0 is the zero-age main-sequence radius. Modes with the same radial order have been connected in the same line. The dashed lines are for radial modes and the solid lines for $l = 1$. The three vertical lines indicate three models. Together with the last model they are discussed in detail, and their locations are shown in the evolution track of Figure 4.3. Evolution of one g mode with $n = -50$ is highlighted as a red curve and is described in Section 4.1.2. The computations of frequencies stop at the acoustic cut-off frequency, which leaves the blank area in the upper figure.

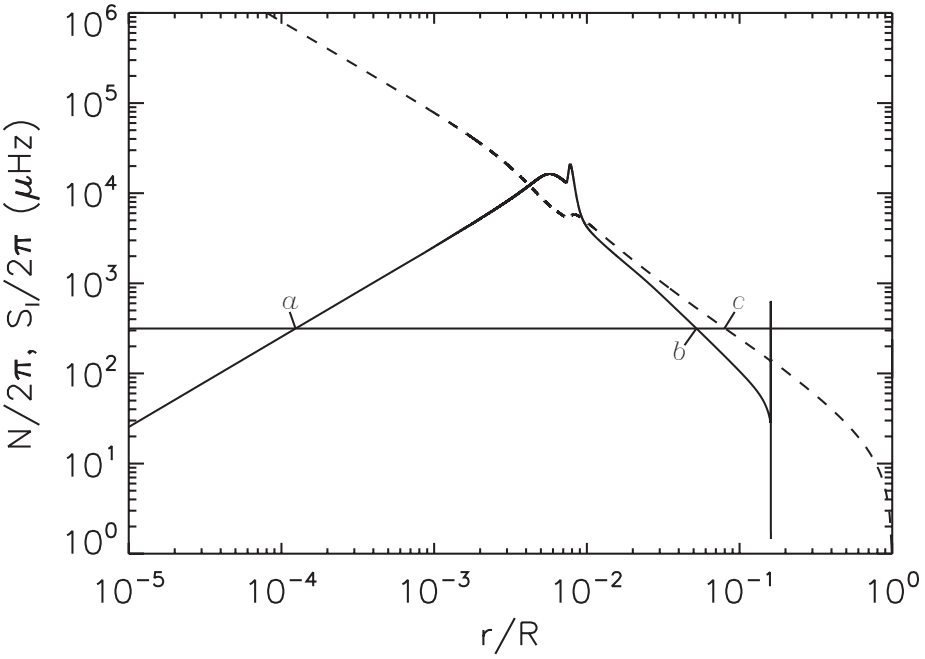

Figure 4.5: Propagation diagram of model M_3. The buoyancy frequency (solid curve) and Lamb frequency (dashed curve, $l = 1$) are shown in terms of corresponding cyclic frequencies, against fractional radius r/R. The axes are in logarithm. The horizontal line indicates the mode frequency $\nu = 315.26$ μHz, which presents mixed-mode character. The locations of turning points of equation (1.32) are indicated by the letter a, b and c, which divide the model into different propagation zones.

general eigenvalue conditions for p and g modes ,

$$\int_{r_1}^{r_2} K \mathrm{d}r = \pi(n + \epsilon) \ . \tag{4.1}$$

Here n is the mode order, and r_1 and r_2 are adjacent turning points (where $K = 0$), between which K^2 is positive. ϵ is a phase correction that depends on the structure of the model near the turning points. The dependence of ϵ on frequency is implied in the definition of K, which can be explored numerically by using equation (4.1) (Christensen-Dalsgaard, 1984). We note that the derivations of equations (1.30) and (1.31) neglected terms that may lead to singularities at critical points in the model, although typically in *evanescent* regions where $K^2 < 0$. This is explicit in a second-order equation, exact in the Cowling approximation, presented by Gough (1993), which is of the same form as equations (1.30) and (1.31) but expressed in terms of a different dependent variable.

The asymptotic relations for pure p and g modes are given in equation (1.8)

and (1.16). In order to discuss a similar asymptotic relation for mixed modes, the propagation diagram of model M_3 (see Section 4.2.1 for details of the model) is shown in Figure 4.5 with eigenfrequency of 315.26 μHz indicated by the horizontal line that intersects with the characteristic frequencies at turning points 'a', 'b' and 'c'. In this case, g modes are trapped in the interval between the layer very close to the innermost point 'a' and 'b', while p modes travel in the outer part of the star between 'c' and the surface, where K^2 is positive for both cases. The region between 'b' and 'c' is called the evanescent region where K^2 is negative and the eigenfunctions behave exponentially. Equation (4.1) can be considered as an eigenvalue condition for p and g modes (Unno et al., 1989). For g modes:

$$\int_{r_\mathrm{a}}^{r_\mathrm{b}} K \mathrm{d}r \approx \pi(n + 1/2 + \epsilon_\mathrm{g}), \tag{4.2}$$

and for p modes:

$$\int_{r_\mathrm{c}}^{R} K \mathrm{d}r \approx \pi(m + \epsilon_\mathrm{p}), \tag{4.3}$$

where n and m are integers that also define the orders of p and g modes, individually. In the present case, with a radiative core, r_a is very close to the centre. If there is a convective core, the deeper boundary of g modes is outside the core.

Unno et al. (1989) describe an eigenvalue condition for mixed modes using a coefficient q measuring the coupling strength between gravity-wave and acoustic-wave cavities:

$$\cot\left(\int_{r_\mathrm{a}}^{r_\mathrm{b}} K \mathrm{d}r\right) \tan\left(\int_{r_\mathrm{c}}^{R} K \mathrm{d}r\right) = q \; . \tag{4.4}$$

[A qualitatively similar relation was obtained by Christensen-Dalsgaard (2012) from the analysis of a simple toy model.] As discussed below, equation (4.4) has been a very powerful tool in the analysis of mixed modes in RGs (e.g., Mosser et al., 2012), with the coupling strength q obtained by fitting the expression to observed or computed frequencies of oscillation.

It is of obvious interest to investigate how the coupling strength reflects the properties of the stellar interior. From a simple analysis of equations (1.30) – (1.32), Unno et al. (1989) obtained the estimate

$$q_\mathrm{int} = \frac{1}{4} \exp\left(-2 \int_{r_\mathrm{b}}^{r_\mathrm{c}} |K| \mathrm{d}r\right) \; . \tag{4.5}$$

We note that this is obviously questionable, given the problems with singularities discussed above. Even so, we find it interesting in the following to compare q_int as computed from equation (4.5) with the results of frequency fits.

When the coupling is very weak, q is close to 0. It is reasonable to estimate that q is a small quantity and there is a condition that satisfies equation (4.4):

$$\left.\begin{aligned} \int_{r_\mathrm{a}}^{r_\mathrm{b}} K \mathrm{d}r &\approx \pi(n + 1/2 \pm \epsilon) \\ \int_{r_\mathrm{c}}^{R} K \mathrm{d}r &\approx \pi(m \mp \epsilon) \end{aligned}\right\} . \tag{4.6}$$

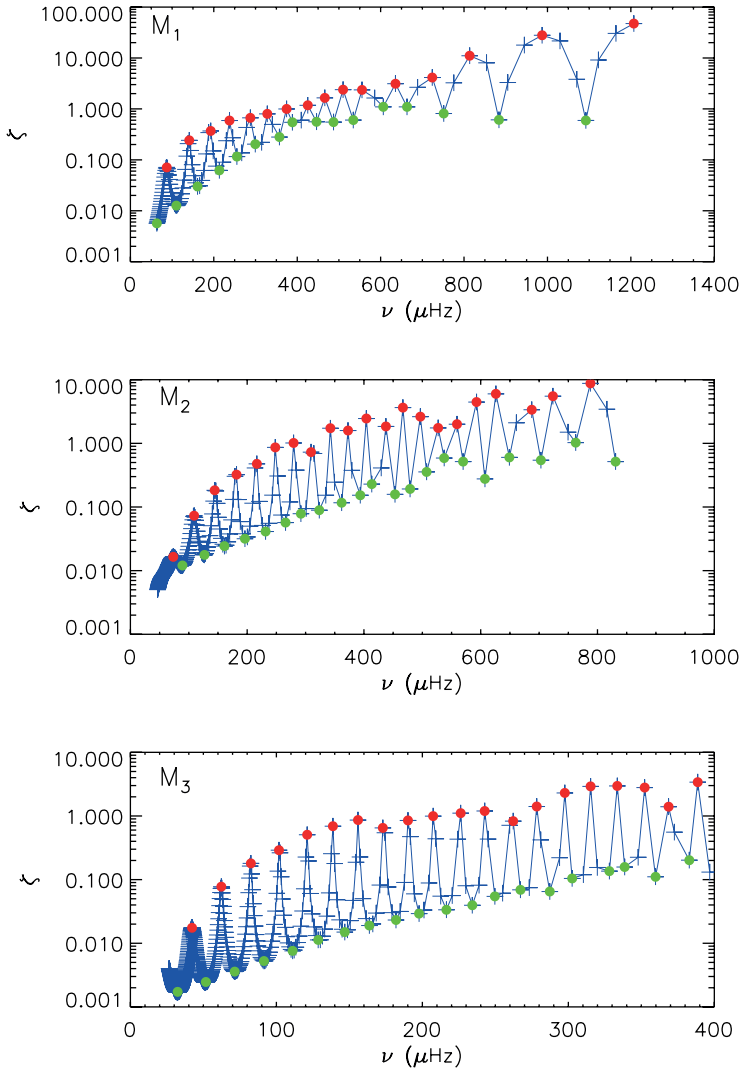

Figure 4.6: The ratio of dimensionless mode inertia in the p cavity over the one in the g cavity of the three models, as a function of frequency. The blue crosses represent the ratios for each oscillation mode. Green circles are the most g-m-like mixed modes while red circles indicate the most p-m-like mixed modes.

It should be noted that equation (4.4) is the general condition even for pure p and g modes if we take $q = 0$. When mixed modes occur, the small value of q leads to deviations from pure oscillation modes, which are indicated by corresponding $\pm$ and $\mp$ signs in equation (4.6). From equation (1.32) K only depends on the frequency for a given model. So the occurrence of oscillation modes is also determined by the frequency. Hence let us consider a model with frequency gradually increasing. In the

very beginning, the frequencies are very small making the integrals in equation (4.2) so great that a large number of g modes satisfy equation (4.2). However, there is no p mode existing at the very low frequency range because $S_l \gg \omega^2$. As the frequency increases, the region in which gravity waves are trapped becomes narrower and therefore the integral of K monotonically decreases. But once the frequency is greater than S_l the integral over acoustic-wave zone monotonically increases. If the frequency is high enough to make gravity and acoustic waves couple with each other meaning that the integrals of K approach $(n-1/2)\pi$ and $(m+1)\pi$ at the same time, the eigenvalue condition equation (4.6) is satisfied and an avoided crossing occurs. When the frequency increases beyond N, only equation (4.3) can be satisfied by p modes.

4.1.2 Classification

With the help of models we can study properties of mixed modes by observing some parameters that characterize oscillation modes, such as kinetic energy (Unno et al., 1989) or mode inertia . The normalized mode inertia is given by equation (1.3). For a mode that is dominated by p-mode nature, the inertia is contributed mostly by the p cavity, which is mainly from $\xi_{\rm r}$. For a mixed mode that behaves predominantly g-mode like, the inertia would be very large owing to the high density in the core area and hence is dominated by $\xi_{\rm h}$ in the g cavity (Aerts et al., 2010). Therefore it is convenient to measure the nature of mixed modes with the ratio of mode inertia in the p cavity over that in the g cavity:

$$\zeta = \frac{E_{\rm p}}{E_{\rm g}} \approx \frac{\int_{r_{\rm c}}^{R} \xi_{\rm r}^2 \rho r^2 {\rm d}r}{\int_{r_{\rm a}}^{r_{\rm b}} L^2 \xi_{\rm h}^2 \rho r^2 {\rm d}r}. \tag{4.7}$$

Unlike Mosser et al. (2012) dividing mixed modes into two categories by the size of the amplitude in the core (see also Goupil et al. 2013), we divide them by the local extreme values of ζ, namely those mixed modes having the local maxima of ζ and their vicinities are called p-m modes and those at the local minima correspond to g-m modes. Although low-frequency mixed modes are principally dominated by g-mode nature ($\zeta \sim 0$), they are always coupling with p modes at different levels. When the coupling effect is strong, the mode tends to have more p-mode nature which leads to an increase in ζ but decrease in frequency. On the other hand, for larger frequency modes where the p character dominates and ζ is very large ($\zeta \gg 1$), their frequencies would be bumped up to a higher value but their ζ values are diminished when the coupling with the g-mode character is strong. The frequencies of these p-m modes are close to the frequencies of pure dipolar p modes, because they are little affected by the g cavity, and they can be observed clearly. Similarly, g-m modes are close to pure g modes. Additionally, mixed modes that have nearly equal mode inertia contributions from the envelope and the core take values of ζ of the order of 1. They also have a significant g component that is valuable for stellar interior research, and may also be observed directly. The variation of ζ in dipolar modes with frequency is shown in Figure 4.6, p-m and g-m modes being illustrated by colored dots.

Since M_1 is a subgiant model, there exist high-order p modes as well as g modes. For mixed modes in the g-mode frequency range, g-m modes are expected to align

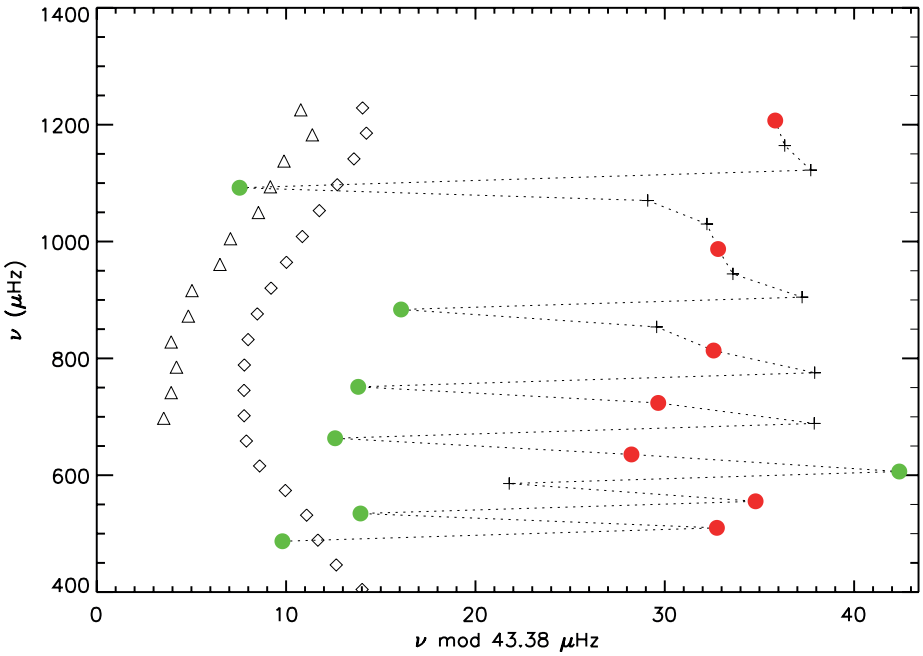

Figure 4.7: Frequency échelle diagram of oscillation modes ($n > 0$) in M_1. Modes of different degrees are indicated by diamonds ($l = 0$), crosses ($l = 1$) and triangles ($l = 2$). Green and red circles correspond to the same kinds of mixed modes as in Figure 4.6. To guide the eyes, the dotted line connects the dipolar mixed modes. Mixed modes for $l = 2$ modes are suppressed in the plot.

vertically in the middle of the S-pattern in the period échelle diagram, while modes affected by p-mode character shift sidewards as p-m modes locating at the edge of the S-pattern. For higher frequency mixed modes which have significant p-mode nature, p-m modes line up more or less vertically as radial modes do in frequency échelle diagram (red circles in Figure 4.7) while modes affected by g-mode character shift sidewards as g-m modes positioning at the edge of each pattern (green circles in Figure 4.7).

In summary, when the coupling is strong, g-dominated mixed modes usually have small values of ζ which increase because of the kinetic energy contributions from the envelope increase. In contrast, the large ζ values of p-dominated mixed modes decrease as a result of the effect by g-m modes. This is clearly seen by the study of the evolutionary variations of a g mode ($n = -50$), in terms of frequency and ζ (Fig. 4.8). The frequency of the mode increases smoothly at an early age, though there are some tiny influences from p modes which make ζ grow a little but remain small ($\zeta \ll 1$). When it ages to around 4.8 Gyr, the frequency decreases at the point where the local maximum of ζ is close to 1, which means the effect of avoided crossing is much greater than earlier. And a series of crossings followed with decreasing period means the p-mode character is becoming obvious because of the increasing coupling, and the possibility of this former pure g mode being detected is increasing too.

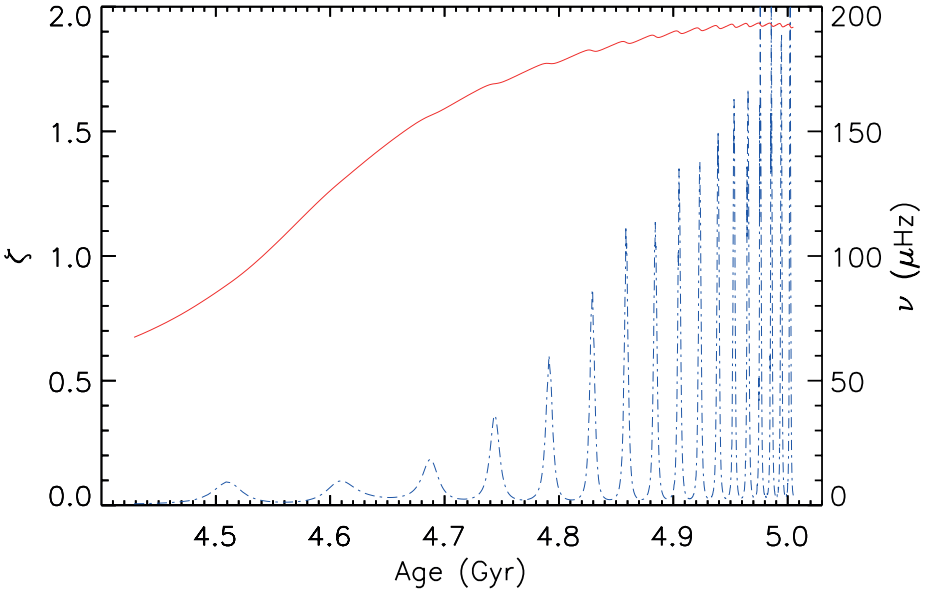

Figure 4.8: The evolutionary view of frequency (red solid line) and ζ (blue dash-dotted line) of a g mode ($n = -50$). The frequencies are indicated by the right y-axis.

4.1.3 Eigenfunctions of oscillation modes

In order to solve the set of differential equations (1.30) and (1.31), we may make use of the Airy functions. The solution y to the differential equation that has the form of

$$\frac{\mathrm{d}^2 y}{\mathrm{d}x^2} + xy = 0 \,, \tag{4.8}$$

is represented by

$$y = aAi(x) + bBi(x) \,, \tag{4.9}$$

where $Ai(x)$ and $Bi(x)$ denote the first and second kind of the Airy functions, respectively, which are related to the Bessel functions of 1/3 order as

$$Ai(x) = \frac{1}{3}\left[x^{1/2} J_{-1/3}\left(\frac{2}{3}x^{3/2}\right) + x^{1/2} J_{1/3}\left(\frac{2}{3}x^{3/2}\right)\right] \tag{4.10}$$

$$Bi(x) = \frac{1}{\sqrt{3}}\left[x^{1/2} J_{-1/3}\left(\frac{2}{3}x^{3/2}\right) - x^{1/2} J_{1/3}\left(\frac{2}{3}x^{3/2}\right)\right] \tag{4.11}$$

and a and b are constant coefficients. For large values of $|x|$ and when $x < 0$, $Ai(x)$ and $Bi(x)$ have the following asymptotic behaviour:

$$Ai(x) \sim \frac{1}{2\sqrt{\pi}} (-x)^{-1/4} \exp\left[-\frac{2}{3}(-x)^{3/2}\right] \tag{4.12}$$

$$Bi(x) \sim \frac{1}{\sqrt{\pi}} (-x)^{-1/4} \exp\left[\frac{2}{3}(-x)^{3/2}\right] \tag{4.13}$$

and when $x > 0$

$$Ai(x) \sim \frac{1}{\sqrt{\pi}} x^{-1/4} \cos\left[\frac{2}{3}x^{3/2} - \frac{\pi}{4}\right] \tag{4.14}$$

$$Bi(x) \sim -\frac{1}{\sqrt{\pi}} x^{-1/4} \sin\left[\frac{2}{3}x^{3/2} - \frac{\pi}{4}\right] . \tag{4.15}$$

It is derived by Unno et al. (1989) that the form of the function w is given by

$$w = |K|^{-1/2} \left(\left|\frac{3}{2}\int_{r_a}^{r} |K| \mathrm{d}r\right|\right)^{1/6} [aAi(x) + bBi(x)] , \tag{4.16}$$

where x is expressed by

$$x = \mathrm{sgn}(K^2) \left(\left|\frac{3}{2}\int_{r_a}^{r} |K| \mathrm{d}r\right|\right)^{2/3} \tag{4.17}$$

and the symbol $\mathrm{sgn}(x)$ is a function that extracts the sign of x. On the other hand, the form of v is given by

$$\begin{aligned} v &= \mathrm{sgn}(Q)|K|^{-1} \left(\frac{\mathrm{d}w}{\mathrm{d}r} + \frac{1}{2}\frac{\mathrm{d}\ln|Q|}{\mathrm{d}r} w\right) \\ &\simeq \mathrm{sgn}(Q)|K|^{-1} \frac{\mathrm{d}w}{\mathrm{d}r} , \end{aligned} \tag{4.18}$$

where Q is

$$Q(r) = \frac{1}{r^2}(\omega^2 - N^2) h(r)^{-1} , \tag{4.19}$$

$h(r)$ being

$$h(r) = \exp\left[\int_0^r \left(\frac{N^2}{g} - \frac{g}{c^2}\right) \mathrm{d}r\right] > 0 . \tag{4.20}$$

Thus ξ_r and ξ_h, which are directly related the eigenfunctions of displacement vector (*cf.* equation (1.27)), are related to v and w through

$$\xi_\mathrm{r} = \rho^{-1/2} c^{-1} r^{-1} \left(\left|1 - \frac{S_l^2}{\omega^2}\right|\right)^{1/2} v \tag{4.21}$$

and

$$\xi_\mathrm{h} = \omega^{-2} \rho^{-1/2} r^{-2} (|N^2 - \omega^2|)^{1/2} w . \tag{4.22}$$

For the most complicated case of a mixed mode, the mode has g-mode character in the core area and p-mode character near the surface, and a evanescent region between them. Substituting x of the p, g mode and the evanescent regions into equation (4.16) and (4.18), we can estimate w and v which leads to ξ_r and ξ_h directly. Figure 4.9 shows

computed eigenfunctions for a p-m mixed modes in Figure 4.8. The mode has nearly equal mode inertia ratio between p and g cavity ($\zeta \sim 1$). It is clear form the figure that the amplitude $\xi_{\rm r}$ is large in the outer part of the star and the oscillation mode is dominated by p-mode character in that region, while $\xi_{\rm h}$ is the dominant displacement in the very interior area where g-mode character is dominant. Counting the zeros of $\xi_{\rm r}$ and $\xi_{\rm h}$ may give us the number of $n_{\rm p}$ and $n_{\rm g}$. However, it is possible to estimate $n_{\rm p}$ and $n_{\rm g}$ directly from the phase of asymptotic relations (see Section 4.3). The evanescent region, which is between the p and g mode region, has a turning point on each side where $K = 0$ and hence $x = 0$ from equation (4.17). This makes the asymptotic expressions of Airy functions $Ai(x)$ and $Bi(x)$ break down, which require $|x|$ to be very large meaning the oscillation should far away from the turning points. Therefore, this blemish of asymptotic Airy functions for the area around turning points leads to the big jumps in the blown up version of $\xi_{\rm r}$ in the evanescent region which is show in the upper right panel of Figure 4.9. The left turning point shows the position of the outer boundary of the convective core and the right one shows the base of the envelope. Also the lack of a strict treatment of turning point will lead an underestimate of theoretical coupling strength (see Section 4.2).

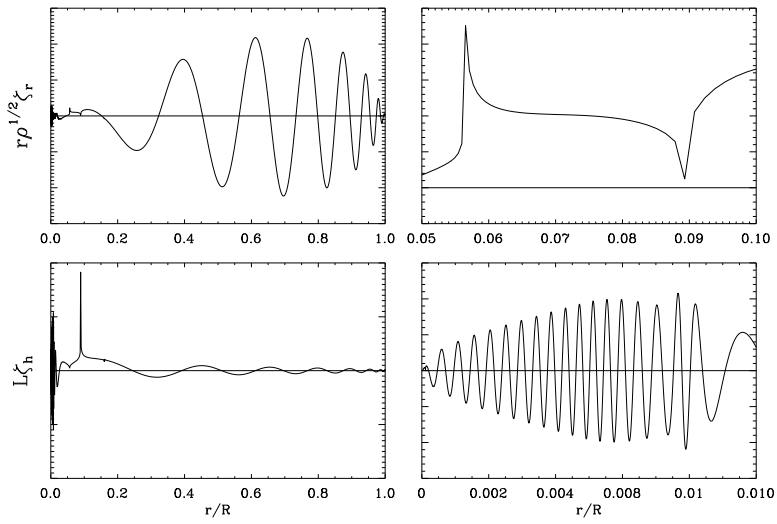

Figure 4.9: Eigenfunctions, on an arbitrary scale, for a selected mixed mode ($l = 1$, $n = -50$, $\nu = 278.25\mu$Hz and $\zeta \sim 1$) from Figure 4.8. The upper two panels show scaled radial displacement eigenfunctions, while the lower two show horizontal displacement eigenfunctions, on different radius scale. The base of the convective envelope locates at about 0.09 R. The y-axis for the four plots are in the same order. The horizontal line indicate the zero point of y-axis.

However, the asymptotic expressions of Airy functions give good estimation for

the eigenfunctions of pure p and g modes under the condition of asymptotic analysis. For a p modes, $\omega^2 \gg S_l^2$ and $\omega^2 \gg N^2$

$$K^2 \simeq \frac{\omega^2}{c^2}\left(1 - \frac{S_l^2}{\omega^2}\right) , \tag{4.23}$$

hence

$$w \simeq a|K|^{-1/2}\frac{1}{\sqrt{\pi}}\cos\left(\int_{r_t}^{r}|K|\mathrm{d}r - \frac{\pi}{4}\right) \tag{4.24}$$

if we take $b = 0$ due to the boundary conditions (Unno et al., 1989) and

$$v \simeq a|K|^{-1/2}\frac{1}{\pi}\sin\left(\int_{r_t}^{r}|K|\mathrm{d}r - \frac{\pi}{4}\right) , \tag{4.25}$$

which lead to the eigenfunctions given by

$$\xi_\mathrm{h} \simeq \frac{a}{\sqrt{\pi}}\omega^{-3/2}\left(\frac{c}{\rho}\right)^{1/2} r^{-2}\left(1 - \frac{S_l^2}{\omega^2}\right)^{-1/4}\cos\left[\int_{r_t}^{r}\frac{\omega}{c}\left(1 - \frac{S_l^2}{\omega^2}\right)^{1/2}\mathrm{d}r - \frac{\pi}{4}\right] \tag{4.26}$$

where r_t denotes the position of turning point. and

$$\xi_\mathrm{r} \simeq -\frac{a}{\sqrt{\pi}}(c\rho)^{-1/2}r^{-1}\omega^{-1/2}\left(1 - \frac{S_l^2}{\omega^2}\right)^{1/4}\sin\left[\int_{r_t}^{r}\frac{\omega}{c}\left(1 - \frac{S_l^2}{\omega^2}\right)^{1/2}\mathrm{d}r - \frac{\pi}{4}\right] . \tag{4.27}$$

For g modes, $\omega^2 \ll S_l^2, N^2$, then

$$K^2 \simeq \frac{L^2}{r^2}\left(\frac{N^2}{\omega^2} - 1\right) , \tag{4.28}$$

and similarly the eigenfunctions become

$$\xi_\mathrm{h} \simeq -\frac{a}{\sqrt{\pi}}L^{-1/2}\rho^{-1/2}r^{-3/2}\omega^{-2}\left(\frac{N^2}{\omega^2} - 1\right)^{1/4}\sin\left[\int_{r_t}^{r}\frac{L}{r}\left(\frac{N^2}{\omega^2} - 1\right)^{1/2} - \frac{\pi}{4}\right] \tag{4.29}$$

and

$$\xi_\mathrm{r} \simeq \frac{a}{\pi}L^{1/2}\rho^{-1/2}r^{-3/2}\left(\frac{N^2}{\omega^2} - 1\right)^{1/4}\cos\left[\int_{r_t}^{r}\frac{L}{r}\left(\frac{N^2}{\omega^2} - 1\right)^{1/2} - \frac{\pi}{4}\right] . \tag{4.30}$$

For mixed modes, the eigenfunctions of p-mode and g-mode regions can be estimated as the same for the pure modes case, and those of the evanescent region, except near the turning points, can be approximated by

$$\begin{aligned}\xi_\mathrm{h} \simeq & \frac{a}{\sqrt{\pi}}(L\rho)^{-1/2}\omega^{-2}r^{-3/2}\Bigg\{ -\frac{1}{2}\sin\left[\int_{r_\mathrm{a}}^{r_\mathrm{b}}\frac{L}{r}\left(\frac{N^2}{\omega^2} - 1\right)^{1/2}\mathrm{d}r\right]\exp\left(-\int_{r_\mathrm{b}}^{r}\frac{L}{r}\mathrm{d}r\right) \\ & + \cos\left[\int_{r_\mathrm{a}}^{r_\mathrm{b}}\frac{L}{r}\left(\frac{N^2}{\omega^2} - 1\right)\mathrm{d}r\right]\exp\left(\int_{r_\mathrm{b}}^{r}\frac{L}{r}\mathrm{d}r\right)\Bigg\}\end{aligned} \tag{4.31}$$

Table 4.1: Fundamental parameters of the 1.30 $M_\odot$ giant models. R and L are surface radius and luminosity, provided in units of the solar values, $T_{\rm eff}$ is effective temperature, $\nu_{\rm max}$ is the estimated frequency at maximum power and $n_{\rm max}$ is the corresponding radial-mode order, $\Delta\nu$ is the acoustic-mode frequency spacing obtained from fitting the frequencies and $\Delta\nu_{\rm int}$ was determined from the asymptotic integral, equation (1.9), and $\Delta\Pi_{\rm int}$ is the asymptotic period spacing of dipolar modes (cf. equation 1.17).

Model	M_1	M_2	M_3	M_4
$R/R_\odot$	2.36	2.88	4.20	6.22
$T_{\rm eff}$ (K)	5347.8	4884.9	4772.2	4651.9
$L/L_\odot$	4.101	4.239	8.189	16.272
$\nu_{\rm max}$ (μHz)	745.24	513.78	252.17	117.62
$n_{\rm max}$	16	15	13	11
$\Delta\nu$ (μHz)	43.38	31.62	17.88	9.89
$\Delta\nu_{\rm int}$ (μHz)	45.32	33.19	18.79	10.38
$\Delta\Pi_{\rm int}$ (s)	191.69	111.73	87.78	75.50

and

$$\xi_{\rm r} \simeq \frac{a}{\sqrt{\pi}}(Lr\rho)^{-1/2}c^{-1}\left\{\frac{1}{2}\sin\left[\int_{r_{\rm a}}^{r_{\rm b}}\frac{L}{r}\left(\frac{N^2}{\omega^2}-1\right)^{1/2}{\rm d}r\right]\exp\left(-\int_{r_{\rm b}}^{r}\frac{L}{r}{\rm d}r\right)\right.$$
$$\left.+\cos\left[\int_{r_{\rm a}}^{r_{\rm b}}\frac{L}{r}\left(\frac{N^2}{\omega^2}-1\right){\rm d}r\right]\exp\left(\int_{r_{\rm b}}^{r}\frac{L}{r}{\rm d}r\right)\right\} \quad (4.32)$$

4.2 Coupling Strength

For evolved stars, the oscillation frequencies shift from their original values because of the avoided crossing which mixes the p and g mode characters together. The strength of the coupling between p and g modes can be measured by the coefficient q which is given in equations (4.4) and (4.5). The strength varies for stars at different evolution stages and varies for different modes in a star. The information it carries for the mixture of the two different oscillation modes character and for the stellar structure is still unclear. Thus, it is of obvious interest to investigate how the coupling strength reflects the properties of the stellar interior.

4.2.1 Frequency Fitting

While a mode is undergoing avoided crossing its frequency deviates a little from its original value which makes K satisfy condition equation (4.6). One can calculate K approximately in different regions separated by turning points (a, b and c in Fig. 4.5) (see Christensen-Dalsgaard, 2012).It should be noted that these approximations are valid except near the turning points. Therefore the integral of K in the outer region

is closely related to $\Delta\nu$ and that in the inner region to $\Delta\Pi$ in this asymptotic analysis (see equations 1.9 and equation 1.17). Substituting $\Delta\Pi$ and $\Delta\nu$ into equation (4.4) yields equation (9) in Mosser et al. (2012):

$$\nu = \nu_{n_{\rm p},\, l=1} + \frac{\Delta\nu}{\pi} \arctan\left[q \tan\pi\left(\frac{1}{\Delta\Pi_1 \nu} - \epsilon\right)\right], \tag{4.33}$$

where $\nu_{n_{\rm p},\, l=1}$ is the uncoupled solutions of p modes and ϵ is the phase shift in equation (1.16) which makes the obtained periods close to $(n + 1/2 + \epsilon)\Delta\Pi_l$ when the coupling is weak (Mosser et al., 2012). Equation (4.33) is the expression for the $l = 1$ mixed modes coupled to the pure p modes $\nu_{n_{\rm p},\, l=1}$. It gives a more intuitive view of the frequency change from pure p modes with only several observable seismic parameters than equation (4.4) that demands the knowledge of the structure of stars. However, a similar expression for p-dominated mixed modes coupled with pure g modes can also be acquired, though the asymptotic relations break down for low radial order modes. But we only focus on the former case in this thesis. With the assumption of the asymptotic relation for p modes, one can approximate $\nu_{n_{\rm p},\, l=1}$ which can be affected by the correction term ϵ to some extent. $\Delta\nu$ is obtained as the mean value of frequency spacings of radial modes, assumed also to be valid for dipole modes. The frequencies ν are either from models or observations.

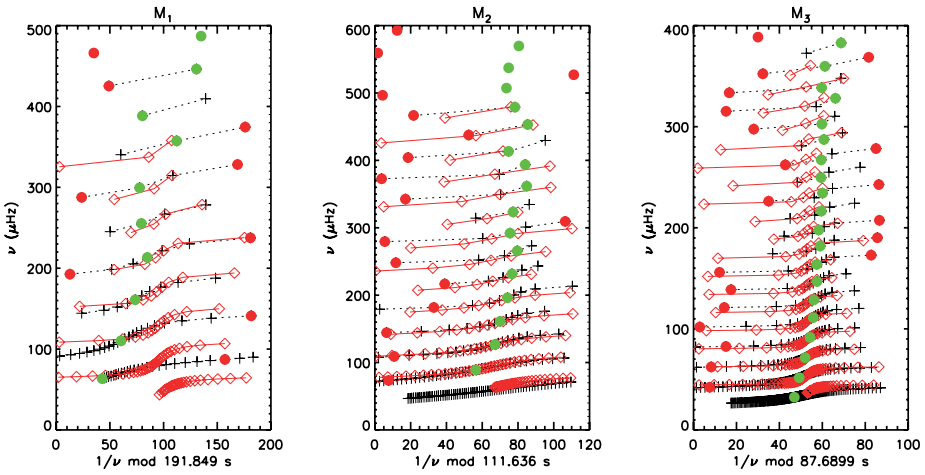

Figure 4.10: Period échelle diagrams for the three models $\mathrm{M}_1 - \mathrm{M}_3$. The x-axis presents the period modulo the period spacing $\Delta\Pi$ gained from fitting and the y-axis is the frequency. Crosses linked by dashed lines indicate the theoretical frequencies. Diamonds correspond to the asymptotic fit. Green circles are the most g-m-like mixed modes while red circles indicate the most p-m-like mixed modes.

Here, we only analyse theoretical modes and use those around the frequency $\nu_{\rm max}$ of maximum power, namely within the range $[\nu_{\rm max} - 3\Delta\nu, \nu_{\rm max} + 3\Delta\nu]$. Since $\nu_{\rm max}$ is not given directly from models, it is scaled from the solar value using the usual scaling relations (Kjeldsen & Bedding, 1995). Hence, $\Delta\Pi$, q and ϵ are left as open parameters and their values are gained after a least-squares fit to frequencies by the

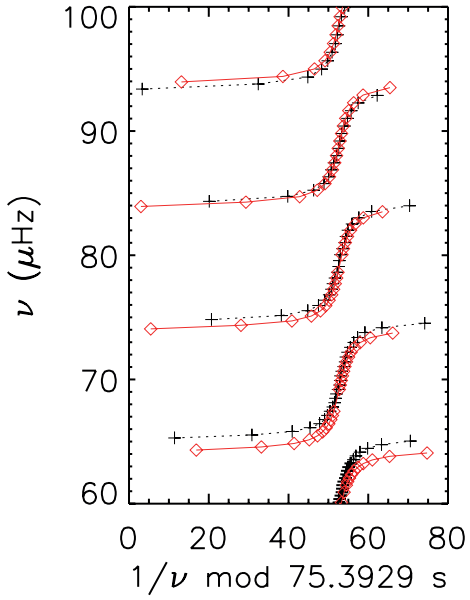

Figure 4.11: Enlarged period échelle diagram for model M_4.

Table 4.2: Results, averaged over the interval $[\nu_{\max}-3\Delta\nu, \nu_{\max}+3\Delta\nu]$, of fitting the asymptotic relation, equation (4.33), to model frequencies.

Model	M_1	M_2	M_3	M_4
$\Delta\Pi$ (s)	191.74	111.98	88.80	75.58
q	0.40	0.23	0.12	0.10
ϵ	0.8	0.1	0.2	0.27

method of grid searching. We constructed grids of q and ϵ from 0 to 1 with a step of 0.01 and 0.1, respectively. $\Delta\Pi$ is searched around a preliminary value, which is estimated by equation (1.17) when fitting only theoretical frequencies, within a small range ($[\Delta\Pi - 3\text{ s}, \Delta\Pi + 3\text{ s}]$). However, if we are confronting observed frequencies, $\Delta\Pi$ is estimated between $\Delta\Pi_{\rm obs}$ and $3\Delta\Pi_{\rm obs}$, where $\Delta\Pi_{\rm obs}$ is the measured value of the period spacing between bumped mixed modes and significantly smaller than $\Delta\Pi$. In this case, more computing time is required, but this is beyond the scope of this thesis. In reality, the coupling strength varies with frequency, but the result from this asymptotic fitting is the mean value $\langle q\rangle$.

We selected four models at different locations on the evolution track (see Fig. 4.3). The first model (M_1) is in the middle of the subgiant branch when p modes are still dominating the high-frequency range. The second model (M_2) lies at the base of RG branch as low-order g modes penetrate into the p-mode area in frequency. The third model (M_3) is on the ascending branch so that g modes are reigning over the frequency range with p modes penetrating in them. The last one (M_4) is farther up on the ascending branch. Their fundamental parameters are given in Table 4.1. For

Table 4.3: Oscillation parameters $\omega_{\rm p}, \omega_{\rm g}$ and q for model M_3 obtained by fitting computed period spacings to equation (4.44), for individual acoustic resonances characterized by $\nu_{\text{p-m}}$. $\Delta\Pi$ and $\Delta\nu$ were calculated from the individual values of $\omega_{\rm g}$ and $\omega_{\rm p}$. For comparison, we also show $q_{\rm int}$ calculated from equation (4.5) at each $\nu_{\text{p-m}}$, and $q_{\rm fit}$ resulting from fitting frequencies within $[\nu_{\text{p-m}} - \frac{1}{2}\Delta\nu$, $\nu_{\text{p-m}} + \frac{1}{2}\Delta\nu]$ to equation (4.33).

$\nu_{\text{p-m}}$ (μHz)	$\omega_{\rm g}$ (s^{-1})	$\omega_{\rm p}$ (μHz)	$\Delta\Pi$ (s)	$\Delta\nu$ (μHz)	q	$q_{\rm int}$	$q_{\rm fit}$
42.22	0.226	42.10	87.51	21.05	0.33	0.031	0.38
62.28	0.226	41.42	87.30	20.71	0.20	0.053	0.25
82.04	0.227	41.05	87.02	20.53	0.16	0.070	0.18
101.79	0.228	40.67	86.72	20.34	0.15	0.084	0.14
120.19	0.229	40.20	86.32	20.10	0.14	0.096	0.13
137.64	0.230	39.44	85.87	19.72	0.14	0.107	0.12
155.92	0.232	38.82	85.19	19.41	0.14	0.116	0.13
172.93	0.233	38.36	84.77	19.18	0.16	0.123	0.12
190.14	0.235	37.93	84.09	18.97	0.17	0.129	0.11
207.39	0.240	37.60	82.36	18.80	0.17	0.134	0.12
224.24	0.238	37.37	83.06	18.68	0.22	0.139	0.12
242.71	0.242	37.23	81.49	18.62	0.20	0.144	0.15
259.86	0.246	37.05	80.12	18.53	0.20	0.149	0.11

the seismic parameters, the large frequency separations $\Delta\nu$ are the mean value taken from radial modes, the period spacings of dipole g modes $\Delta\Pi_{\rm int}$ are the theoretical values derived from the integral of N (equation 1.17) while similarly $\Delta\nu_{\rm int}$ are from the integral of the inverse of the sound speed (equation 1.9), and $n_{\rm max}$ is the radial order at $\nu_{\rm max}$. Since g modes are equally separated in period, it is reasonable to plot them in a period échelle diagram, which is just like the classical échelle diagram for p modes, but the x-axis is defined as the period modulo the period spacing $\Delta\Pi$. Fig. 4.10 shows asymptotic fits to theoretical frequencies of the first three models. Those g-mode-like modes are located in the middle of the pattern, at $1/\nu = \Delta\Pi/2$ (modulo $\Delta\Pi$) if ϵ is 0. As noted by Bedding et al. (2011), the S-pattern per $\Delta\nu$-wide interval observed in Fig. 4.10 is the outcome of coupling. The reason for the g-m modes in M_1 not lining up well is that the radial orders of these modes are relatively low and hence the asymptotic theory is not quite valid. As seen in M_3 of Fig. 4.10, the alignment is much better as there are adequate high-radial-order modes. A higher coupling strength would result in gentle central patterns in each segment. The qualitative agreement of the fit to M_1 mixed modes is not good except for medium radial orders, as expected. This is because q varies with frequency and the mean value $\langle q \rangle$ used in the fitting usually deviates from the real one of each segment. The agreement gets better as the model evolves (see the additional blown-up example of M_4 in Fig. 4.11), but the fitting gives an abnormally high q for M_1 and its vicinity (Table 4.2). Hence, for subgiant models, our obtained mean value of q is not close to the actual coupling coefficient for low-radial-order g mixed modes, which is the reason that this asymptotic fitting method is not suitable for mixed modes in subgiant models. Benomar et al. (2012)

introduced a way to fit mixed modes in subgiant stars[1]. However, the fitting provides reasonable q and $\Delta\Pi$ for models on the ascending branch.

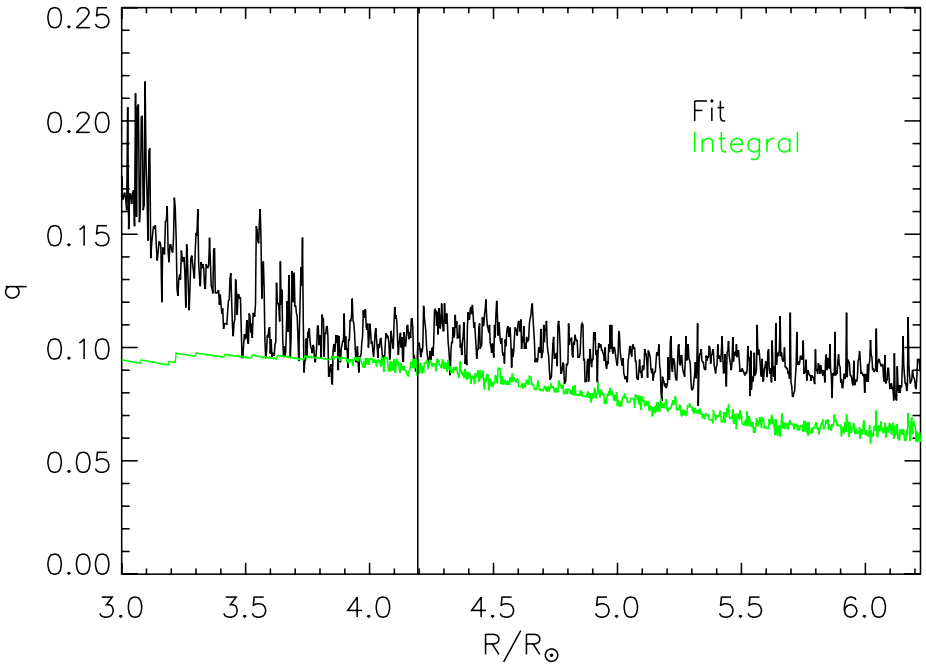

Figure 4.12: Coupling strength obtained from different means indicated by different coloured lines against radius covering all the ascending-branch models in Fig. 4.4. The 'Fit' stands for the asymptotic fitting method (the same as in Table 4.2). The 'Integral' results are calculated from the approximate integral in equation (4.5) and they are the average value of $\nu_{n_{\rm p},\,l=1}$ modes (see Table 4.3). Only modes over the interval $[\nu_{\rm max} - 3\Delta\nu, \nu_{\rm max} + 3\Delta\nu]$ are taken into account for a given model for both methods. The vertical line indicates the location of model M_3, and M_4 is at the end of the figure.

Fig. 4.12 collects the results along the evolution sequence, comparing averages of the fitted values of q with the approximate value obtained from the integral in equation (4.5). As indicated, the fitting results for q are somewhat larger than the values of $q_{\rm int}$ in more evolved models. This is hardly surprising, given the problems associated with the simplified asymptotics, particularly as used in the evanescent region. Concerning these obvious limitations, a relatively simple test is to redo the analysis for frequencies computed in the Cowling approximation. We have done so for model M_4, at the right-hand edge of Fig. 4.12. The average q resulting from the fits to frequencies computed in the Cowling approximation is lower by about 0.02 than when using frequencies computed with the full equations; this, probably coincidentally, brings the results of the fit substantially closer to $q_{\rm int}$. A more detailed analysis is beyond the scope of

[1]They found that the coupling strength of the dipole mixed modes is predominantly a function of stellar mass and appears to be independent of metallicity.

this thesis, however. A solution of ϵ can also be found after the fitting. Although it decides the absolute position of the pattern in the period échelle diagram, it has little influence on the solutions of the fitting (Mosser et al., 2012).

4.2.2 Period Spacing

A dispersion relation can be approximated from equation (4.4):

$$\sin(\omega/\omega_{\rm p})\cos(\omega_{\rm g}/\omega) - q\sin(\omega_{\rm g}/\omega)\cos(\omega/\omega_{\rm p}) = 0 \tag{4.34}$$

where

$$\omega_{\rm g} = L\int_{r_{\rm a}}^{r_{\rm b}} \frac{N}{r}{\rm d}r \simeq \frac{2\pi^2}{\Delta\Pi}, \quad \omega_{\rm p} = \left(\int_{r_{\rm c}}^{R}\frac{{\rm d}r}{c}\right)^{-1} \simeq 2\Delta\nu. \tag{4.35}$$

Although the dispersion relation differs from equation (25) in Christensen-Dalsgaard (2012), we follow derivations in Christensen-Dalsgaard (2012) and rewrite equation (4.34) as:

$$C(\omega)\cos(\omega_{\rm g}/\omega + \Phi(\omega)) = 0, \tag{4.36}$$

where $C(\omega) = \sqrt{\sin^2(\omega/\omega_{\rm p}) + q^2\cos^2(\omega/\omega_{\rm p})}$ and $\Phi(\omega)$ satisfies

$$C(\omega)\cos\Phi(\omega) = \sin(\omega/\omega_{\rm p}) \tag{4.37}$$

$$C(\omega)\sin\Phi(\omega) = q\cos(\omega/\omega_{\rm p}). \tag{4.38}$$

From equation (4.36), it is obvious that the eigenfrequencies satisfy

$$\mathcal{R} = \omega_{\rm g}/\omega + \Phi(\omega) = \left(n + \frac{1}{2}\right)\pi. \tag{4.39}$$

Hence the frequency spacing between adjacent modes nearly satisfies

$$\Delta\omega \simeq \Delta\mathcal{R}({\rm d}\mathcal{R}/{\rm d}\omega)^{-1} = \pi({\rm d}\mathcal{R}/{\rm d}\omega)^{-1}, \tag{4.40}$$

and the corresponding period spacing is approximately given by

$$\begin{aligned}\Delta\Pi &\simeq -\frac{2\pi\Delta\omega}{\omega^2} = -\frac{2\pi^2}{\omega^2}\left(\frac{{\rm d}\mathcal{R}}{{\rm d}\omega}\right)^{-1} \\ &= \frac{2\pi^2}{\omega_{\rm g}}\left(1 - \frac{\omega^2}{\omega_{\rm g}}\frac{{\rm d}\Phi}{{\rm d}\omega}\right)^{-1}.\end{aligned} \tag{4.41}$$

The term outside the parentheses of equation (4.41) is the period spacing for pure g modes, and variations of $\Delta\Pi$ of mixed modes originate from the behaviour of Φ which is illustrated in Christensen-Dalsgaard (2012). Φ is almost constant and therefore its derivative is around zero except near acoustic resonances where Φ changes rapidly, causing a vigorous variation in the period spacing. At the centre of an acoustic resonance, the mode frequency is exactly $\nu_{n_{\rm p},\,l=1}$ in equation (4.33), and $\Phi = \pi/2$, $\omega/\omega_{\rm p} = k\pi$ for integer k. We introduce $\delta x = \omega/\omega_{\rm p} - k\pi$ that represents how much a mode deviates from the centre of an acoustic resonance and expand Φ as $\delta\Phi = \Phi - \pi/2$ in terms of δx. Equations (4.36) and (4.39) yield $\tan(\delta\Phi) = -q^{-1}\tan(\delta x)$, expanding

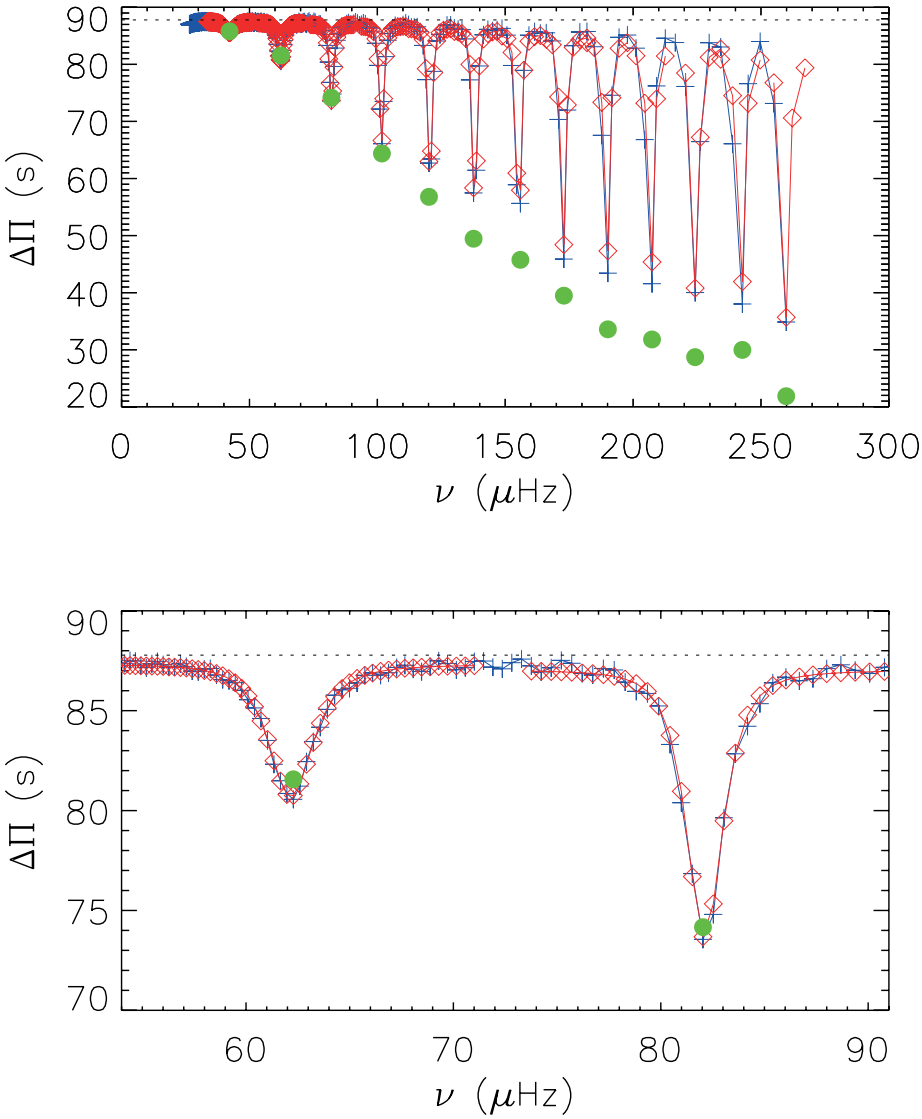

Figure 4.13: Period spacings for g modes of model M_3 (blue crosses) against angular frequency, with solutions to the asymptotic expression equation (4.44) (red diamonds). Green circles are minimum spacings in each segment computed from equation (4.45) using $q_{\rm fit}$ listed in Table 4.3. The horizontal dotted line is the theoretical period spacing of pure g modes defined by equation (1.17). The lower panel shows detailed properties of the second and third segments.

which to the second order gives

$$\delta\Phi \approx -\frac{\delta x}{\sqrt{\frac{2}{3}\delta x^2 + q^2}}, \tag{4.42}$$

which leads to the derivative of Φ as

$$\begin{aligned}\frac{\mathrm{d}\Phi}{\mathrm{d}\omega} &= \frac{\mathrm{d}}{\mathrm{d}\omega}(\delta\Phi + \frac{\pi}{2}) \\ &= \frac{q^2}{\omega_\mathrm{p}(q^2 + \frac{2}{3}\delta x^2)^{3/2}}\end{aligned} \tag{4.43}$$

This leads to the final approximation to $\Delta\Pi$ after plugging equation (4.43) into equation (4.41),

$$\Delta\Pi \simeq \frac{2\pi^2}{\omega_\mathrm{g}}\left(1 + \frac{\omega^2}{\omega_\mathrm{g}\omega_\mathrm{p}}\frac{q^2}{(q^2 + \frac{2}{3}\delta x^2)^{3/2}}\right)^{-1}. \tag{4.44}$$

Therefore the variation of the period spacing is determined by the coupling strength and δx. The minimum period spacing occurs when the mode is extremely close to the centre of the acoustic resonance:

$$\Delta\Pi_\mathrm{min} \simeq \frac{2\pi^2}{\omega_\mathrm{g}}\left(1 + \frac{\omega^2}{q\omega_g\omega_\mathrm{p}}\right)^{-1}. \tag{4.45}$$

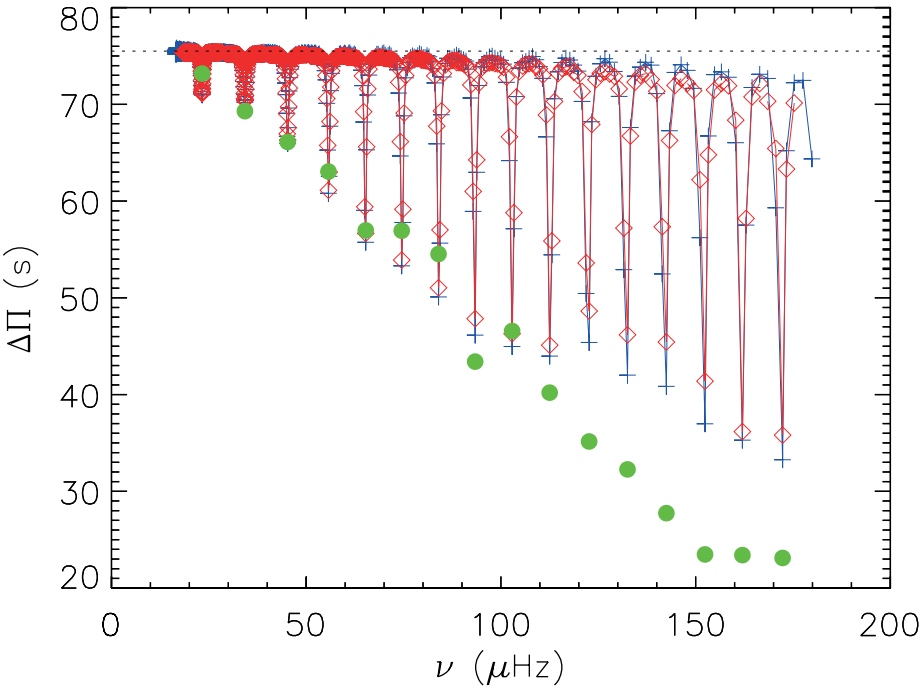

Figure 4.14: Same as the upper panel of Fig. 4.13 for model M_4.

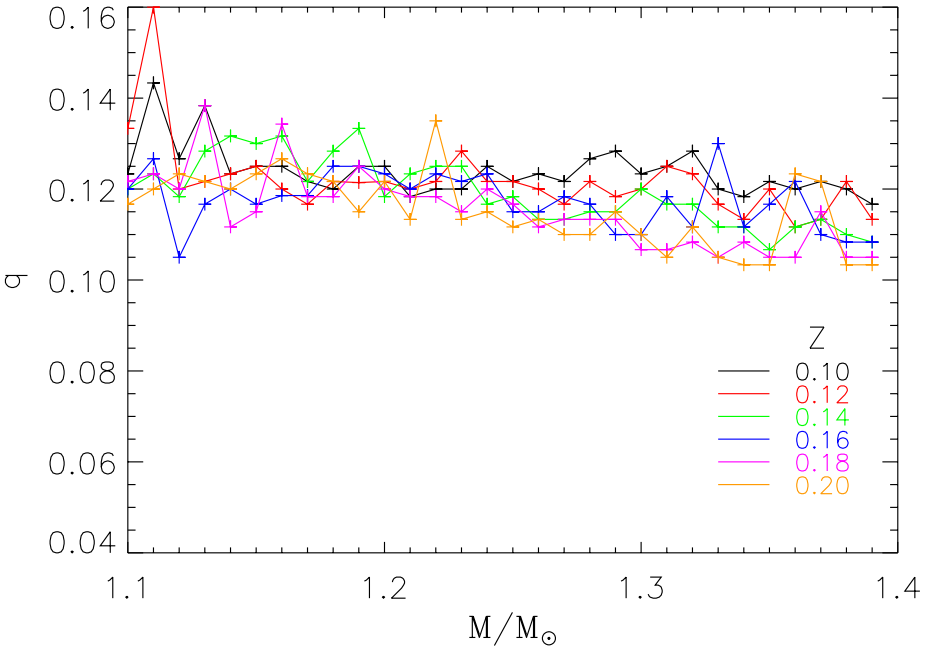

Figure 4.15: Coupling strength as a function of stellar mass. Models with different metallicity are in different colors.

In equation (4.44), $\omega_{\rm g}$ relates to the $\Delta\Pi$ of g-m modes, $\omega_{\rm p}$ corresponds to around twice $\Delta\nu$, and $\delta x \approx 0$ indicates a p-m mode. Therefore, equation (4.44) clearly provides another approach to acquiring $\Delta\Pi$, $\Delta\nu$ as well as q by fitting the period spacings if we have adequate g-m modes. To do this, we focused on M_3 which has a large amount of high-order g modes. Fig. 4.13 presents the fit to the period spacings of M_3. The period spacings of the g-m modes, which are located on the side of each dip, are very close to the theoretical $\Delta\Pi$ calculated from equation (1.17), while the p-m modes lie at the bottom of each dip, as a result of the increase in frequency of these modes. We fit each dip separately in the range $[\nu_{\rm p\text{-}m} - \Delta\nu/2\ ;\ \nu_{\rm p\text{-}m} + \Delta\nu/2]$. Those modes at the bottom of each dip are regarded as p-m modes, which are mixed modes containing gravity mode character as well. They are also possible for detection if their ζ are large enough. As shown in Fig. 4.13, the asymptotic dispersion relation leads to an excellent fit to the theoretical period spacings for low-frequency modes. However, when the g modes are not dense enough, $\omega_{\rm g}$ is underestimated and so therefore is $\Delta\Pi$. The results are displayed in Table 4.3. The coupling strength relates to the depth and width of each dip. According to equation (4.45) the depth of each dip increases with decreasing q, but the width decreases reversely and therefore the chances of finding a g mode decrease too. However, in this exercise we found that the reductions of the period spacing are also very sensitive to the mode frequency. For instance, for low-frequency modes, the small value of the maximum reduction in period spacing of M_3 gives very high q value, compared to the results from other approaches, though they lead to good period spacing calculated from $\omega_{\rm g}$ and mean frequency spacing derived from $\nu_{p\text{-}m}$ ($\Delta\Pi = 87.41 \pm 0.62$ s, $\Delta\nu = 18.04 \pm 0.16$ μHz). We also analysed the

even more evolved model M_4. The resulting q are acceptable in this case thanks to sufficient g modes but the frequency dependence still exists (Table 4.4 and Fig. 4.14). In summary, the outcome of the asymptotic dispersion relation works more robustly for more evolved stars where g modes are dense, but the results have a strong frequency dependence.

Table 4.4: Oscillation parameters for model M_4 obtained by fitting computed period spacings to equation (4.44), for individual acoustic resonances characterized by $\nu_{\text{p-m}}$. See the caption to Table 4.3.

$\nu_{p\text{-}m}$ (μHz)	ω_{g} (s^{-1})	ω_{p} (μHz)	$\Delta\Pi$ (s)	$\Delta\nu$ (μHz)	q	q_{int}	q_{fit}
23.26	0.262	23.25	75.38	11.63	0.05	0.005	0.13
34.26	0.262	22.83	75.24	11.42	0.11	0.012	0.10
45.24	0.263	22.61	75.14	11.30	0.10	0.021	0.11
55.72	0.263	22.30	75.01	11.15	0.09	0.031	0.12
65.29	0.264	21.73	74.88	10.87	0.09	0.041	0.10
74.52	0.264	21.31	74.76	10.66	0.10	0.051	0.13
83.98	0.265	21.02	74.59	10.51	0.10	0.060	0.14
93.38	0.265	20.73	74.35	10.36	0.10	0.069	0.09
102.87	0.266	20.58	74.27	10.29	0.13	0.078	0.13
112.51	0.267	20.48	73.99	10.24	0.13	0.086	0.11
122.64	0.269	20.39	73.48	10.19	0.13	0.094	0.10
132.51	0.269	20.34	73.28	10.17	0.15	0.102	0.10
142.48	0.271	20.30	72.92	10.15	0.17	0.109	0.09
152.40	0.273	20.28	72.40	10.14	0.17	0.116	0.08
162.01	0.272	20.25	72.49	10.13	0.19	0.124	0.09
172.33	0.279	20.24	70.82	10.12	0.16	0.132	0.10

4.2.3 A little more about coupling strength

As discussed above, the coupling strength theoretically depends on the extent of the evanescent region between the p- and g-mode cavity. However, the relation between coupling strength and stellar parameters is still not well understood. We computed models with masses ranging from 1.10 to 1.40 $M_{\odot}$ and Z from 0.01 to 0.02, with a fixing X and α. The models stop when they evolve to the stage that have large frequency separations close to 10.5 μHz. Our models having $\Delta\nu$ of 10.5 μHz are red giant models. Using the fitting method for mixed mode frequencies, we obtained their coupling strength and plotted it as a function of mass in Figure 4.15. Similar to the results we obtained in Figure 4.12, here the resulted coupling strength have variations with masses in the order of 0.02. The variations in low-mass models are relatively larger than those in high-mass models. We found the strength changes little with mass but more with metallicity. The strength has an very obscure tendency to decrease when model mass increases, but its dependence on metallicity is much clearer. Models with lower metallicity tend to have larger coupling strength than those with higher metallicity. However, it should be noted that in this work, the effects of varying

α has not been tested, which definitely should be done in the future.

4.3 Using phase shift to characterize the mixed modes in red giant stars

In this section, we continue the asymptotic analysis of mixed modes in red giants. This includes a detailed discussion about the eigenvalue conditions for mixed modes, and then extends the discussion to some general properties of mixed modes and use of the phase shift in the asymptotic descriptions. The pair of eigenfunction condition equations (4.6) is also conditions for pure g and p modes when $q = 0$ and hence ϵ should be replaced by corrections according to modes. For a mixed mode, any deviations from pure oscillatory modes, which caused by coupling, are implied by the very term ϵ and the $\pm$ and $\mp$ signs. We selected two models of the 1.3 $M_\odot$ red giant model of Figure 4.3 for the discussions in this section. Along the evolutionary track, one sub-giant model $M_{\rm s}$ is selected to present the case that p modes undergoing avoided crossings, while one red-giant model $M_{\rm r}$ is picked up to present g-mode case. Because in the sub-giant branch, high-order p modes are still able to be observed like being in the main-sequence stars, but they are mixed with g modes at different level that relates to ϵ. On the other hand, at more evolved evolution stage, the star may only have g modes, some of which can be detected in terms of mixed modes that have significant p-mode character. We will follow the classification of mixed modes as in Section 4.1.2 that divide them into two categories, p-m and g-m mixed modes, according to how much they contribute to the kinetic energy. If a mixed mode has a large contribution from the acoustic cavity in mode energy, it behaves more like a p mode having a larger amplitude that enables it to be detected and hence it is called p-m mixed mode.

4.3.1 Phase shift

Following the same denotes of turning points as in Figure 4.5 that the propagation of the oscillation mode is divided into p, g and evanescent region by the turning points 'a', 'b' and 'c'. The coupling strength q is the parameter that measures the level of coupling. As discussed above, the value of q depends on how close the two cavities are. In principle larger-frequency modes have larger q for the evanescent regions get smaller as frequency increasing. But this dose not mean larger-frequency modes have greater mixed character than lower ones. The occurrence of mixed modes is determined by the eigenvalue conditions in equations (4.6) meaning the integrals of K of a given mode in different oscillatory regions should satisfy the conditions. The evanescent region is between b and c, of which the width relates to the strength of coupling between oscillatory waves traveling in g region and p region. It is obvious that width changes with frequency as well as the two characteristic frequencies, N and S_l. However, the changes of q for adjacent modes are not significant, which means they have similar coupling strength but avoided crossing only happens to certain modes. The reason for that is q is not related to the occurrence of avoided crossing, but from equations (4.6) ϵ is the parameter that really matters here. For the case of the sub-giant model $M_{\rm s}$, p modes are still observable. The frequency échelle diagram of acoustic oscillation

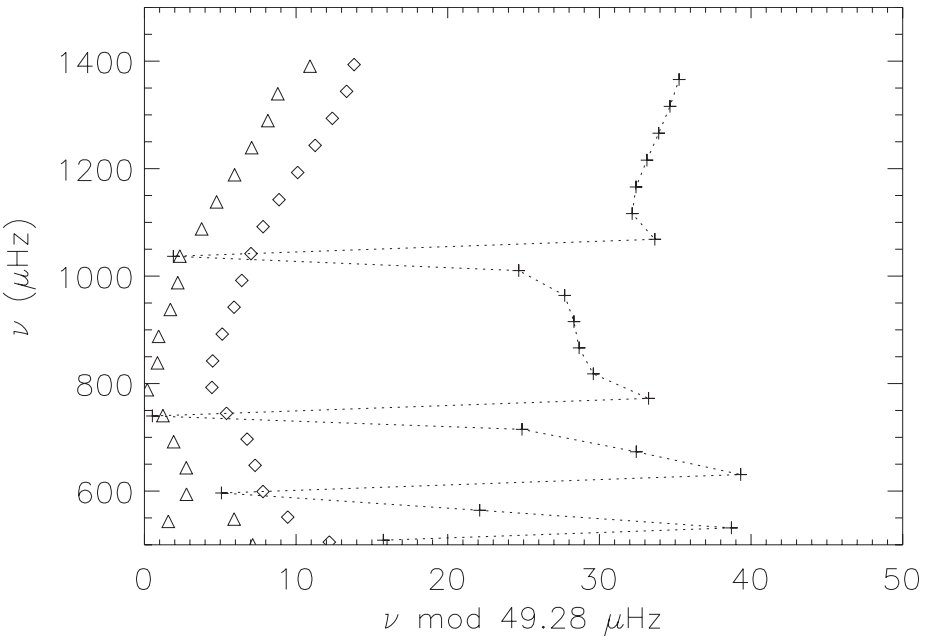

Figure 4.16: Frequency échelle diagram of acoustic oscillation modes ($n > 0$) in $M_{\rm s}$. Modes of different degrees are indicated by diamonds ($l = 0$), pluses ($l = 1$) and triangles ($l = 2$). To guide the eyes the line connected the dipolar mixed modes. G-m mixed modes for $l = 2$ modes are suppressed in the figure.

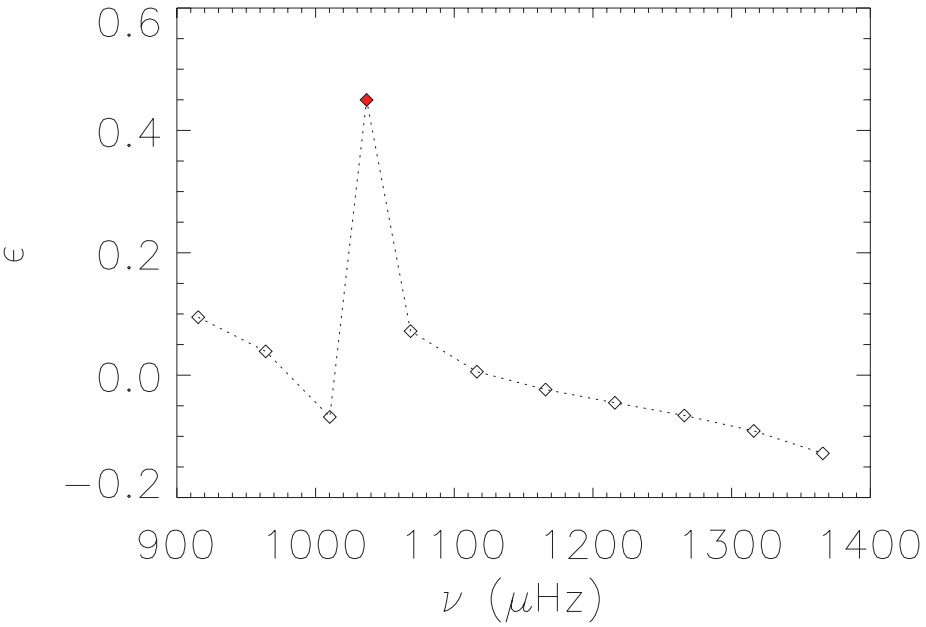

Figure 4.17: Computed ϵ of dipolar modes of Model $M_{\rm s}$ from equation (4.46) as a function of frequency. Each mode is illustrated by diamond. Modes undergoing avoided crossing is in red.

modes of model $M_{\rm s}$ is shown in Fig. 4.16. Though there are slight shifts, the radial modes (diamonds) are stack up vertically, because they are equally spaced by $\Delta\nu$. The reason for the deviations is that $\Delta\nu$ varies with mode orders and the potentially lack of surface correction for high-order modes (Kjeldsen et al., 2008). Mixed modes for $l = 1$ are clearly illustrated in Fig. 4.16 as their frequencies are largely off the vertical pattern. This is due to the reason that when avoided crossing happens the mode frequency bump to a higher value for g-m mixed mode. When the evanescent region is narrow, the coupling is large enough to make significant variations to the modes. The level of coupling is determined by q, but the extent of avoided crossing is decided by the phase shift ϵ:

$$\epsilon \approx \frac{1}{\pi}\int_{r_{\rm c}}^{R} K{\rm d}r - n_{\rm p}. \tag{4.46}$$

Since K only depends on mode frequency and l for a given mode, ϵ also varies with the frequency if we only consider dipolar modes here. However, in reality, the computation of ϵ needs very accurate K for a mode, which is very difficult because K is approximated based on several assumptions. For instance, in equation (1.32) we neglect the cut-off frequency which is generally small in the stellar interior but can be large near the surface. Besides, the lack of corrections for near-surface layers results in offset between computed and observed frequencies for high-order modes (Kjeldsen et al., 2008). Since we only deal with computed frequencies in this thesis, the surface correction is not relevant. Nevertheless, (4.46) still works excellently for determination of mixed modes, because ϵ shift largely from regular pattern when avoided crossing occurs.

Fig. 4.17 shows the computed ϵ of $l = 1$ modes for Model $M_{\rm s}$. Only modes in high frequency range are plotted in the figure, where the asymptotic relation works fine. The mode that undergoing avoided crossing and having irregular ϵ value from other p modes has frequency around 1030 μHz and its ϵ is very close to 0.5. The ϵ of regular p modes should be very small (around 0), but a clear decreasing trend is shown in the plot. The reason for this is the defective treatment of surface terms in asymptotic analysis. Therefore, the computed frequencies of these higher-order modes shift from their true values. The large jump in ϵ of mixed modes is so obvious in this sub-giant model that the use of ϵ as an indicator of the extent of avoided crossing is valid. In the case of more evolved stars with many g-mode mixed modes that are much denser in frequency, ϵ can be a useful window to understand the mixed modes and stellar interior.

As shown in Fig. 4.18, a period échelle diagram for model $M_{\rm r}$ is produced by plotting the frequencies as a function of the period modulo the period spacing $\Delta\Pi$. The uncoupled g modes should be aligned vertically in this diagram, but they spread sideward due to the effect of coupling, leaving the most p-mode like mixed modes located at the sides of each s-shape pattern (red circles in the figure) and the most g-mode like one lies at the centre (green circle). In Fig. 4.18, all these modes are coupled between different orders of g modes and two p modes, namely $n_{\rm p} = 3$ and 4.

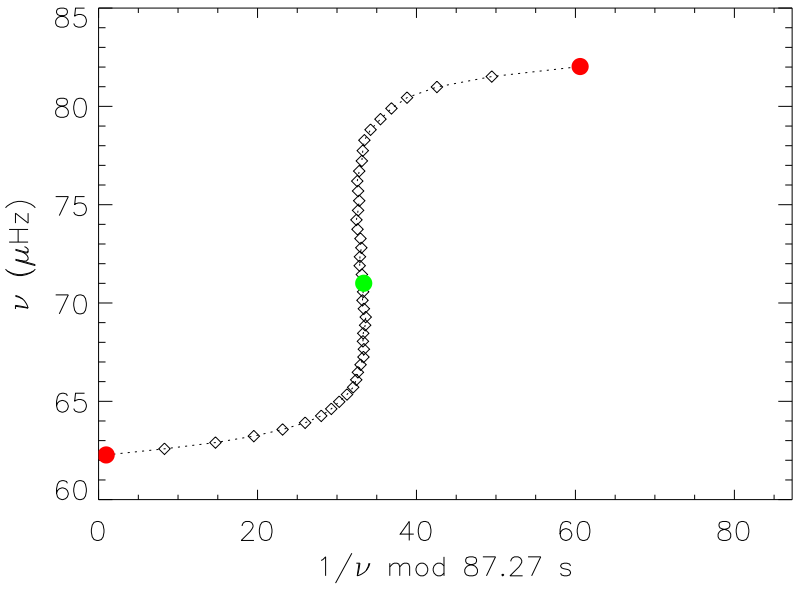

Figure 4.18: Period échelle diagram of a segment of gravity modes in M_r. These g modes are coupled with the same p mode. The modes in red are the most p-mode like mixed modes among the g modes in this plot, while the green circle indicates one that preserve most g-mode character during the coupling.

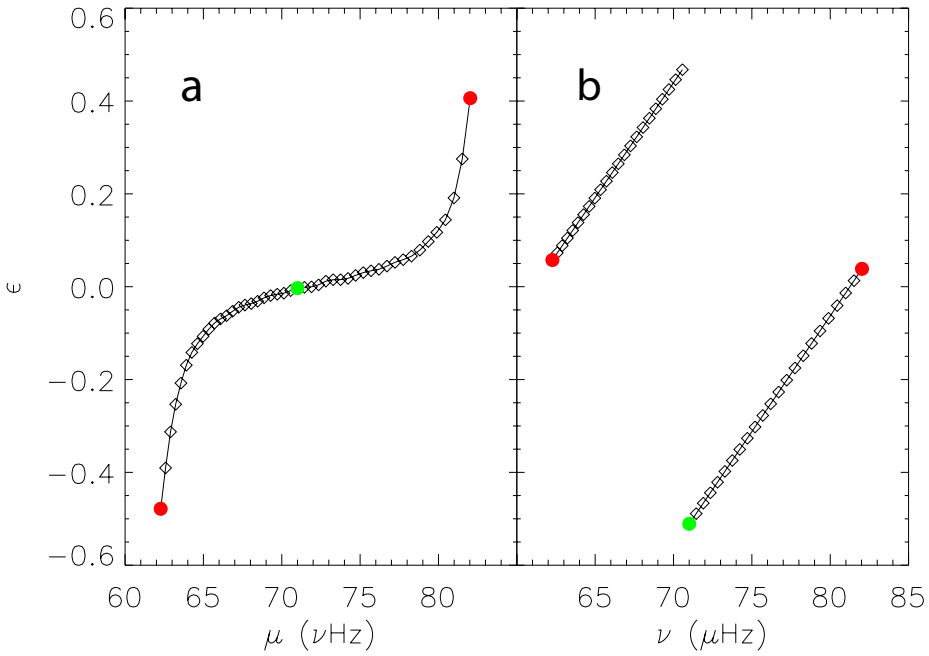

Figure 4.19: (a) Computed ϵ of dipolar modes of Model M_r from equation (4.47) as a function of frequency. (b) ϵ computed from equation (4.46). Green and red circles correspond to the same kinds of mixed modes as in Fig. 4.18. For the two red p-m modes, the first one that is smaller in frequency has a p-mode radial order of 3, while the other one has an order of 4.

The distances of these mixed modes from the centre depend on different ϵ values that reveal the extent of coupling during each avoided crossing. The shift term ϵ is now given by:

$$\epsilon \approx \frac{1}{\pi}\int_{r_\mathrm{a}}^{r_\mathrm{b}} K\mathrm{d}r - \frac{1}{2} - n_\mathrm{g}. \tag{4.47}$$

The resulting value of ϵ of these mixed modes are illustrated in Fig. 4.19(a). Modes in red are the ones having most p-mode like characters and located at the edges of the pattern in Fig. 4.18. Their absolute value of ϵ (near 0.5) is much larger than ones of less perturbed g-mode like modes (the green mode and its vicinities in Fig. 4.18), meaning they are very close to a pure p mode and the green mode is the closest one to a pure g mode. The utility of ϵ as a tool to indicate the extent of avoided crossing is also explained in Fig. 4.19(b), in which the ϵ is computed from equation (4.46). Here the ϵ of red modes are very close to 0 indicating the purity of their p-mode character. Similarly, the green mode, the most g-mode like one, differs more than any other mixed modes in the plot and therefore has an absolute ϵ value close to 0.5. However, the computation of ϵ is very sensitive to the integral of K over different regions, and hence to K itself as well as the locations of the turning points. Due to the use of various approximations in the asymptotic analysis (Jiang & Christensen-Dalsgaard, 2014), K can be not very accurate for many modes, raising the question about the effectiveness of using ϵ. Although ϵ can not be used globally to measure the extent of coupling for this reason, it is still helpful to do so locally as what we do in Fig. 4.18 and 4.19, because we do not need to know the value of ϵ accurately but only to pursue the relative results.

In Section 4.1.2 we introduced that the ratio between the contributions of p and g cavity to the kinetic energy for a certain mode also helps to understand the behaviour of mixed modes. However, the contributions are not able to be obtained from observations directly, making it only stay theoretically. The integrals of wave number K is related to two observable parameters $\Delta\Pi$ and $\Delta\nu$, which makes them more valuable. This will be discussed later.

4.3.2 Mode order of coupled modes

In equations (4.2) and (4.3), n_p and n_g represent the radial order for uncoupled modes. But for coupled modes, their values shift away from pure modes by the number of times they are being coupled, which are the resulting radial orders n given in the model. We first use the model M_s to discuss the shift in radial order caused by coupling. Fig. 4.16 shows p modes ($n > 0$) that experience several times of avoided crossings, though the coupling already happens for low frequency g modes ($n < 0$). The normalized mode inertia E (equation (1.3)) of g modes in Model M_s is plotted in Fig. 4.21. The mode inertia of uncoupled g modes are large because of their large horizontal displacements and great density in the centre. The add of p-mode character increases the displacement vertically but suppresses it horizontally, leading a decrease in inertia. As a result, those mixed modes having locally small inertia, which are the red ones and their vicinities in the plot, are p-m mixed modes and are able to be detected in observations. The detectability of these modes increases with observation time.

The red modes in Fig. 4.21 indicate that there are six times of coupling happening

Table 4.5: Radial orders for Model $M_{\rm s}$ p modes. n is the radial order, while $n_{\rm p}$ and $n_{\rm g}$ are the radial orders of the pure p and g mode that contributes to the corresponding mixed mode, from equation (4.46) and (4.47).

n	$n_{\rm p}$	$n_{\rm g}$
1	7	6
2	7	5
3	8	5
4	8	4
5	9	4
6	9	3
7	10	3
8	11	3
9	12	3
10	12	2
11	13	2
12	14	2
13	14	1
14	15	1
15	16	1
16	17	1
17	18	1
18	19	1
19	19	N
20	20	N
21	21	N
22	22	N
23	23	N
24	24	N
25	25	N
26	26	N

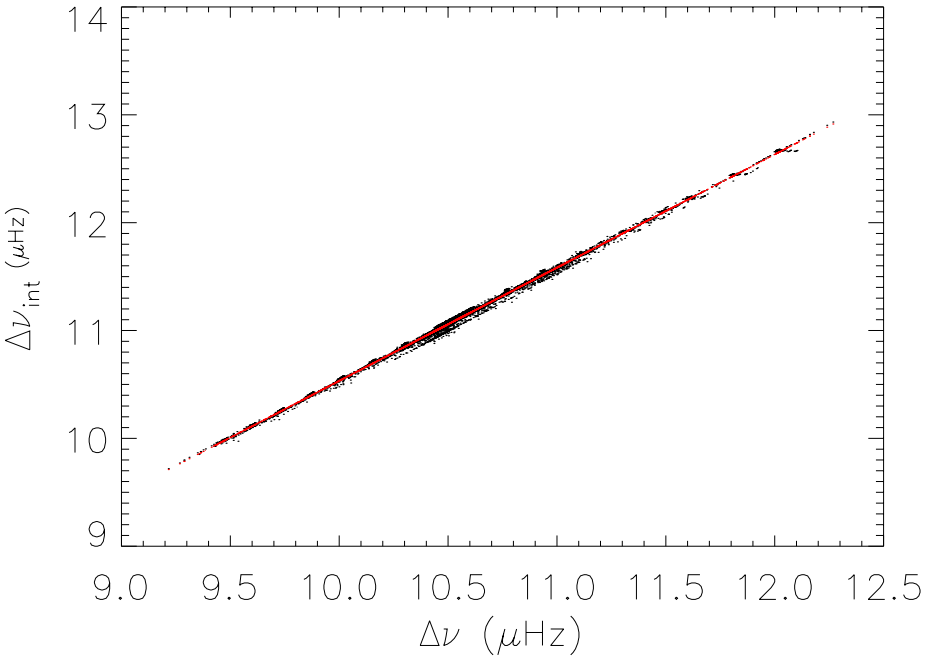

Figure 4.20: The large frequency separations computed theoretically from equation (4.48) as a function of the ones from model frequencies. The black dots are the frequency separations, while the red line is a power law fit.

in the g-mode range, which means the six lowest-order p modes coupling with these g modes and their frequencies are bumped up to higher values as discussed in Section 4.1. As a result, the first six p modes are buried in the g modes. Table 4.5 lists the radial orders n, $n_{\rm p}$ and $n_{\rm g}$ of $M_{\rm s}$ p modes. It is not surprising that the $n_{\rm p}$ value of the first p mode is 7. The first six coupling in the g-mode frequency range means that there are six g modes bumped into p-mode frequency range, due to which it is reasonable to find that there are 6 g modes hidden in the p-mode frequency range.

Similarly, we can also examine the change of radial orders for g modes. In Table 4.6 we list the radial orders for those most p-m mixed modes in g-mode frequency range. Once coupling happens, n is increased by 1 from $n_{\rm g}$(actually it is decreased by 1 if the g-mode radial orders were not defined as negative values). Therefore, the last mixed mode in g-mode frequency range is coupled by the 7th-order g mode and the 6th-order p mode.

In summary, the radial order of a mixed mode is decided by its gravity and pressure radial orders $n_{\rm g}$ and $n_{\rm p}$, being $n = n_{\rm g} + n_{\rm p}$. Given $n_{\rm g}$ is defined as negative value, n is also negative in the g-mode frequency range, but positive in the p-mode range. Similar to ϵ, $n_{\rm g}$ and $n_{\rm p}$ are only related to K, hence to the inner structure of the star and the mode frequency, they are not possible to be obtained directly from observations.

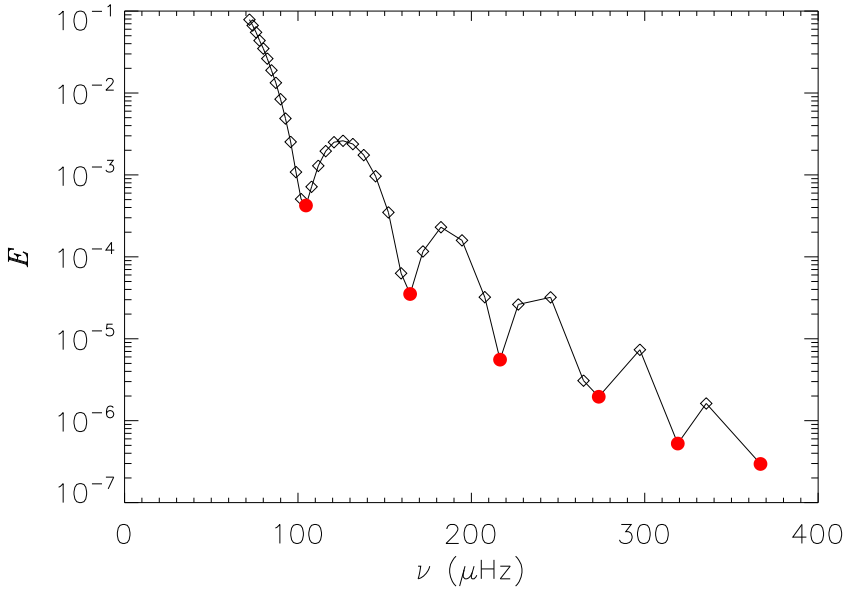

Figure 4.21: Normalized mode inertia (*cf.* equation (1.3)) of $l = 1$ g modes for the model $M_{\rm s}$. The y-axis is in logarithm. Those p-m modes are plotted in red, indicating several times of coupling happen in the g-mode cavity.

4.3.3 Application to observed frequencies

The wave number K provides us a useful tool to explore the interior structure of the star. Although it can only be gained from models, by employing some approximations, it is also related to some observable parameters. Christensen-Dalsgaard (2012) discussed the approximated versions of K in p, g cavity and in the evanescent region through a simple asymptotic analysis. After comparing them with the definitions of $\Delta\nu$ and $\Delta\Pi$, we find that

$$\int_{r_{\rm c}}^{R} K {\rm d}r \approx \frac{\pi\nu}{\Delta\nu_{\rm int}} \ , \tag{4.48}$$

and

$$\int_{r_{\rm a}}^{r_{\rm b}} K {\rm d}r \approx \frac{\pi}{\nu\Delta\Pi_{\rm int}} \ , \tag{4.49}$$

where $\Delta\nu_{\rm int}$ and $\Delta\Pi_{\rm int}$ are theoretical spacings. $\Delta\nu$ and $\Delta\Pi$ are achievable parameters from observations (Bedding et al. (2011), Jiang et al. (2011)), therefore they enable us the possibility to calculate the integrals of K in each region for real stars. However, the approximation make quite a difference between the theoretical spacings, $\Delta\nu_{\rm int}$ and $\Delta\Pi_{\rm int}$, and the ones from observations, $\Delta\nu$ and $\Delta\Pi$. In order to understand how much the difference is, we computed a large number of giant models with mass ranging from 1.1 to 1.4 $M_{\odot}$ and different chemical compositions. A small fraction of

Table 4.6: Radial orders for Model $M_{\rm r}$ g modes.

n	$n_{\rm g}$	$n_{\rm p}$
-25	-26	1
-14	-16	2
-9	-12	3
-5	-9	4
-3	-8	5
-1	-7	6

the large frequency separations is plotted in Fig. 4.20. $\Delta\nu_{\rm int}$ is the theoretical value from equation (4.48). $\Delta\nu$ is obtained from the fit of radial-mode frequencies of the models to their radial orders. A power law fit is performed to the separations for all the models and we find the relation between $\Delta\nu$ and $\Delta\nu_{\rm int}$ is $\Delta\nu_{\rm int} = 1.062\Delta\nu^{0.996}$. The exponent is very close to 1, but for sub giant models it is slightly smaller than red giant models. We do not include main-sequence stars in the computation. Similarly, we also use a power law to fit the period spacings $\Delta\Pi$ and its theoretical values $\Delta\Pi_{\rm int}$ from equation (4.49) and plot them in Fig. 4.22. The exponent of the fit is also very close to one and the power law relation is $\Delta\Pi_{\rm int} = 0.991\Delta\Pi^{1.002}$. From Fig. 4.20 and 4.22 we know that the relations between theoretical values and observed ones are very stable and reliable, which provides us the opportunity to advance the analysis to real data.

The ϵ approach has been applied to one red giant star, KIC 3744043, observed by the *Kepler* space mission. This star was analysed by Mosser et al. (2012) for mixed modes study. They found that $\Delta\nu$ and $\Delta\Pi$ of this star is 9.90 μHz and 75.98 s. Using the power law relation between the theoretical spacings and the observed ones, we approximate the $\Delta\nu_{\rm int}$ and $\Delta\Pi_{\rm int}$ to be 10.42 μHz and 75.95 s. A part of the power spectrum of the KIC 3744043 is plotted in the top panel of Fig. 4.23, covering $2\Delta\nu$ wide, with $\nu_{\rm max}$ of 110.9 μHz locates in the centre. Apart from two radial modes and two $l = 2$ p modes, two bunches of $l = 1$ mixed modes are clearly illustrated. This star is still burning hydrogen around the core but is on the ascending red giant branch (Mosser et al., 2012). Therefore, pure dipolar p mode does not exist and all the observed dipolar modes are p-m mixed modes. We calculate the ϵ for these mixed modes using equations (4.47), (4.48) and (4.49) to indicate how large they deviate from pure g modes and plot them in the bottom panel of Fig. 4.23. As discussed above, these p-m mixed modes possess the p-mode character through coupling. The extent of the coupling is reflected by ϵ. In this case, the most p-mode like mixed modes have largest absolute values of ϵ in their local mode clusters and they locate the farthest away from the dashed line indicating the position of 0. Normally the p modes have much larger amplitude than g modes, which makes them much easier to be observed than the later kinds. This is true as shown in the power spectrum of KIC 3744043. In the first dipolar mode cluster, where modes have frequencies around 106 μHz, the third mode has largest ϵ value and therefore it is the most p-mode like mode in this cluster. The amplitude of this mode is much higher than the rest of the modes located beside which all have comparable low amplitude. It is not possible to distinguish their mixed-mode characters from the power spectrum, but it is possible from the ϵ values.

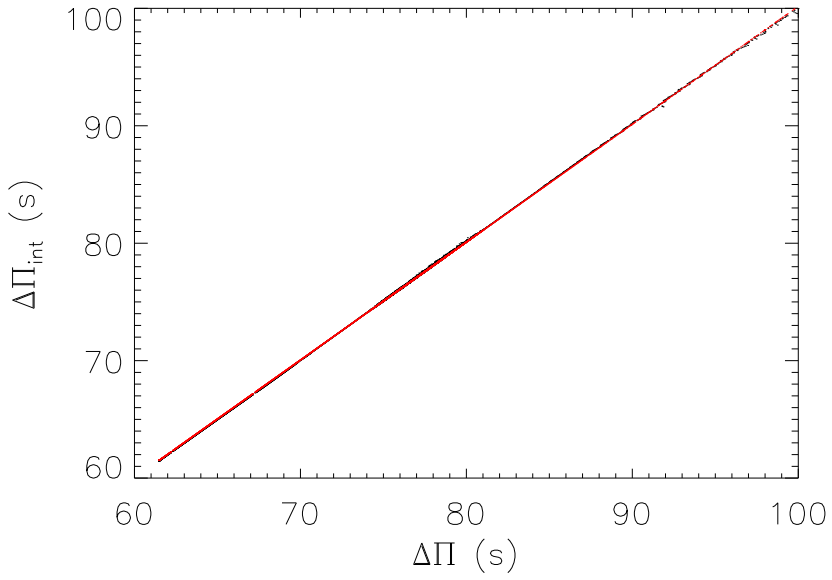

Figure 4.22: The period spacings computed theoretically from equation (4.49) as a function of the ones from model frequencies. The black dots are the period spacings, while the red line is a power law fit.

The second clusters of dipolar modes also prove the validity of using ϵ.

We can also identify the radial order of these dipolar modes directly from equations (4.46) and (4.47). The two most p-mode like mixed modes have pressure radial orders of 10 and 11, respectively, while Mosser et al. (2012) derive them to be 9 and 10 by using the asymptotic relations. The radial orders are from -125 to -110, decreasing by 1 for adjacent mode except for the two most p-mode like mixed modes. Their n stay unchanged as the previous mode.

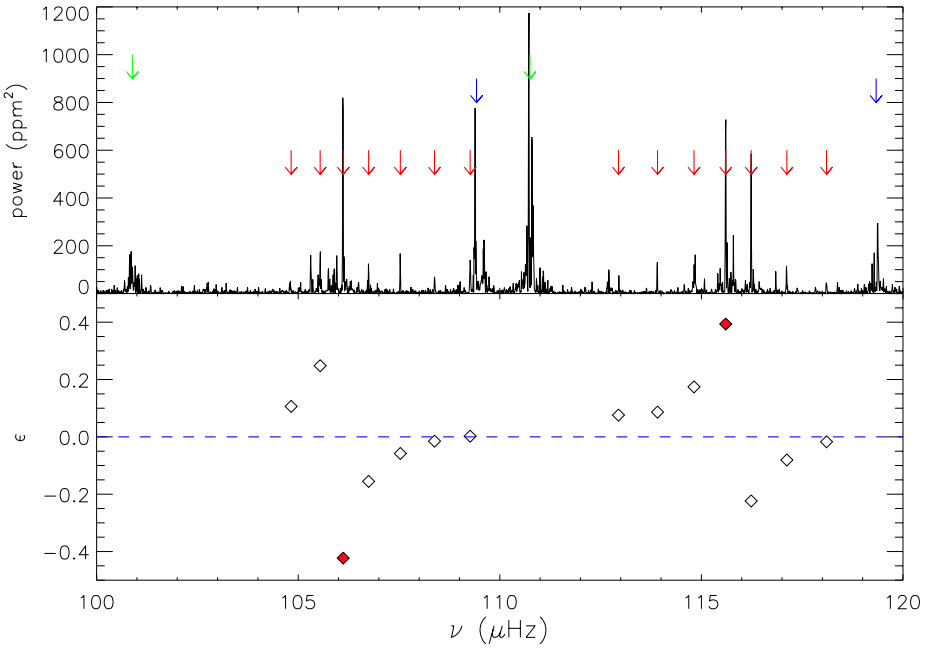

Figure 4.23: *Top*: Power spectrum of the KIC 3744043, with superimposed mode identification provided by Mosser et al. (2012). Red arrows indicate the forests of dipolar mixed modes, while green and blue arrows show the positions of radial tripolar modes, respectively. The power spectrum only covers two $\Delta\nu$ range, with $\nu_{\rm max}$ of 110.9 μHz locates in the middle. *Bottom*: ϵ computed using equation (4.47) for the dipolar mixed modes, as a function of the frequency. Modes with ϵ close to 0 preserve more g-mode character. On the other hand, modes with ϵ away from 0 are more affected by p-mode character. The most p-mode like modes in each cluster are filled with red.

Chapter 5

Conclusions and Future Prospects

In this thesis, we presented several work on aspects of asteroseismology in red giant stars, practically and theoretically. From the observational point of view, we utilized high-precision photometrical data from the *Kepler* space mission launched by NASA and many supplementary data from various high resolution spectrographs, including the promising SONG network led by the Stellar Astrophysics Center (SAC) at Aarhus University. The center is funded by the Danish National Research Foundation. The purpose of the SAC is to study the stars and their planetary systems based on a comprehensive strategy that seeks to produce a complete picture of the structure, atmosphere and magnetic activity of the stars and the planets in their orbit. Theoretical modelling in terms of evolutionary and pulsation calculations were performed with the ASTEC code for stellar evolution and ADIPLS code for oscillation modes.

5.1 Summary and Conclusions

The high-precision and high-quality photometric time series from *Kepler* are able to provide us high resolution frequency dataset of power spectra, with which lots of details of solar-like oscillations in red giant power spectra are revealed for the first time. Despite the inevitably high system noise in low frequency range, normally the power excess range can cover about $6\Delta\nu$ wide in the *Kepler* power spectra with good quality. The peaks of pure p modes are significant enough to be detected. Thanks to the long-term continuous observation of the *Kepler* spacecraft, substantial $l = 1$ mixed modes are also detectable, which gives us a window to study the interior of these stars.

In Chapter 2, we used the *Kepler* red giant star KIC 11618103 as an example to introduce the basic properties of *Kepler* time series and the way to analyze them, including the approaches to remove outliers and systematic trends, and to normal-

ize time series of different quarters. After performing the Fourier transform to the reduced time series, the resulting power spectra are ready for further extractions of seismic parameters, such as $\Delta\nu$ and $\nu_{\rm max}$. However, before this step the background of the power spectrum, which is due to various stellar activities and can contaminate the spectrum with peaks not from oscillations, should be removed first. The background can be modeled by a sum of several Lorentzian-like functions, subtracting which from the spectrum leaves the spectrum with only oscillation peaks significant. During the process of modelling the background, the value of $\nu_{\rm max}$ is acquired from the Gaussian term used to fitting the power excess region. We introduced three different approaches to obtain $\Delta\nu$ from the power spectrum. The first two are the so-called power spectrum of the power spectrum method and auto-correlation method, which are both efficient and stable ways to get $\Delta\nu$ directly from the oscillation peaks. The third method is to perform a linear fit to the frequencies of radial modes, which of course needs to know the individual mode frequencies first. The extraction of mode frequencies is done by using the program of Period04 which can find the oscillation peaks iteratively. However, the program is not suitable for large sample of targets which require more powerful and complicated peakbagging procedures. We extracted 33 frequencies from the power spectrum of KIC 11618103, including two $l = 3$ modes and a bunch of $l = 1$ mixed modes. Using these time series and power spectra analyzing techniques, we demonstrated the result of the red giant stars of the three open clusters in the *Kepler*field, NGC 6791, NGC 6819 and NGC 1811. Stars in a certain cluster are assumed to share the same age, distance and metallicity, which is an excellent advantage that allows for stringent verification of stellar evolution theory. We studied 89 stars belonging to the three clusters, (52 in NGC 6791, 32 in NGC 6819 and 5 in NGC 6811). All of the targets are ascending giant branch stars except for the 5 stars in NGC 6811 which are identified as red clump stars. The $\Delta\nu$ and $\nu_{\rm max}$ for all the targets are obtained from the power spectra, which are utilized in the scaling relations to estimate the stellar masses. Due to the fact that cluster members on similar evolutionary stage have similar masses, the masses that are estimated from the scaling relations should in agreement with other members in the same cluster. For the required term $T_{\rm eff}$ in the scaling relations, they are derived from two different colors $(B - V)$ and $(V - K)$ independently. After the comparison between the resulted temperatures from the colors, we confirmed that $(V - K)$ color index is generally the better temperature proxy for cool red giants. Besides, we listed the global parameters as well as some seismic parameters in the chapter, which are essentially valuable for asteroseismic modelling studies.

As a very important aspect of asteroseismology, asteroseismic modelling interprets stars from the theory point of view. High-quality photometry and spectroscopy provide good measurements of stellar parameters and oscillations. With some appropriate approximations of the complex stellar physics in the numerical calculations, models are proved to be able to reflect real stars very well with global parameters and oscillation frequencies. However, due to near-surface effect, there is a long-last systematic deviation between the computed and observed frequencies, which can be corrected empirically by a power law fitting. In Chapter 3, we presented the surface corrected theoretical frequencies for a model calibrated to the Sun and they match perfectly with observed frequencies in the échelle diagram. Models help interpret real stars, while observations of real stars provide constraints on models. The selection of best-fitting model from tens of thousands of models in the grid should make use of the observation constraints through a calculation of χ^2 minimization. Taking the global parameters,

such as mass, radius, [Fe/H], $T_{\rm eff}$ and so on, and individual frequencies into account in the χ^2 minimizations is a powerful approach to find the best-fitting model that has smallest χ^2 value. We introduced two of our modelling work on real stars. One is a *Kepler* red giant star KOI-1299 which is a host star of a planetary system. And the other one is the first red giant star, 46 LMi, observed by the SONG network. For KOI-1299, time series from the long-term *Kepler* observations give us the opportunity to extract many dipolar mixed modes in addition to expected pure p modes with very good precision. These individual oscillation frequencies used in χ^2 calculations make the selection of best-fitting model more precise and resulted parameters with smaller errors than normal grid-based modelling which do not use frequencies but only global parameters. For the first SONG red giant star 46 LMi, we only have less than two month data with daily gaps, because only one node of the network is observing. We could only identify three modes from the power spectrum, which are not enough for detailed modelling. Therefore we could only model this star with the global parameters, which leads to a less precise determination of masses. As more data coming from observation and more nodes of the network established in the future, detailed modelling which utilize the mode frequencies can be on the table again and can definitely help to improve the modelling results.

Mixed modes result from the coupling between the acoustic and gravity modes in evolved stars when the buoyancy frequency N is high enough that frequencies of g modes are able to approach those of p modes. The amplitudes of pure g modes are usually so small that they are not able to be detected. But in more evolved stars g modes can be observed in terms of mixed mode. The detection of mixed modes in *Kepler* data is a new window on stellar evolution and interior studies. In Chapter 4, we study the properties of mixed modes by using models at different stages along a 1.30 $M_{\odot}$ evolutionary track. When a star evolves past the main sequence, the possible frequency upper limit that a g mode can get to increases dramatically because of the increase of the central density. In the beginning, oscillation modes are dominated by p modes and coupled with several g modes, and high-order pure g modes are only distributed over the low frequency region. Frequencies of p modes are bumped up to a slightly higher value when an avoided crossing happens. As the star ages, frequencies of more g modes grow to be as high as those of p modes. The dense g modes are then coupled with a few acoustic oscillation modes. The frequencies of g modes are diminished a little as a result of coupling in this case. The extent of the coupling can be measured by a coefficient called the coupling strength q that corresponds to how close the g and p cavities are. The closer the two cavities are, the larger is q.

The coupling actually affects every oscillation mode all the time in more evolved stars, at a level which also depends on the mode phases. We followed the work of Mosser et al. (2012) to show an asymptotic relation of mixed modes derived from an implicit relation between the phases of coupled p and g modes. By using this asymptotic relation, we can measure the coupling strength and $\Delta\Pi$ to a very good degree for ascending-branch models by means of grid searching. In other words, the asymptotic relation is very helpful for the identification of mixed modes in observed power spectra. However, our fitting method failed to provide reasonable q for early models where p modes still play the leading role. We managed to classify the mixed modes according to the proportions of the contributions to their mode inertia from the outer region to the central core.

We find that for RG models when a mixed mode has considerable variation in frequency, the proportions of the contributions to its mode inertia from the outer region to the central core change significantly as well. Frequencies of those p-m modes with a large contribution ratio of mode inertia between the two regions ($\zeta \gg 1$) are very close to the pure p modes, which are obvious in the power spectrum. In their vicinities, several mixed modes with relatively smaller ζ ($\zeta \geqslant 1$) can be detected from observation, which have more g-cavity character and hence reveal more information of the central core. Christensen-Dalsgaard (2012) estimated that the chance of finding such mixed modes is related to the width of the maximum reduction in period spacings, which is based on a study of the solutions of an asymptotic dispersion relation. Although we have a slightly different dispersion relation in this thesis, an identical expression for the period spacing is obtained and has been employed to fit theoretical models, which gives excellent results for $\Delta\Pi$ and $\Delta\nu$. We confirm the prediction of Christensen-Dalsgaard (2012) about the chance of finding mixed modes, but we also notice that the width and depth of the dips in period spacing depend on the combination of mode frequency and q. Our fitting to period spacing is able to supply uncertainties and also results in a good outcome of q for more evolved stars, but unreasonably high value of q for high-order g modes. The two fitting approaches can both provide robust outcomes for evolved stars when they are combined. We note that, although our analysis is done for theoretical models, the method is also useful for real observations that provide adequate mixed modes.

The value of q inferred from the analysis of observed frequencies in principle provides diagnostics of the stellar interior, supplementing $\Delta\nu$ and $\Delta\Pi$ which probe, respectively, the envelope and the core of the star. This requires a better understanding of how q is related to the structure of the star in the evanescent region. The theoretical $q_{\rm int}$ from the integral expression of equation (4.5) is obviously inadequate for this purpose, given the problems with the underlying asymptotic equation in the evanescent region. A more careful analysis is required, taking into account the potential singularities. A second limitation in the analysis is the use of the Cowling approximation, neglecting the perturbation to the gravitational potential. We have tested the importance of this by determining the coupling strength computed by fitting frequencies computed in the Cowling approximation, comparing with results based on the full set of equations, and showing a significant reduction in q, by about 0.02. We note that the Cowling approximation could be avoided in the present case of dipolar modes by using the exact second-order equation developed by Takata (2005). This definitely deserves further investigation.

Furthermore, although the coupling strength varies with the mode frequencies, the differences between them are normally quite small for a star. However, it is obvious that the extent of coupling for some modes differs a lot from their vicinities, for their frequencies changes largely from the regular p or g mode pattern. These modes theoretically satisfy the eigenfunction conditions of equations (4.2) and (4.3). In this thesis, we discussed the method of utilizing ϵ, from the eigenfunction conditions, as a tool to distinguish the extent of coupling for adjacent mixed modes. We computed ϵ values for the mixed modes in a sub-giant as well as a red-giant model. For both cases, ϵ is around 0 when the mode suitably satisfies the eigenfunction conditions for pure p and g modes. When the mode meets the condition for mixed modes, the absolute value of ϵ shifts away from zero, meaning the mode gains p-mode character if it was a g mode before or vice versa. Therefore, the absolute value can be used

to determine the extent of coupling for adjacent modes. We apply this method to a red giant star observed by *Kepler*. From the power spectrum of this star, it is not possible to directly distinguish the character of dipolar mixed modes in the same frequency cluster. With the help of ϵ, we can accomplish that by measuring how far away their ϵ values are from zero, once we obtained the $\Delta\nu$ and $\Delta\Pi$ from the power spectrum. Given the fact that the calculation of ϵ is very sensitive to K which is obtained through series of approximation, this method is not suitable for low-order modes where the approximations of K is not valid. However, it works well for observed frequencies for which only modes around the $\nu_{\rm max}$ can be observed and their radial orders are normally high enough.

Another purpose of computing ϵ is to identify the radial order of pure p and g mode that are mixed into a mixed modes. The mixed-mode radial order which indicates the number of radial nodes in the wave function is defined by $|n_{\rm g}| + n_{\rm p}$, where $n_{\rm g}$ and $n_{\rm p}$ are the pressure and gravity radial orders. In order to have an accurate and continuous numbering of mixed modes, which is given in theoretically computed modes, we use the definition $n = n_{\rm g} + n_{\rm p}$. $n_{\rm g}$ and $n_{\rm p}$ can be easily obtained from equations (4.46) and (4.47), which is an alternative way of obtaining the radial orders other than the asymptotic fitting. Knowing the pressure and gravity radial orders gives us better understanding of the contributions of mixed modes from the p and g mode character.

5.2 Future prospects

In this thesis, we introduced the asteroseismology in red giant stars from both modelling and observation point of view, which are of great importance among all the aspects of asteroseismology. However, our understanding of the evolution and the interior, and the physics within, of red giant stars are still inadequate. With the help of asteroseismology, we can improve our understandings about these red giants for sure. In Chapter 2, we analyzed the time series of the open clusters NGC 6791, NGC 6819 and NGC 6811 and obtained global parameters as well as seismic parameters for all our targets. These parameters are excellent constraints for detailed modelling which can precisely determine the masses, radii, age and other parameters of the cluster members. Since stars in a cluster share the same distance, age and metallicity, these parameters determined from models are also expected to be close to each other, though the determination of cluster age can be model dependent and have high errors. The large samples of cluster members are useful to learn the evolution and interior of red giants. Therefore, the detailed modelling of these open clusters is of great interest.

SONG network is believed a very promising project. With the very high quality SONG spectrograph we can measure the velocity to a precision of 1-2 m/s which corresponds to a shift of 100 atoms in the position of the spectral lines on the digital camera in the spectrograph. The data we presented in Chapter 3 were observed by the first SONG node, the Danish SONG telescope in Tenerife, the Hertzsprung SONG telescope. The second node which is located at the Delingha Observatory in the Qinghai province of China and has an excellent infrastructure. The building, telescope and spectrograph are completed and currently alignment and initial commissioning is ongoing. More nodes in different countries all over the world are going to be built in

the very near future. We can imagine what great data this global observation network can provide for asteroseismology studies.

Mixed modes carry information of the stellar outer part where the p cavity is and, more importantly, also that of the inner part where the g modes travel. They enable us to study the interior from observations. However, our understanding of the coupling strength of mixed modes only stay theoretical. The relation between the strength and stellar parameters, such as mass, metallicity and so on, are unclear. In this thesis, we studied mixed modes and the coupling strength and phases theoretically and asymptotically. The asymptotic analysis utilizes some approximations which may lead to improper treatments in same cases. For example, the Cowling approximation used to get rid of the perturbation of the gravitational potential in the general hydrodynamic equations, simplifying the equations into second-order system. But the Cowling approximations are not valid for low radial order modes which are significant in the power spectra of more evolved stars. Additionally, the asymptotic expressions of Airy functions used in the derivations of eigenfunctions are also problematic. As discussed in Chapter 4, the asymptotic expressions are not valid around and at the turning points, which can result in significant deviations, for example the theoretical $q_{\rm int}$ in our analysis is apparent underestimated because of the deviations of K from the asymptotic analysis. Therefore, a more developed asymptotic analysis is needed with the intention to understand mixed modes better.

Bibliography

Aerts, C., Christensen-Dalsgaard, J., & Kurtz, D. W. 2010, Asteroseismology, Astronomy and Astrophysics Library. ISBN 978-1-4020-5178-4. Springer Science+Business Media B.V., 2010, p.,

Barkhatova, K. A., Zakharova, P. E., & Shashkina, L. P. 1978, Soviet Ast., 22, 31

Basu, S., Chaplin, W. J., & Elsworth, Y. 2010, ApJ, 710, 1596

Basu, S., Grundahl, F., Stello, D., et al. 2011, ApJ, 729, LL10

Batalha, N. M., Rowe, J. F., Bryson, S. T., et al. 2013, ApJS, 204, 24

Batchelor, G. K. 1956, *The Theory of Homogeneous Turbulence*, Cambridge: Cambridge University Press, 1956

Baudin, F., Barban, C., Goupil, M. J., et al. 2012, A&A, 538, A73

Beck, P. G., Bedding, T. R., Mosser, B., et al. 2011, Science, 332, 205

Beck, P. G., Montalban, J., Kallinger, T., et al. 2012, Nature, 481, 55

Bedding, T. R., & Kjeldsen, H. 2003, PASA, 20, 203

Bedding, T. R., Huber, D., Stello, D., et al. 2010, ApJ, 713, L176

Bedding, T. R., Mosser, B., Huber, D., et al. 2011, Nature, 471, 608

Bedding, T. R. 2012, Progress in Solar/Stellar Physics with Helio- and Asteroseismology, 462, 195

Belkacem, K., Goupil, M. J., Dupret, M. A., et al. 2011, A&A, 530, A142

Benomar, O., Bedding, T. R., Stello, D., et al. 2012, ApJ, 745, LL33

Borucki, W., et al. 2008, IAU Symposium, 249, 17

Borucki, W. J., et al. 2010, Science, 327, 977

Bragaglia, A., Carretta, E., Gratton, R. G., et al. 2001, AJ, 121, 327

Brandão, I. M., Doğan, G., Christensen-Dalsgaard, J., et al. 2011, A&A, 527, AA37

Brogaard, K., Bruntt, H., Grundahl, F., et al. 2011, A&A, 525, AA2

Brown, T. M., Gilliland, R. L., Noyes, R. W., & Ramsey, L. W. 1991, ApJ, 368, 599

Casagrande, L., Flynn, C., Portinari, L., Girardi, L., & Jimenez, R. 2007, MNRAS, 382, 1516

Chaplin, W. J., Elsworth, Y., Howe, R., et al. 1996, Sol. Phys., 168, 1

Chaplin, W. J., Houdek, G., Elsworth, Y., et al. 2005, MNRAS, 360, 859

Chaplin, W. J., Basu, S., Huber, D., et al. 2014, ApJS, 210, 1

Christensen-Dalsgaard, J. 1982, Advances in Space Research, 2, 11

Christensen-Dalsgaard, J., & Frandsen, S. 1983, Sol. Phys., 82, 469

Christensen-Dalsgaard J., 1984, Liège International Astrophysical Colloquia, Vol. 25, Theoretical Problems in Stellar Stability and Oscillations. Université de Liège, Belgium, p. 155

Christensen-Dalsgaard, J., Dappen, W., & Lebreton, Y. 1988, Nature, 336, 634

Christensen-Dalsgaard, J., Dappen, W., Ajukov, S. V., et al. 1996, Science, 272, 1286

Christensen-Dalsgaard, J., & Thompson, M. J. 1997, MNRAS, 284, 527

Christensen-Dalsgaard, J., Arentoft, T., Brown, T. M., Gilliland, R. L., Kjeldsen, H., Borucki, W. J., & Koch, D . 2007, Communications in Asteroseismology, 150, 350

Christensen-Dalsgaard, J. 2008, Ap&SS, 316, 13

Christensen-Dalsgaard, J. 2008, Ap&SS, 316, 113

Christensen-Dalsgaard, J. 2012, African Skies, 16, 74

Corsaro, E., Stello, D., Huber, D., et al. 2012, ApJ, 757, 190

Cowling, T. G. 1941, MNRAS, 101, 367

Cox, J. P. 1968, New York: Gordon and Breach, 1968

Cutri, R. M., Skrutskie, M. F., van Dyk, S., et al. 2003, VizieR Online Data Catalog, 2246, 0

Djupvik, A. A., & Andersen, J. 2010, Highlights of Spanish Astrophysics V, 211

Dziembowski, W. A., Paterno, L., & Ventura, R. 1988, A&A, 200, 213

Dziembowski, W. A., Gough, D. O., Houdek, G., & Sienkiewicz, R. 2001, MNRAS, 328, 601

Edmonds, P. D., & Gilliland, R. L. 1996, ApJ, 464, L157

Fletcher, S. T., Chaplin, W. J., Elsworth, Y., Schou, J., & Buzasi, D. 2006, MNRAS, 371, 935

Flower, P. J. 1996, ApJ, 469, 355

Frandsen, S., & Lindberg, B. 1999, Astrophysics with the NOT, 71

Fűrész, G. 2008, Ph.D. thesis, University of Szeged, Hungary

Gai, N., Basu, S., Chaplin, W. J., & Elsworth, Y. 2011, ApJ, 730, 63

Goupil, M. J., Mosser, B., Marques, J. P., et al. 2013, A&A, 549, AA75

Gilliland, R. L., Brown, T. M., Christensen-Dalsgaard, J., et al. 2010, PASP, 122, 131

Goldreich, P., & Keeley, D. A. 1977, ApJ, 212, 243

Gough D. O., 1986, in Osaki Y., ed., Hydrodynamic and Magnetodynamic Problems in the Sun and Stars. Univ. Tokyo Press, Tokyo, p. 117

Gough, D. O. 1993, in Zahn J.-P., Zinn-Justin J., eds, Les Houches Session XLVII, Astrophysical Fluid Dynamics. Elsevier, Amsterdam, p. 399

Gough D. O., 2007, Astron. Nachr., 328, 273

Grec, G., Fossat, E., & Pomerantz, M. A. 1983, Sol. Phys., 82, 55

Grevesse, N., & Noels, A. 1993, Physica Scripta Volume T, 47, 133

Grundahl, F., Christensen-Dalsgaard, J., Pallé, P. L., et al. 2014, IAU Symposium, 301, 69

Handberg, R., & Campante, T. L. 2011, A&A, 527, AA56

Handberg, R., & Lund, M. N. 2014, MNRAS, 445, 2698

Harvey, J. 1985, Future Missions in Solar, Heliospheric & Space Plasma Physics, 235, 199

Hekker, S., Kallinger, T., Baudin, F., et al. 2009, A&A, 506, 465

Hekker, S., Basu, S., Stello, D., et al. 2011, A&A, 530, AA100

Høg, E., Fabricius, C., Makarov, V. V., et al. 2000, A&A, 355, L27

Hole, K. T., Geller, A. M., Mathieu, R. D., et al. 2009, AJ, 138, 159

Houdek, G., Balmforth, N. J., Christensen-Dalsgaard, J., & Gough, D. O. 1999, A&A, 351, 582

Houdek, G. 2010, Ap&SS, 328, 237

Huber, D., Bedding, T. R., Stello, D., et al. 2010, ApJ, 723, 1607

Huber, D., Bedding, T. R., Stello, D., et al. 2011, ApJ, 743, 143

Jenkins, J. M., Caldwell, D. A., Chandrasekaran, H., et al. 2010, ApJ, 713, L87

Jiang, C., Jiang, B. W., Christensen-Dalsgaard, J., et al. 2011, ApJ, 742, 120

Jiang, C., & Christensen-Dalsgaard, J. 2014, MNRAS, 444, 3622

Kallinger, T., Hekker, S., Mosser, B., et al. 2012, A&A, 541, A51

Karoff, C. 2008, PhD thesis, Department of Physics and Astronomy, University of Aarhus

Kjeldsen, H., & Bedding, T. R. 1995, A&A, 293, 87

Kjeldsen, H., Bedding, T. R., & Christensen-Dalsgaard, J. 2008, ApJ, 683, L175

Lazrek, M., Baudin, F., Bertello, L., et al. 1997, Sol. Phys., 175, 227

Ledoux, P. 1951, ApJ, 114, 373

van Leeuwen, F. 2007, A&A, 474, 653

Lenz, P., & Breger, M. 2004, The A-Star Puzzle, 224, 786

Lindoff, U. 1972, A&A, 16, 315

Metcalfe, T. S., Monteiro, M. J. P. F. G., Thompson, M. J., et al. 2010, ApJ, 723, 1583

Miglio, A., Brogaard, K., Stello, D., et al. 2012, MNRAS, 419, 2077

Mathur, S., Handberg, R., Campante, T. L., et al. 2011, ApJ, 733, 95

Mosser, B., Belkacem, K., Goupil, M.-J., et al. 2010, A&A, 517, AA22

Mosser, B., et al. 2011, A&A, 525,L9

Mosser, B., Goupil, M. J., Belkacem, K., et al. 2012, A&A, 540, AA143

Mosser, B., Goupil, M. J., Belkacem, K., et al. 2012, A&A, 548, AA10

Pasetto, S., Chiosi, C., Cropper, M., & Grebel, E. K. 2014, MNRAS, 445, 3592

Piau, L., Kervella, P., Dib, S., & Hauschildt, P. 2011, A&A, 526, AA100

Quinn, S. N., et al. 2014, submitted

Ramírez, I., & Meléndez, J. 2005, ApJ, 626, 465

Scherrer, P. H., Wilcox, J. M., Christensen-Dalsgaard, J., & Gough, D. O. 1983, Sol. Phys., 82, 75

Skrutskie, M. F., Cutri, R. M., Stiening, R., et al. 2006, AJ, 131, 1163

Stein, R. F. 1968, ApJ, 154, 297

Stello, D., Bruntt, H., Kjeldsen, H., et al. 2007, MNRAS, 377, 584

Stello, D., Bruntt, H., Preston, H., & Buzasi, D. 2008, ApJ, 674, L53

Stello, D., & Gilliland, R. L. 2009, ApJ, 700, 949

Stello, D., Chaplin, W. J., Basu, S., Elsworth, Y., & Bedding, T. R. 2009, MNRAS, 400, L80

Stello, D., Chaplin, W. J., Bruntt, H., et al. 2009, ApJ, 700, 1589

Stello, D., Basu, S., Bruntt, H., et al. 2010, ApJ, 713, L182

Stello, D., Meibom, S., Gilliland, R. L., et al. 2011, ApJ, 739, 13

Stetson, P. B., Bruntt, H., & Grundahl, F. 2003, PASP, 115, 413

Takata, M. 2005, PASJ, 57, 375

Tassoul, M., 1980, ApJS, 43, 469

Ulrich, R. K. 1986, ApJ, 306, L37

Unno W., Osaki Y., Ando H., Saio H., Shibahashi H., 1989, Nonradial Oscillations of Stars, 2nd edn. Univ. Tokyo Press, Tokyo

Weiss, A., Hillebrandt, W., Thomas, H.-C., & Ritter, H. 2004, Cox and Giuli's Principles of Stellar Structure, by A. Weiss, W. Hillebrandt, H-C. Thomas, H. Ritter. Cambridge, UK: Princeton Publishing Associates Ltd, 2004.

White, T. R., Bedding, T. R., Stello, D., et al. 2011, ApJ, 743, 161